

ENERGY TRANSFER AT GAS-LIQUID INTERFACE:
TOWARDS ENERGETIC MATERIALS

A Dissertation
Presented to the
Faculty of the Graduate School
University of Missouri-Columbia

in Partial Fulfillment
of the Requirements for the Degree
Doctor of Philosophy

by
TAMAS SZABO
Dr. John E. Adams, Dissertation Supervisor
DECEMBER 2007

The undersigned, appointed by the dean of the Graduate School, have examined the dissertation entitled

ENERGY TRANSFER AT GAS-LIQUID INTERFACE:
TOWARDS ENERGETIC MATERIALS

presented by Tamas Szabo,
a candidate for the degree of Doctor of Philosophy,
and hereby certify that, in their opinion, it is worthy of acceptance.

Professor John E. Adams

Professor Carol A. Deakyne

Professor John J. Tanner

Professor C. Michael Greenlief

Professor Ioan Kosztin

ACKNOWLEDGEMENTS

I wish to express my gratitude to my advisor Dr. John E. Adams for his support, guidance, scientific insight, deep knowledge, and the abundance of patience he showed during my graduate work. I would also like to thank Dr. Carol A. Deakyne for further widening my horizon in the field of theoretical chemistry. I am thankful to Dr. Ali Siavosh-Haghighi for his help in the settling into the research, and also the other current and past members of Dr. Adams' group, Michael D. McNatt, Sanaa K. Deshmukh, Soumya Uppalapati, Rachel Castleberry and Michael Valliere for their excellent cooperation. Finally, I wish to extend my gratitude to Dr. Donald L. Thompson and the members of his research group especially the postdoctoral researchers Drs. Richard M. Dawes, Steven G. Arturo and Pablo Nigra for some of the valuable discussions we had. From the Atwood group I like to thank Drs. Nicholas P. Power and Scott J. Dalgarno for their cooperation in the supermolecular chemistry related studies.

TABLE OF CONTENTS

ACKNOWLEDGEMENTS.....	ii
LIST OF TABLES.....	v
LIST OF FIGURES.....	vi
ABSTRACT.....	x
Chapter 1.....	1
Introduction.....	1
Chapter 2.....	6
Gas-Liquid Interface Energy Transfer in a Lennard-Jones System.....	6
I. Introduction.....	6
II. Simulation.....	9
III. Results and Discussion.....	12
IV. Conclusions.....	38
Chapter 3.....	42
Energy Transfer within the Liquid Nitromethane System.....	42
I. Introduction.....	42
II. Simulations.....	45
III. Results.....	50

IV. Summary.....	70
Chapter 4.....	74
Future possibilities.....	74
Appendix A.....	76
Appendix B.....	81
References Cited:.....	88
Vita.....	97

LIST OF TABLES

Table	Page
2-1. Trapping probabilities (%) of incident atoms for different incident angles, liquid temperatures; numbers in parentheses represent the standard deviation of the mean.....	27
3-1. Lennard-Jones parameters used to describe gas-liquid interaction in the scattering simulations.....	47
3-2. Effect of the gas-liquid attractive interaction strength on the scattering behavior.....	59

LIST OF FIGURES

Figure	Page
2-1. Density profiles for liquid indium at temperatures 436 K, 448 K, 459 K, 511 K and 560 K.....	13
2-2. Final kinetic energy distribution of all argon atoms at different temperatures	15
2-3. Final energy distribution of Ar atoms colliding with a liquid In surface. $T_1 = 436$ K.....	16
2-4. Final energy distribution of Ar atoms colliding with a liquid In surface. $T_1 = 560$ K.....	19
2-5. Final energy distribution for scattered species; differing incident angles.....	21
2-6. Final energy distribution for trapped species; differing incident angles.....	21
2-7. Final scattering angle distributions for three different incident angles. $T_1 = 436$ K.....	22
2-8. Final scattering angle distributions for three different incident angles. $T_1 = 560$ K.....	22
2-9. Graphical representation of the definition of the angular distributions; θ_i is the angle of incidence, θ_f is the scattered or final angle and ϕ is the out of plane angle or azimuth ranging between 0° - 180° (in the +y direction) and 0° - -180° (in the -y direction).....	24
2-10. Final scattering azimuth distributions for three different incident angles. $T_1 = 436$ K.....	25
2-11. Final scattering azimuth distributions for three different incident angles. $T_1 = 560$ K.....	25
2-12. Trapping probabilities of incident atoms at different incident angles.....	26
2-13. The improved Baule-model: dark spheres are atoms of the solid at the surface; the light sphere is the incoming projectile.....	29

2-14. Calculated trapping probability as a function of the gas/liquid particle mass ratio at the highest and lowest temperatures considered in the present work.....	31
2-15. Final energy distributions of scattered particles for different gas-liquid well depths. $T_1 = 436$ K.....	33
2-16. Final energy distributions of trapped particles for different gas-liquid well depths. $T_1 = 436$ K.....	33
2-17. Dependence of the atom trapping probability on the scaled gas-liquid interaction well depth, varying ϵ_{gl}^*	33
2-18. Dependence of the atom trapping probability on the gas-liquid interaction well depth, varying the attractive part of the 12-6 potential.....	37
2-19. Dependence of the atom trapping probability on the gas-liquid interaction well depth, obtained through the two different methods described in the text. The solid lines connect data obtained by changing the ϵ_{gl}^* in the Lennard-Jones potential function, while the dashed lines connect data from the simulations in which the repulsive part was held constant in the 12-6 potential.....	38
3-1 Chemical structure of a) RDX (Cyclonite, Hexogen), b) nitromethane and c) TNT	43
3-2. Density profile of liquid nitromethane after 500000 steps at 360 K.....	50
3-3. Density profiles of C (blue) and N (red) at the $-z$ and $+z$ surfaces.....	49
3-4. Weighted density profiles for H (blue) and O (red) at the $-z$ and $+z$ surfaces.....	49
3-5. Convergence of the final energy distribution of all projectiles with increasing number of trajectories. ($T_1 = 360$ K, $\theta_1 = 55^\circ$, $E_i = 12.5$ kJ/mol).....	54
3-6. Convergence of the final energy distribution of all projectiles with increasing number of trajectories. ($T_1 = 360$ K, $\theta_1 = 55^\circ$, $E_i = 92$ kJ/mol).....	54
3-7. Final energy distributions of all particles collided with the simplified “diatomic” liquid. ($T_1 = 300$ K, $\theta_1 = 0^\circ$).....	56
3-8. Final energy distributions of the scattered particles collided with the simplified “diatomic” liquid. ($T_1 = 300$ K, $\theta_1 = 0^\circ$).....	56
3-9. Energy transfer in the model system at gas-liquid interaction strength limits. ($T_1 = 360$ K, $\theta_1 = 0^\circ$, $E_i = 12.5$ kJ/mol).....	58

3-10. Energy transfer in the model system at gas-liquid interaction strength limits. ($T_1 = 360$ K, $\theta_1 = 0^\circ$, $E_i = 92$ kJ/mol).....	58
3-11. Distribution of final energies of atoms with 12.5 kJ/mol initial kinetic energy. ($T_1 = 360$ K, $\theta_1 = 55^\circ$).....	60
3-12. Distribution of final energies of atoms incident with 92 kJ/mol initial kinetic energy. ($T_1 = 360$ K, $\theta_1 = 55^\circ$).....	61
3-13. Final scattering angle distributions for Ar impinging on nitromethane, (fully flexible potential) $T_1 = 360$ K, $\theta_1 = 55^\circ$	62
3-14. Final azimuthal scattering angle (ϕ) distributions for Ar scattering from nitromethane, (fully flexible potential) $T_1 = 360$ K, $\theta_1 = 55^\circ$	63
3-15. Density profiles of rigid-body and fully flexible liquid nitromethane averaged over 500,000 time steps at 360 K.....	65
3-16. Distribution of final energies for atoms incident, with 12.5 kJ/mol initial kinetic energy, interacting with the rigid-body nitromethane liquid surface. ($T_1 = 360$ K, $\theta_1 = 55^\circ$).....	62
3-17. Final scattering angle distributions for Ar scattered from model nitromethane surfaces. $T_1 = 360$ K, $\theta_1 = 55^\circ$, $E_i = 12.5$ kJ/mol.....	64
3-18. Final scattering azimuthal angle distributions for Ar scattered from model nitromethane surfaces. $T_1 = 360$ K, $\theta_1 = 55^\circ$, $E_i = 12.5$ kJ/mol.....	68
A-1. Excerpt of an example CONFIG file used for scattering simulations.....	78
A-2. Example CONTROL file used for scattering simulations.....	79
A-3. Example CONTROL file used for scattering simulations.....	80
A-4. Chemical structure of pyrogallol[4]arene on the left and the hexameric capsule on the right.....	81
A-5. Chemical structure of a) pyrene, b) benzo[α]pyrene (B[α]P) and c) pentacene	82
A-6. Optimized structures for benzene/pyrogallol complexes at the MP2/cc-pVDZ level of theory.....	84
A-7. Optimized structure of the pyrogallol/benzo[α]pyrene complex.....	84
A-8. Optimized structures for the “wall segment” at the B3LYP/cc-pVDZ level on the left, and at the MP2/cc-pVDZ level on the right.....	85

A-9. Optimized structures of the a) pyrene/wall segment and b) benzo[α]pyrene/wall segment complexes	86
A-10. Optimized structures of the a) pyrene/rigid half nano-capsule and b) benzo[α]pyrene/rigid half nano-capsule complexes.....	87

ENERGY TRANSFER AT GAS-LIQUID INTERFACE: TOWARDS ENERGETIC MATERIALS

Tamas Szabo

Dr. John E. Adams, Dissertation Supervisor

ABSTRACT

Physicochemical surface processes have great importance in the different fields of everyday life and science. Computational characterization of collisional energy transfer at a gas-liquid interface is a helpful tool to interpret recent experimental studies and to yield insight into the energy feedback mechanism of multiphase combustion problems. As a first step, a simple Lennard-Jones system was used to investigate the dependence of the collisional energy transfer and the gas atom trapping probabilities on the temperature of the bulk liquid, on the gas/liquid particle mass ratios, on the incident angle of the impinging projectile, and on the gas-liquid interaction strength. We find in accord with the experimental results that the kinematic effects dominate the energy transfer dynamics, but the importance of the role of surface roughening as the temperature of the liquid increases is also seen.

The second system, nitromethane was chosen to extend the range of simulations. It is a molecular model system, representing nitramine-type energetic materials. Having had a good potential description for the nitromethane molecule including all internal degrees of freedom, we generated simplified molecular systems based on the original nitromethane model to isolate particular features of the dynamics. We have investigated the effect of the initial incident energy, of the inclusion of the internal degrees of freedom, of the initial incident kinetic energy and of the gas-surface interaction strength.

The incorporation of internal degrees of freedom enhanced the collisional energy transfer. These calculations also point to the importance of simple kinematics as it predicts the increase of the ratio of energy transferred with increased initial incident energy of the gas particle.

Chapter 1

Introduction

Physicochemical surface processes surround us; we find them in living (biological) and nonliving (environmental) nature, in breathing (air absorption through the lungs or through the skin and abdomen of insects) and in the gas exchange of the atmosphere with the hydrosphere. Gas-liquid surface interactions also play important roles in industrial processes for food production (fizzy drinks, beer), in the chemical industry (sulfuric acid production, for example) and also in homes as low-noise, electricity-independent gas-absorption refrigerators (although these products are not prevalent in households because of their working gas (NH_3) and unsuccessful marketing, they commonly can be found in hotel rooms due to their low noise and power usage) and in industrial air-conditioning units, especially where the electrical system is unreliable or surplus heat sources (waste heat) are easily accessible.¹⁻³

Our interest in the simulation of the energy transfer at a gas-liquid interface is in connection with a study of the burning (deflagration) processes of energetic materials. In carrying out this study we began with simulations of simple systems which allowed us to develop tools, to evaluate them and to gain insight into the problem. We then moved to a consideration of more complicated molecular liquids to extend the understanding acquired in the initial studies and to assess the value of simplistic collision models.

Energetic materials are compounds that contain chemical energy that can be released in a very short time interval. They are customarily used as explosives or propellants. The general composition of these materials consists of two components: an oxidizer (supplies oxygen or accepts electrons) and a fuel (combines with oxygen or releases electrons, a reducing agent). These two components may reside in the same molecule. An example for the latter is TNT, where the nitrated aromatic ring is the fuel (C, H) and the nitro groups are the oxidizer, while blackpowder is an example where the fuel (carbon powder) and the oxidizer (saltpeter KNO_3) are in separate molecules.^{4,5} Propellants are compounds used to create high gas pressures for extended times (longer burns) for driving projectiles or rockets and for other similar uses (blackpowder, nitrocellulose, or the T-Stoff (concentrated hydrogen peroxide)/C-Stoff (aqueous solutions of hydrazine mixed with methanol) liquid bipropellant used by the Germans in their Me 163B rocket fighter plane during WWII.⁶), while explosives are used to create the disruption of solid or liquid bodies (they have a high burning rate), as in construction, mining and warfare (RDX, ammonium nitrate). The exothermic reaction or burning of these chemicals can either be characterized as detonation or deflagration, where in the former the reaction front propagates at supersonic speeds in the material and in the latter it propagates at subsonic speeds.⁴ Having control over the propagation speed allows use of the same compound as either an explosive or a propellant. Currently, the formulation and shaping of solid energetic materials is based largely on practical experience rather than a detailed understanding of the microscopic behavior.

In a simplified model of the deflagration of an energetic material burning occurs in the gas phase, so in order to burn a compound, it has to be transferred into the gas

phase. In the case of a solid compound, it has to be sublimed or melted and evaporated before the reaction can take place. The energy required to melt the surface and evaporate molecules from it presumably is coming from the exothermic reaction itself. (This simple assumption is surprisingly well applicable at describing real-life properties of fuels and combustion processes, like the flash point, a commonly applied property of the petrol chemical industry and the need of atomization (using carburetors or high pressure jet injectors) in internal combustion engines.) It is also observed for some energetic materials that a thin liquid layer is formed at the surface, which pointed to the development of multiphase models, including evaporation from the liquid and coupling to combustion processes exclusively in the gas phase.⁷⁻⁹ The more recent 1 dimensional continuum models use specific elementary reactions to describe the combustion process. In cases like RDX condensed-phase reactions play an important role in the combustion process. The lack of data on the mechanism of the reactions occurring in the condensed phase and their rate coefficients, results in the gas phase being treated only by elementary reactions and is coupled to a single overall reaction describing the condensed-phase processes⁸. These simple continuum models have shown success in describing the combustion behavior of different sample materials, but ultimately a method, where the whole process (including a detailed description of the condensed-phase reactions) is described with a first principles model is sought to aid the formulation and evaluation of present and prospective energetic materials. A necessary part in these models is the description of the energy feedback process from the combustion zone, driving the gasification at the interface. The energy feedback to the liquid surface can occur by absorption of electromagnetic radiation and through kinetic energy transfer (collisions of

different high energy combustion products with the surface). By understanding the energy transfer processes involving surfaces will contribute to improve the performance and safety of energetic materials used in both civilian and military applications. Previous works suggest that energy transfer at surfaces is controlled partly by the degree of surface roughness and by the pathways the energy is channeled in the system.^{10,11}

Experimental investigations into the effect of surface topology and temperature on the energy exchange have been conducted with the use of X-ray scattering^{10,11} from the surface or with time-of-flight (TOF) mass spectrometry detection of scattered particle beams.¹²⁻¹⁸ The experimental setup used in the latter studies generally is an ultrahigh-vacuum chamber, inside which a nearly monoenergetic beam of gas particles is directed at the liquid surface of a jet stream or at a liquid surface inside a constant temperature reservoir (in the simpler cases this is a crucible,^{19,20} in the more sophisticated studies of reactions at the surface a spinning wheel is partly submersed in the liquid with an attached scraper to create a renewing, clean, thin vertical liquid film^{15-17,21-23}). The exiting molecules are identified by a mass spectrometer set up at desired (usually in-plane) scattered angles. The kinetic energy of the exiting particles is measured by chopping the stream of molecules (atoms) into short bursts and recording their time-of-flight (TOF) between the chopper and the mass spectrometer (detector). These experiments often show good agreement with simple kinematic models.²⁴ Computational techniques were also used to simulate the surface^{19,25-27} and to study the energy exchange. The advantage of the computer simulations is that they record all parameters of each trajectory (we can closely follow the flight path of each projectile) providing more details about the surface scattering. Another factor is that the application of theoretical methods (after a reasonably

precise and reliable model and simulation system is created) to study energetic materials, can lead to improvement in both cost effectiveness and safety, as it decreases the need for direct manipulation of potentially dangerous substances.

The eventual target systems of our investigation are surfaces consisting of relatively complex organic molecules, with different fragments and combustion products being the impinging species. The necessary simulation, therefore, is potentially complex and difficult; in the absence of an available specialized code, we adopted a stepwise approach to the overall problem. In order to adapt a simulation code for our purpose, we started with a simple Lennard-Jones system that had been investigated briefly in a previous study. The Lennard-Jones system was used to investigate in detail the behavior of a simple system, using different liquid temperatures, impact angles, impinging masses and gas-liquid interaction strengths, giving insight into the underlying dynamics of this prototypical system. Then, while still refining the code and adding more features, we started working on the more complex simulations of a practical energetic material, nitromethane. The nitromethane system required an expansion of the simulation method, for it is a more complex system with rotational and vibrational degrees of freedom and thus more internal modes into which the energy of the impinging particles can be imparted. To characterize the energy flow into the internal degrees of freedom of the nitromethane, we performed simulations applying rigid bond constraints to the molecule and compared the efficiency of the energy transfer to that observed from the processes with the fully flexible nitromethane. A simplified version of the molecule was also devised to further the understanding on the behavior of the system.

Chapter 2

Gas-Liquid Interface Energy Transfer in a Lennard-Jones System

I. Introduction

While in the last decades considerable efforts have been spent to understand solid surface structures and reactivity with remarkable results,^{28,29} mostly made possible by advances in ultrahigh vacuum technology and the development of sensitive surface analytical techniques,³⁰ less attention has been paid to liquid surfaces. Studies initially have focused on low melting point metal melts and elastic/inelastic scattering of non-reactive gases³¹, while later they have been extended to molecular liquids (glycerol)³² and also to reactive systems (Cl_2 interacting with liquid In, Pb, Bi and Sn³³⁻³⁶; additionally various gases and U^{37,38}). The recent detailed work of Nathanson and coworkers is important to mention. As noted in the introduction they have been using experimental and theoretical methods to examine the features of the energy transfer at gas-liquid interfaces, as well as adsorption and solution processes.^{10,15,17-26,39-43}

Theoretical methods to study the phenomena are helpful tools to help explain the results of the experiments, with several simulations having been attempted.^{19,23,27,40,44,45} One of the methods (probably the most common) and the one we also chose to use is a molecular dynamics simulation involving hundreds of atoms either in the bottom of a simulation cell, or as it is in our case, (see below) forming a layer in the middle of the “box”. If the layer occupies the middle portion of the simulation cell, two equivalent

surfaces are created, either or both of which can be used as targets. Another approach is the one by Muis and Manson,⁴⁴ who used classical scattering theory to calculate the angular distributions of species rebounding from a liquid metal interface.

We selected a Lennard-Jones atomic system (the particular parameters used refer to liquid In) as the model for the initial part of our study. It was selected since it is a relatively simple system, but it is still expected to incorporate the most important kinematic effects of the gas-liquid collisions, as well as enabling efficient executions of the simulations (an especially important consideration in the initial coding phase of the project). The relatively short time needed to complete the simulations is also an advantage in pursuing our goal to “map out” the behavior of the system. Also, since it is an atomic system we do not run into complications such as the role of internal degrees of freedom in the impact energy accommodation and molecule fragmentation problems appearing at the cell expansion step, resulting from the use of periodic boundary conditions.

We expected that the parameters impinging particle mass, initial incident kinetic energy, angle of incidence of the projectile, and temperature of the surface are variables of significance describing the energy transfer process^{18,41}. The roughness of the surface is expected to have an effect on the elasticity of the scattering. At a smoother surface it was expected that elastic collisions similar to the ones observed in the studies of gas-solid interactions ought to predominate. As the temperature increases, the surface becomes rougher, and this roughness can lead to multiple collisions between the incident particle and the atoms at the surface, giving a higher probability of thermal equilibration with the surface. For a monoenergetic incident particle beam it also would tend to cause the

scattered particles to have an energy distribution in better agreement with a Boltzmann distribution^{17,26}.

The Lennard-Jones liquid indium system's other advantage is its low vapor pressure in the temperature range used in the experimental system, which helps avoid further complications arising from collisions of the incident species with evaporated surface particles. The observations collected during the simulations of the In-Ar system, can be extended to other systems described by a Lennard-Jones potential via corresponding states using reduced units. (For example, reduced temperature: $T^* = kT/\epsilon$, and reduced energy: $E^* = E/\epsilon$) In our simulations we explored a larger temperature region; therefore some of our systems were at higher temperatures and we saw measurable evaporation. The Lennard-Jones potential does not yield the best description of liquid metals (for this reason Chase, Nathanson, Gerber and co-workers conducted studies using more complex embedded atom potentials, which were specifically designed for liquid metals²⁷), but it is simple and models the properties well enough for our purposes. (X-ray and neutron diffraction studies of bulk liquid indium suggest that it behaves like a hard sphere liquid, although in liquids like bismuth and gallium, some associations may occur.²⁰)

In this chapter we first show the method we used in our simulations, using the Lennard-Jones system as an example and standard to explain the adaptations to the simulation code. In the Results section, we discuss our findings, including the effect of the manipulation of the surface temperature, the impact angle, the mass of the incident particle, and the interaction energy between liquid and gas.

II. Simulation

The program DL_POLY_2 version 2.14⁴⁶ was used in our simulations. This program was developed primarily by W. Smith and T. R. Forrester at Daresbury Laboratory in 1993 for the Council for the Central Laboratory of the Research Councils. It was designed to do serial and parallel simulations of large molecules using the Verlet leapfrog integration algorithm.⁴⁷ The code is capable of incorporating all degrees of freedom of a molecule and includes a wide variety of built-in potential types. Another advantage of the code is that it has a modular architecture; that is, it is built as a collection of subroutines. This structure made it ideal for our purposes because adapting the code to handle gas-liquid scattering was mostly done by adding new subroutines, requiring fewer modifications to the original code.

At the beginning, our aim was to use the Lennard-Jones system to validate the coding work done, but it soon grew into gathering insight into the fundamental aspects of the surface energy transfer problem. To check the working of the code we took as our prototypical system one previously studied, both experimentally and theoretically, by G.M. Nathanson, J.L. Skinner and co-workers.^{19,27} The parameters we used for the potential interaction (eq 1) were also based on that group's suggestions. To describe Ar incidence on an In surface:

$$V_{ij} = 4\epsilon_{ij} \left[\left(\frac{\sigma_{ij}}{r_{ij}} \right)^{12} - \left(\frac{\sigma_{ij}}{r_{ij}} \right)^6 \right] \quad (1)$$

for the liquid species (In), $\epsilon_{ii}/k = 606.8$ K and $\sigma_{ii} = 281$ pm; for the incident species (Ar), $\epsilon_{jj}/k = 119.8$ K and $\sigma_{jj} = 341$ pm (k here is the Boltzmann constant). To define the

interaction between the Ar and In atoms we used the conventional Lorentz-Berthelot combining rules, (using the arithmetic mean for the σ_{ij} and geometric mean for ϵ_{ij}) resulting in $\epsilon_{ij}/k = 269.6$ K and $\sigma_{ij} = 311$ pm. Initially an fcc super cell with 864 atoms was set up with cubic periodic boundary conditions and a spherical truncation of the potential the cutoff radius is 7.025 Å. (The edge length of the cell is 28.38 Å.) Following the recommendation from the previous simulations,²⁵ we equilibrated the indium at 507.7 K using a Nosé-Hoover thermostat for 10000 steps (the time step here was chosen to be 6.7 fs), thus creating a model of the bulk liquid. (More details can be found in the thesis work of Ali Shrivastava-Haghighi.⁴⁸) Interfaces were created normal to the z-axis by expanding the simulation box in the z-direction to 80 Å (roughly 3 times the original length). This procedure resulted in the creation of a bulk liquid lamella in the middle of a parallelepiped box, with surfaces both at the “top” and “bottom”. A constant energy simulation (NVE), with periodic boundary conditions applied in all three dimensions, was then carried out to let the newly formed surfaces reach thermal equilibrium. During this process the temperature dropped to 436 K, as a consequence of the creation of the surfaces (introduction of surface tension) and evaporation processes. A constant temperature simulation at the derived surface temperature was then used to equilibrate the system further and to accumulate density profile data for the system along the z-axis. The data collection was run for 250,000 time steps, and the density profile obtained (averaged over this time) was found to be in good agreement with the results reported in the work of Nathanson, Skinner and co-workers.²⁵ Finally, we used one of these simulations to generate 100 surface configurations separated by 1000 time steps from one another, saving the positions and momenta of each to use as starting configurations for the liquid

in the subsequent scattering simulations; thus, we start each scattering trajectory with an equilibrated and continuous surface. The above sequence of steps was repeated in obtaining higher initial surface temperatures.

A starting temperature of 567.4 K (also the starting temperature adopted when previous work²⁵) resulted in a 448 K final temperature, while 610 K gave us a 459 K final temperature. We also generated surface configurations equilibrated at 511 K and 560 K. The 511 K final temperature was achieved by two slightly different means, first by following the above mentioned procedure from a 680 K starting temperature, and second more directly by taking an already expanded box and re-equilibrating it at the target temperature. After inspecting the two resulting structure's properties, it was clear to us that the two methods yield equivalent results, but the latter preparation strategy is quicker and gives better control of final temperature. The structures with the 560 K final temperature were obtained by only the latter method.

We were then ready to carry out the actual scattering simulations and to determine the energy transfer to the liquid surfaces. The initial incident particle kinetic energy was chosen to be 92 kJ/mol (it was selected to allow comparison to a previous study¹⁹ and to provide a large difference between the incident energy and the average thermal energy of the liquid), and the incident angle was taken to be 55°, 30° or 0° with respect to the surface normal. (The simulations were carried out for each incident angle in turn.) Visual inspection and earlier trials indicated that during the expansion and the thermal equilibration of the surfaces, atoms left the liquid phase. The long dimension of the cell was further expanded to 100 Å to avoid problems with evaporated particles (positioning the incident particle close to an atom evaporated from the liquid). The incident argon

atom was inserted such that the z-coordinate of argon was set to 50 Å (i.e. at the top of the box) ensuring it was far enough above the surface that there was no interaction between the atom and the liquid surface. The x and y coordinates of Ar are randomly selected from a uniform distribution on the cross-sectional area of the simulation cell. The Ar atom was then directed toward the surface at +z using the previously defined incident energy and incident angle to determine the initial Ar velocity components in an NVE trajectory (the particle was taken to be incident in the xz-plane). The end of each trajectory is determined either by the return of the argon atom back to its initial distance (or any other selected distance) from the surface, or by reaching an arbitrary time limit, in our case 12000 time steps of 0.0012 ps (a total of 14.40 ps). The time limit changes in correspondence with the incident velocity, maintaining a constant relative time excess, ensuring the comparability of the trapping results.

An atom is considered trapped if it does not reach the predetermined distance (the “detection distance”) at the end of the trajectory within the given maximum time, unless it has a positive momentum in the z-direction at this maximum time (i.e. it is moving away from the surface) and zero forces are acting on it. The final energies, velocities, interaction forces, and coordinates were recorded in a report file for later analysis. In each simulation, a total of 4000 trajectories was calculated.

III. Results and Discussion

The density profile along the z-axis (which is perpendicular to the average plane of the liquid surface) was calculated because it is a good indicator of the width and thus the roughness of the liquid surface. Figure 2-1 shows these density profiles at the

different temperatures we have investigated. It can be seen that the shape of the density profiles changes with the temperature in a nonlinear fashion. That the change in the surface contour is especially marked at the highest temperature is not surprising; surface roughening should increase in parallel with an increase of the vapor pressure of the liquid, which is of course a non-linear function of temperature.

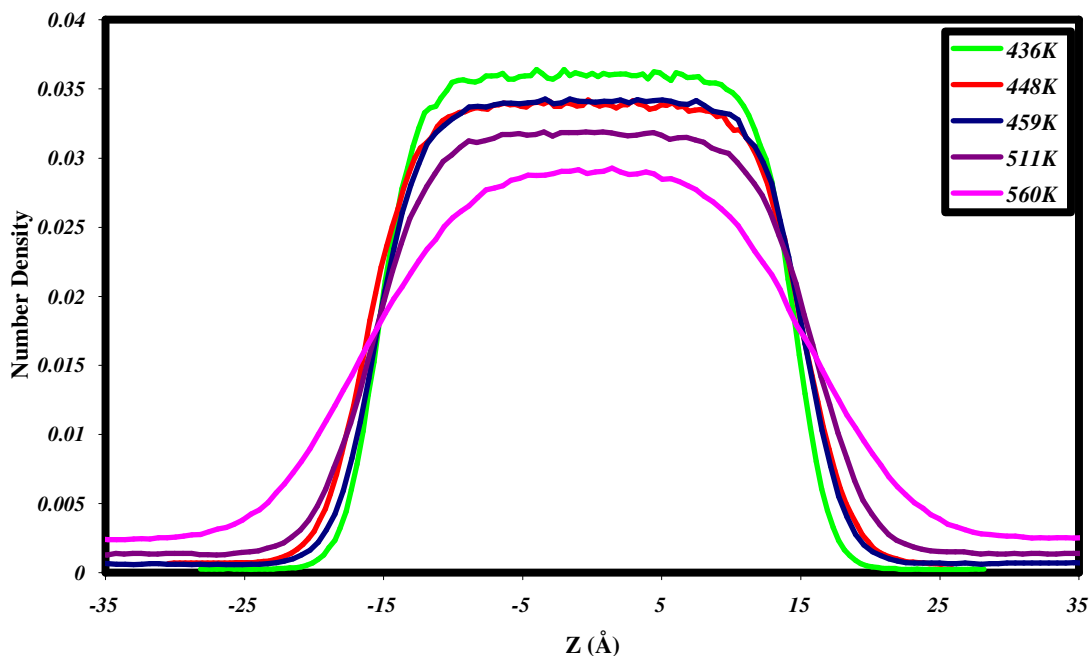


Figure 2-1. Density profiles for liquid indium at temperatures 436 K, 448 K, 459 K, 511 K and 560 K

The lowest chosen simulation temperature (436 K) is not far from the melting point of indium (429.8 K).⁴⁹ It is also visible that the density plot of the bulk has small and random peaks, indicating it is a liquid. The density profile at 436 K is also the narrowest of all. As temperature increases the density profile referring to the bulk liquid gets smoother - as the mobility of the atoms increases, positional averaging becomes more efficient - and the width of the surface increases. The expansion of the indium is

expected, although it is interesting that there is barely a difference between 448 K and 459 K. The wider surface layer implies, of course, a rougher surface. The surface, represented by the slopes, has finite thickness at all temperatures, and that thickness roughly doubles between the lowest and highest temperature structures. Also the density profile in the vapor regime is getting higher and higher in connection with a significant increase in the vapor pressure of indium above the surface.

The graph corresponding to the 436 K result in the figure matches the results of Nathanson and co-workers quite well.²⁵ Both the reduced density $\rho^* = \rho\sigma^3$ (0.83 yielding a number density of 0.037) and the width of the liquid lamella (~ 30 Å) are in good agreement with their values. (More details can be found in the thesis work of Ali Siavosh-Haghighi.⁴⁸)

After the data from the scattering simulations has been collected, we can create energy distribution diagrams corresponding to the final energy of the argon atom after interacting with the liquid surface.

Figure 2-2 is an example showing the final energy distribution of all scattered trajectories. It is easy to see that the population peaks in the low-energy region, and as the temperature of the surface increases, the number of particles having a final energy in the low-energy intervals increases. This result is a clear indicator that the energy transfer efficiency is greater at the higher surface temperatures. From the graph, it is also seen that with increasing temperature, the percentage of low-energy particles increases while the number of particles found in the medium energy range decreases. The average final energies of the scattered atoms at the different temperatures are as follows: at 436 K, 29.4 kJ/mol; at 448 K, 29.6 kJ/mol; at 459 K, 27.9 kJ/mol; at 511 K, 24.4 kJ/mol; and at 560

K, 25.0 kJ/mol. There is no significant difference between the magnitudes of the average final energies.

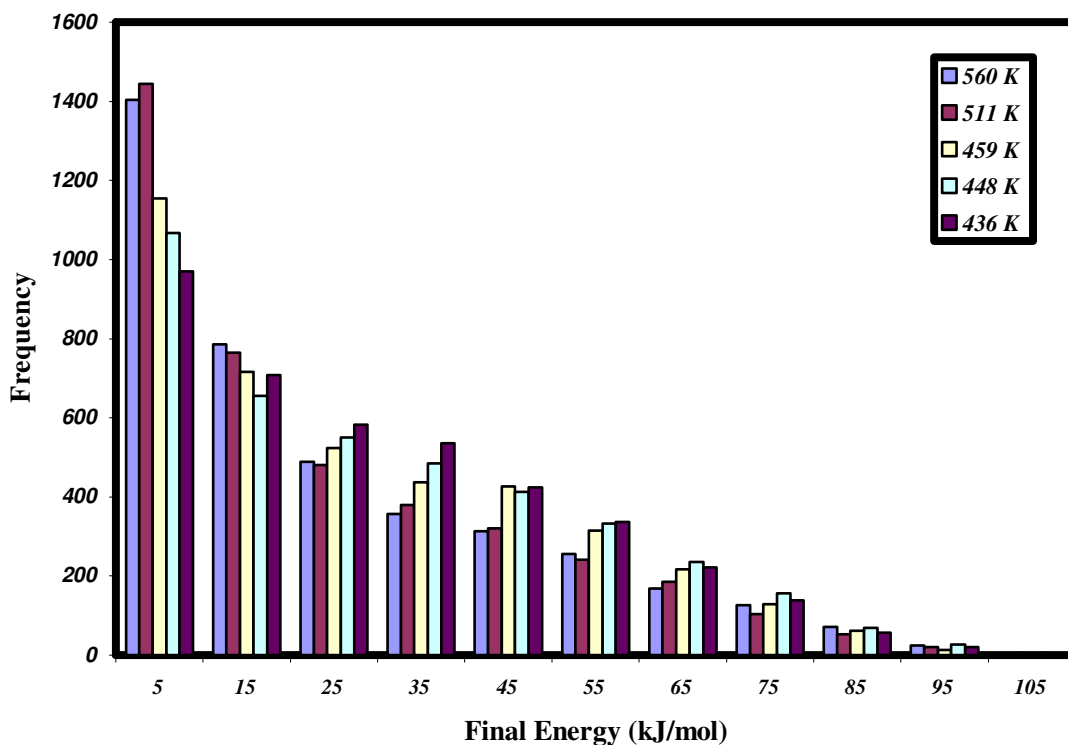


Figure 2-2. Final kinetic energy distribution of all argon atoms at different temperatures

On the following figure (2-3), we show final energies of all the 4000 incident atoms at a temperature of 436 K, but we also display subsets corresponding to trapped and reflected/scattered atoms also. The initial trajectory parameters selected for this calculation were the above-mentioned 92 kJ/mol initial kinetic energy, 55° impact angle, and incident particle mass, which was taken to be that of argon. Thus the mass ratio μ defined by

$$\mu = m_g / m_l \quad (2)$$

where m_g is the mass of the incident gas particle and m_l is the mass of the liquid atoms, had a value of 0.348.

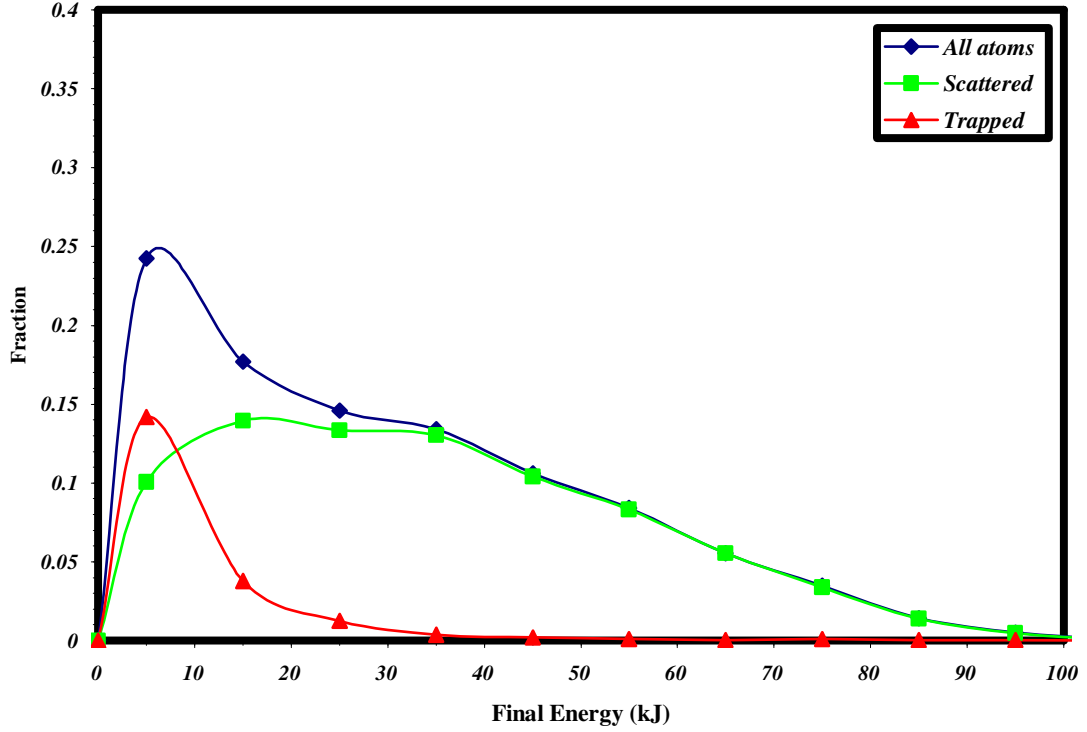


Figure 2-3. Final energy distribution of Ar atoms colliding with a liquid In surface. $T_l = 436$ K

The graph representing the trapped-atom energies rapidly decreases with increasing final energy after peaking at about 5-7 kJ/mol, while the scattered particle energies have a maximum at much higher energies. Essentially, the high-energy part of the latter curve is identical with that of the total curve. In order for the atom to become trapped at the surface, it has to lose sufficient energy to be trapped in the gas-liquid attractive well, or to have a departure trajectory nearly parallel to the surface. Such a trajectory also increases the probability of secondary collisions, further lowering the

energy and eventually possibly thermalizing the atom. Atoms that have sufficient final kinetic energy most likely will escape the surface; thus, they could contribute to either the scattered (making it a large enough distance away from the surface) or the trapped (either too slow to reach a distance of no interaction with the surface or collides with vapor phase atoms) distributions. Also in this figure we can see that there is a small but finite probability that collision with the surface will increase the energy of the scattered particle, resulting in a final energy higher than its initial energy.

All the curves indicate a significant net energy transfer, even if the species is scattered from the surface. To quantify the amount of energy transferred, a Maxwell-Boltzmann distribution was fitted to the final kinetic energy distribution of the scattered species, and the corresponding temperature was determined, using a nonlinear least-squares fit algorithm. For the initial conditions of the simulation represented by figure 2-3, this procedure gives a temperature of about 2400 K that we may compare with the initial energy of 92 kJ/mol, which the equipartition theorem (eq 3) relates to a temperature of approximately 7400 K.

$$E = 3/2 kT \quad (3)$$

This temperature data then can be used to calculate a value for the thermal accommodation coefficient α defined by⁵⁰

$$\alpha = (T_i - T_f) / (T_i - T_l) \quad (4)$$

even though the value is only approximate for the scattered atoms, because the initial energy does not correspond to a thermal distribution characterized by T_i but rather a single value. Nonetheless, the α calculated here is a useful measure of the extent of gas-liquid energy equilibration; $\alpha = 0.72$ in the present case.

It might seem surprising that with such a large value of α , we still get the majority of the atoms scattered from the surface, but the well depth of the two-body gas-liquid potential is only about 2.24 kJ/mol. In order to trap the atom at the surface, the energy transfer has to be even more efficient. Fitting a Maxwell-Boltzmann distribution to the trapped species' energy distribution yields a characteristic temperature of ~509 K, only ~73 K higher than the temperature of the bulk liquid. The difference between the temperatures of the trapped particle and the surface might be even less, because most of the energy of the particle is transferred to the surface thereby leading to local heating.

This efficiency of the energy transfer indicated by our graphs in figure 2-3 could be explained various ways, but since the surface is a liquid, we attribute the efficiency in part to multiple collisions with an uneven, thermally roughened surface.⁵⁰ This explanation suggests that as the roughening increases, the net energy transfer also will increase. Figure 2-4 shows the energy distributions plotted in the same way as in the previous figure, except in this case the bulk liquid temperature is 560 K.

An easy-to-spot difference here is that the fraction of atoms falling into the lowest energy ranges has significantly increased (about 40% for all projectiles, and more for the trapped ones) compared to the results obtained at the lower temperature ($T_1 = 436$ K). Fitting a Maxwell-Boltzmann distribution to these energy distribution results for the trapped and scattered particles, we determined the characteristic temperature to be about 498 K for the trapped particles and approx. 2245 K for the scattered ones. Both of these values are slightly less than those found for the lower liquid temperature case, while calculation of the thermal accommodation coefficient for the scattered atoms gives a similar result $\alpha = 0.75$. The fitted temperature of the trapped species in this case is less

than the temperature of the bulk liquid, but caution is warranted in interpreting this result. The distribution of the trapped particles' kinetic energies is strongly peaked at low energies, and since the applied binning procedure is rather coarse, it can have a significant effect on the fitting accuracy and thus on the calculated final value. On the other hand, this caveat does not change the important observations: the energy transfer efficiency increases with increasing liquid surface temperature and there is an increase in the probability of trapping at the higher temperature surface.

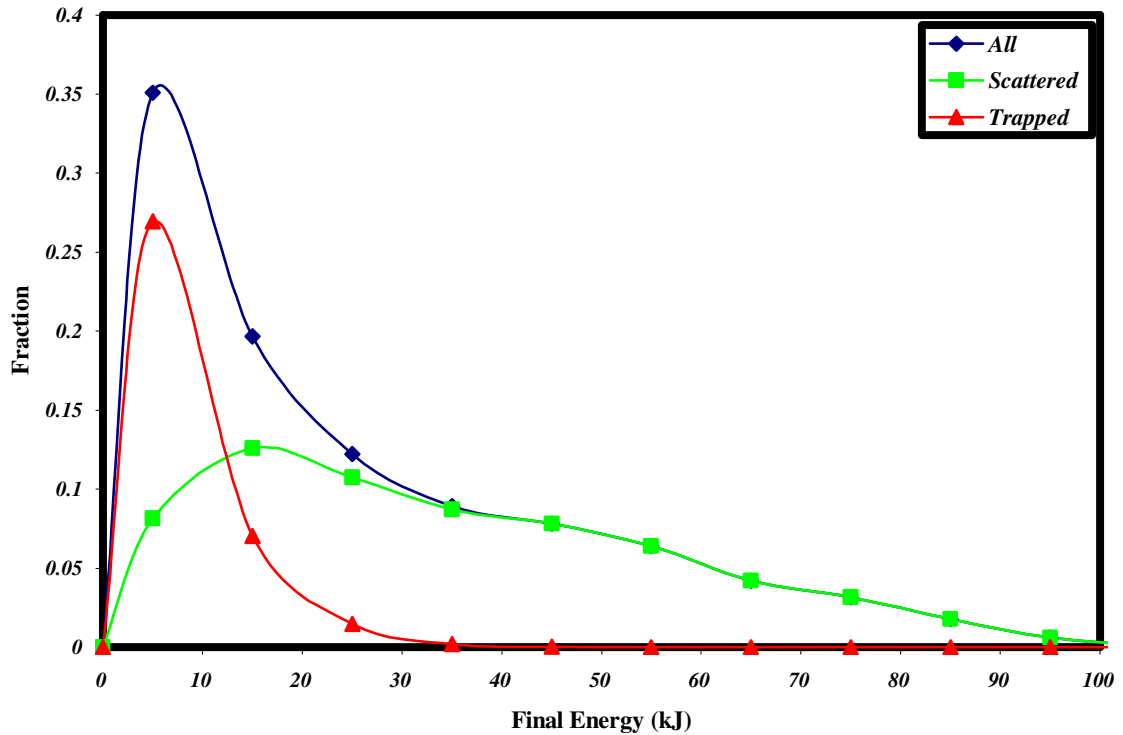


Figure 2-4. Final energy distribution of Ar atoms colliding with a liquid In surface. $T_l = 560$ K

It is important to consider that during actual combustion the incident species will collide with the surface with a multitude of impact angles and that impact angle might have an effect on the fraction of energy transferred. To probe this dependence of the net

energy transfer on the incident angle, three different systems were investigated with angles of incidence of 55° (used in the above mentioned calculations), 30° , and 0° (normal impact). The resulting energy distributions at $T_l = 436$ K for the scattered and trapped species are shown in figures 2-5 and 2-6, respectively.

The general shape of the distributions resulting from trajectories incident with different impact angles does not change significantly with the angle, albeit there is a tendency for a slight increase in the energy transfer as we get closer to a normal angle of incident. This trend might indicate a bias toward the transfer of momentum perpendicular to the liquid surface, but we would not expect the system to be described well by a simple “cube” model,^{51,52} which is based on the conservation of momentum parallel to the surface. (Such models have proved useful in characterizing the gross features of gas-solid energy transfer. The surface of the solid consists of cube shaped atoms, hit by a rigid, elastic sphere of a gas atom.) For the gas-liquid collision process the extended models, like Tully’s “washboard” model⁵³ might be more applicable as they include surface corrugation, although the periodicity of those surface corrugations in the model (in contrast a real liquid is irregular and dynamic) should caution their use.

It should not be too surprising that the energy distribution of the trapped particles does not change appreciably with the change in the incident angle, because in order for the particle to be trapped at the surface most of its energy has to be transferred. The magnitude of the peak of figure 2-6 decreases as the angle of incidence increases, though, confirming the inverse dependence of the energy transfer (and also the trapping probability) on the incident angle. The relatively small differences between the peaks, on the other hand, suggests that trapping is a result of multiple collisions with the surface, as

only the initial two-body collision is expected to retain the signature of the initial angle of approach.

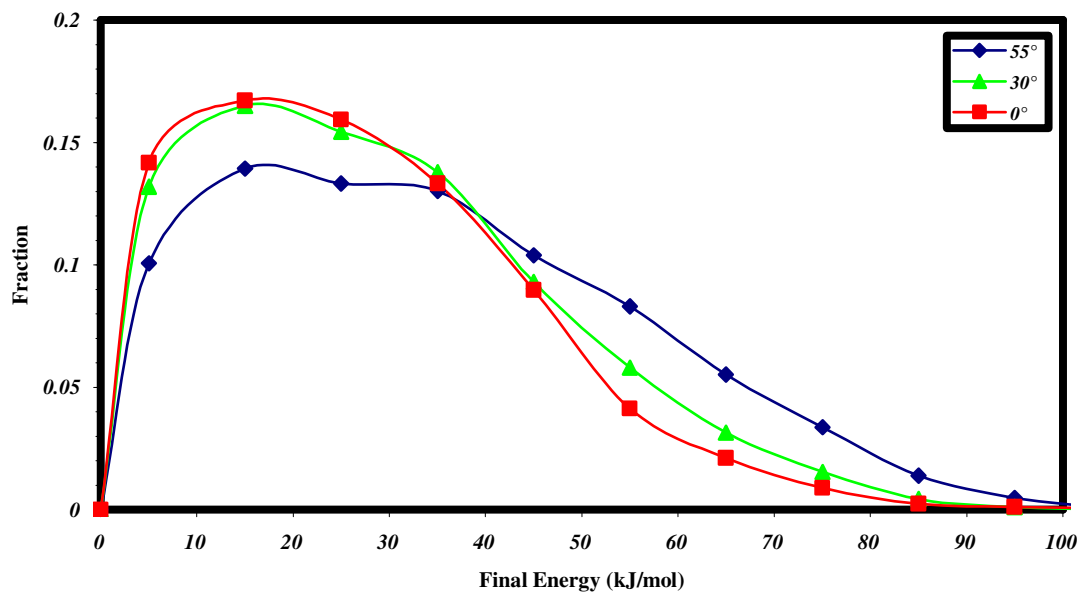


Figure 2-5. Final energy distributions for scattered species; differing incident angles.

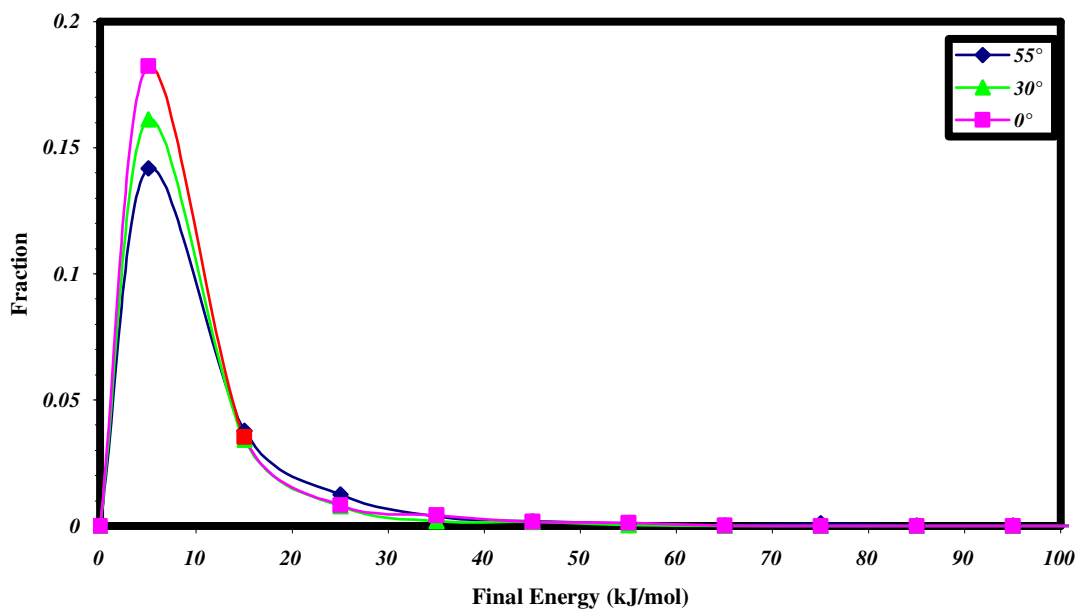


Figure 2-6. Final energy distribution for trapped species; differing incident angles.

Support for the observation that many of the gas-liquid collisions actually involve multiple collisions can be found in the angular distributions of particles scattered from the surface.

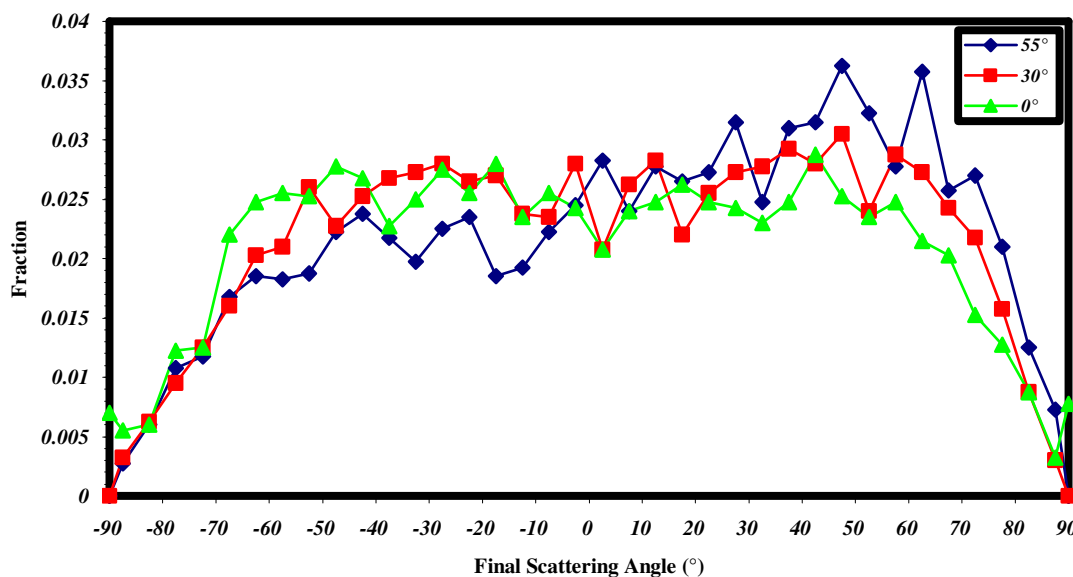


Figure 2-7. Final scattering angle distributions for three different incident angles $T_1 = 436$ K

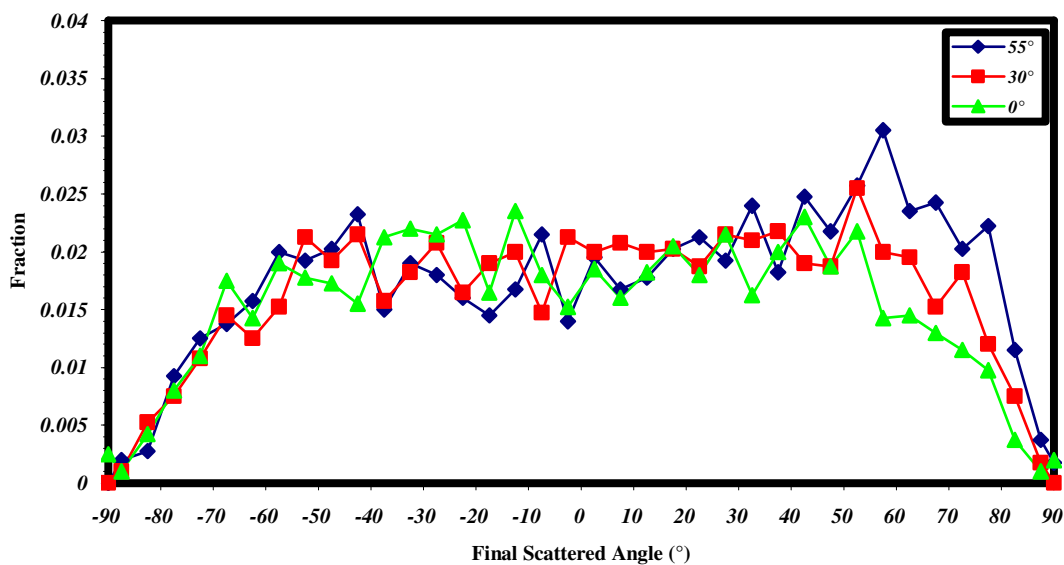


Figure 2-8. Final scattering angle distributions for three different incident angles, $T_1 = 560$ K

Figures 2-7 and 2-8 show these final scattering angles for the simulations at 436 K (figure 2-7) and 560 K (figure 2-8) bulk liquid temperatures. For all the investigated systems, the distribution of the scattering angles is broad, indicating multiple collision events and thus significant energy transfer. The distributions obtained from the 0° angle (normal incidence) trajectories are nearly symmetric; there is approximately the same probability that the particle leaves between $\pm 60^\circ$. The distributions derived from trajectories with the other two initial impact angles show modest preference for scattering in the forward direction. We note that it would be a mistake to try to read too much structure-related information into these distributions since their lack of smoothness reflects real statistical fluctuations of 20-30%. Even so, the general patterns are helpful in explaining the degree of energy transfer. A high efficiency of transfer stems from multiple collisions as well as single inelastic events, which translate into a wide range of scattering angles. Scattering from vapor species (“In” atoms that have left the surface) also widens these distributions. The dependence of the angle distributions on the liquid temperature is not strong, although the peak heights are generally lower at the higher temperature. This difference is explained, as figure 2-5 and 2-6 indicate, by the higher probability of trapping at higher temperatures; thus, there are fewer particles to scatter from the surface. We also note a slightly less preference for forward scattering.

The above described scattered-angle distributions are only a one-dimensional representation of the scattering, as the positive angle values correspond to atoms scattered forward (in the +x) direction and the negative angles refer to atoms scattered backwards (in the -x) direction. To interpret the two-dimensional behavior of the scattered particles,

we need to introduce the distribution of azimuthal angles. The azimuthal angle in our case is the angle between the x-z plane and the y-directional velocity vector of the scattered projectile measured in the plane of the surface, illustrated in figure 2-9.

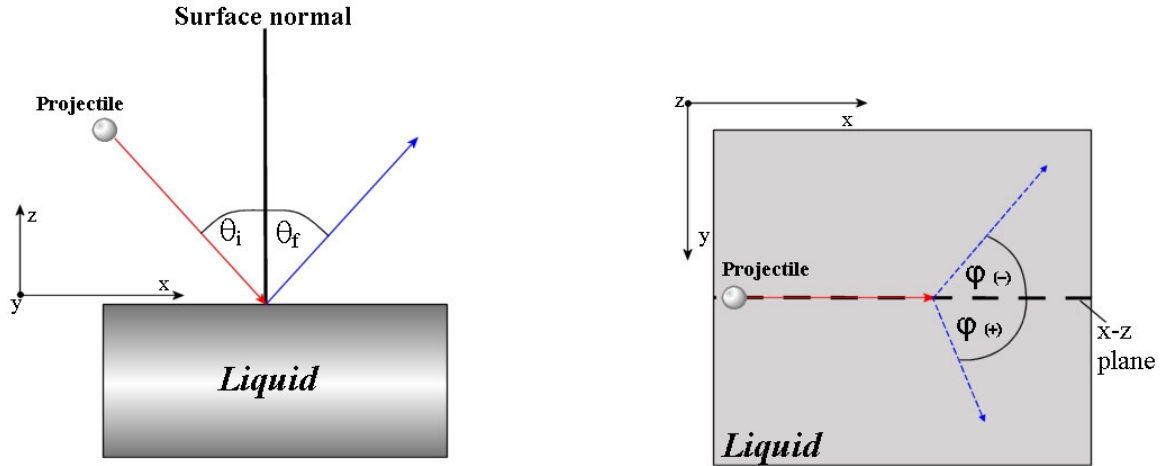


Figure 2-9. Graphical representation of the definition of the angular distributions; θ_i is the angle of incidence, θ_f is the scattered or final angle and ϕ is the out-of-plane angle, or azimuth ranging between 0° - 180° (in the +y direction) and 0° - -180° (in the -y direction)

The following figures (2-10, 2-11) show the distributions of the azimuthal angles of the scattered species. We can clearly see that for a 55° impact angle we have a clear preference for in-plane scattering. This preference disappears, though, as the initial impact angle decreases. (The higher preference for scattering with $|\phi| \leq 90^\circ$ also attests to the preference for forward scattering.) For normal incidences, we have equal probabilities of scattering at all ϕ . As the temperature increases, the azimuthal scattering distribution of the projectiles with the larger incident angle flattens, losing its peaking at 0° under the same conditions that lead to significantly increased trapping. Both results can be explained by the increased surface roughness of the higher-temperature liquid. In general all scattering distribution peaks decrease in magnitude with increased trapping just

because there are fewer and fewer particles contributing to the distributions. The nonzero values associated with the ϕ bins of -170° to -180° and 170° to 180° are consistent with the considerable backscattering noted in the final scattering angle distributions.

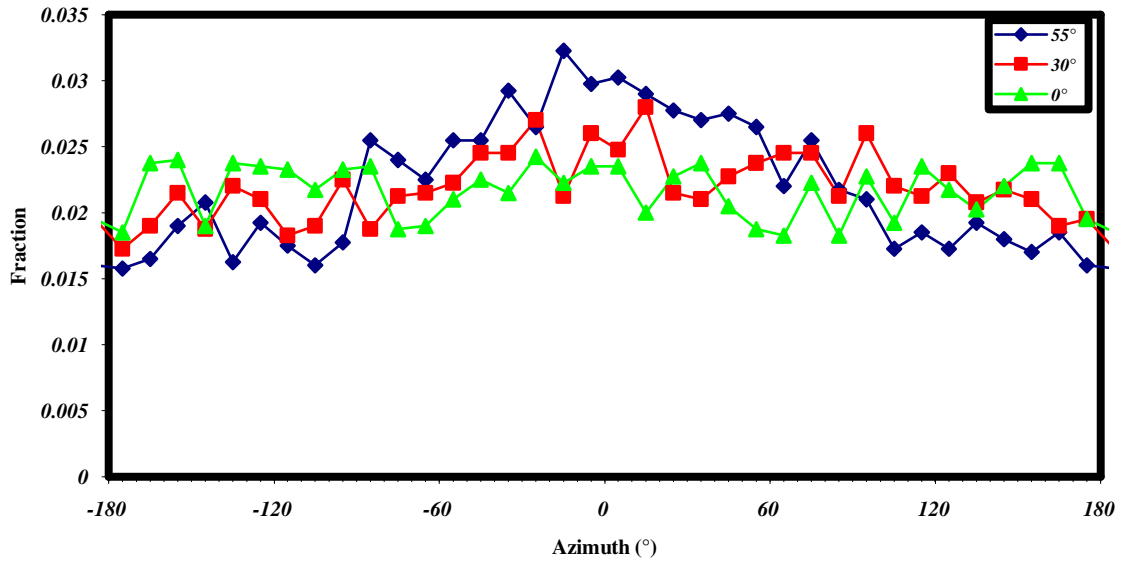


Figure 2-10. Final scattering azimuth distributions for three different incident angles
 $T_1 = 436 \text{ K}$

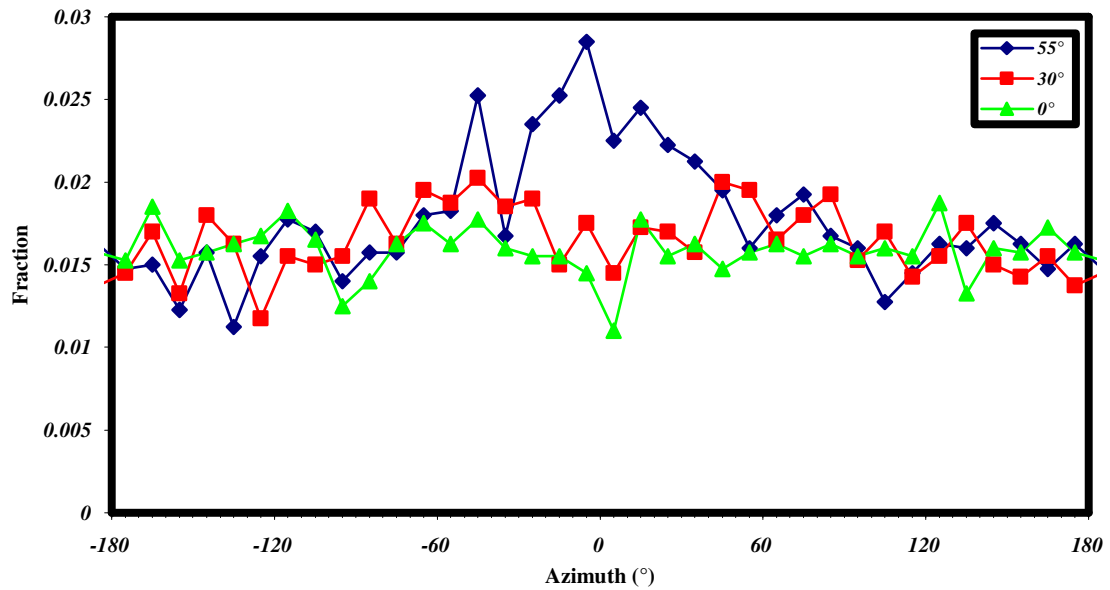


Figure 2-11. Final scattering azimuth distributions for three different incident angles
 $T_1 = 560 \text{ K}$

There is a common feature of the collected results discussed this far, namely that the temperature of the liquid and the angle of incidence affect the probability that the atom gets trapped at the liquid surface, which might lead to its thermal equilibration. It was mentioned in the previous section that the criterion for an atom to be considered “trapped” is that it neither reached the predetermined distance (the “counting surface”) within a given time, nor was it moving away from the surface with no forces originating from interactions with the surface acting on it. Evaluating the trapped particle final energy profiles in figures 2-3, 2-4 and 2-6, we see that the trapped atoms are close to being thermally equilibrated with the liquid surface atoms, thereby validating the applied criteria for trapping. The following figure 2-12 has the trapping probabilities collected for the earlier mentioned systems. Also, we show the numerical values in table 2-1.

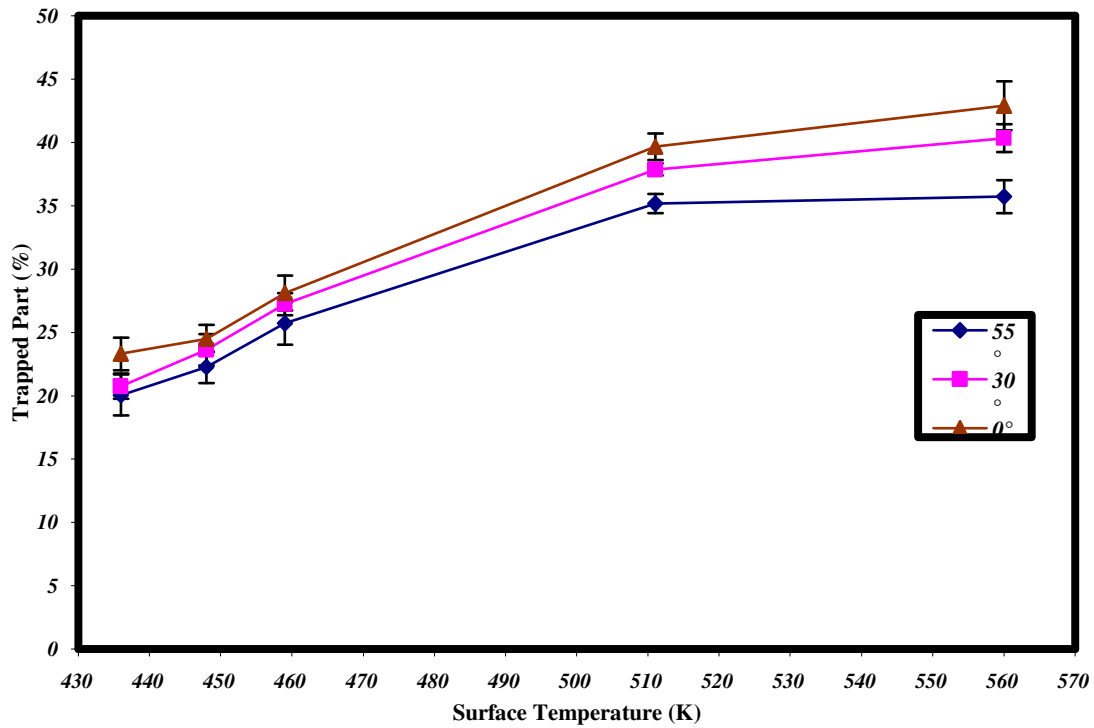


Figure 2-12. Trapping probabilities of incident atoms at different incident angles

Table 2-1. Trapping probabilities (%) for incident atoms at different incident angles; numbers in parentheses represent one standard deviation of the mean.

Temperature (K)	Impact angle		
	0°	30°	55°
436	23.3 (±0.29)	20.8 (±0.23)	20.1 (±0.36)
448	24.5 (±0.24)	23.6 (±0.28)	22.3 (±0.28)
459	28.1 (±0.31)	27.2 (±0.19)	25.7 (±0.38)
511	39.7 (±0.23)	37.9 (±0.11)	35.2 (±0.17)
560	42.9 (±0.43)	40.4 (±0.24)	35.7 (±0.29)

For each of the incident angles studied the trapping probability roughly doubles (1.5-2x) over the temperature interval of 124 K. The results obtained at the two highest liquid temperatures, 511 K and 560 K, show a linear variation with the z-component (normal, see eq 4) of the initial kinetic energy of the particle, where

$$E_z = E_i \cos \theta_i \quad (5)$$

This result may prompt one to draw parallels with the analogous gas-solid interface processes, the analysis of which focuses on that same initial energy component^{51,52}. However, because we have limited data and the scaling does not apply to the whole temperature range, z-component energy scaling is only an interesting observation, one suggesting the need for further investigations focusing on this particular issue.

Up until this point, all simulations used Ar as the projectile, thus resulting in a mass ratio μ of 0.348. Simple kinematic considerations suggest that the efficiency of the energy transfer should depend on the ratio of the masses of the incident and surface particles. One of the equations successful in describing the factors important in gas-solid energy-transfer, the “Baule formula”, which was also used by Nathanson and co-

workers^{17,24} to explain their experimental results, predicts that the average energy transfer ΔE is given by

$$\frac{\Delta E}{E_i} = \frac{4\mu}{(1+\mu)^2} \cdot \frac{1}{2} \left[1 - \cos \chi (1 - \mu^2 \sin^2 \chi)^{1/2} + \mu \sin^2 \chi \right] \cdot \left[1 + \frac{(V - 2RT_l)}{E_i} \right] \quad (6)$$

Here E_i is the initial kinetic energy of the incident species, T_l is the temperature of the surface, μ is the mass ratio, χ is the deflection angle ($180^\circ - \theta_i - \theta_f$), V is the depth of the gas-liquid potential well (modeled as a simple square well), and R is the gas constant. The angle term is used to correct the two-body collision results for a distribution of impact parameters, and the final energy part compensates for the acceleration caused by the attraction between collision partners (the particle at the liquid surface is assumed to vibrate harmonically only, with an energy determined by the surface temperature). This equation is only useful as an approximation, since it is derived for a two-body collision occurs between a gas atom and the last atom of an infinite linear chain. Considering all of these limitations, it nonetheless gives reasonable results when we use it for a system with normal particle incidence, for which the effect of the angle term is minimized ($\langle \chi \rangle \approx 180^\circ$). The calculated average energy transfer for a system like that shown in figures 2-5 and 2-6 is 72%. In contrast our simulations give an average energy transfer of 76% which is reasonably well approximated with the Baule formula.

The model described by Baule was originally devised to describe the temperature-jump phenomenon observed in a system consisting of solid plates at different temperatures, with the space between them filled with thin (low-pressure) gas⁵⁴. At ordinary ambient pressures the temperature gradient in the gas between the plates is linear with distance, but when the pressure is lowered, a temperature jump is measured. This jump increases as the gas pressure decreases. The basis of the model is the

assumption that the solid surface is a vibrating grid with solid atoms at the grid points and the energy transfer during the collision with the gas molecules (spherical, rigid and elastic) being governed by the mass ratio, the initial kinetic energy of the gas particles E_i (in the original case, the average speed, which was related to the temperature) and the surface temperature (T_s). Further improvements of this simple model added the square well potential depth V , to describe the attraction between the gas atom and the surface atoms. Also included was the effect of the impact angle (θ_i), resulting in eq 6.⁵⁵ A graphical representation of the improved model is shown below.

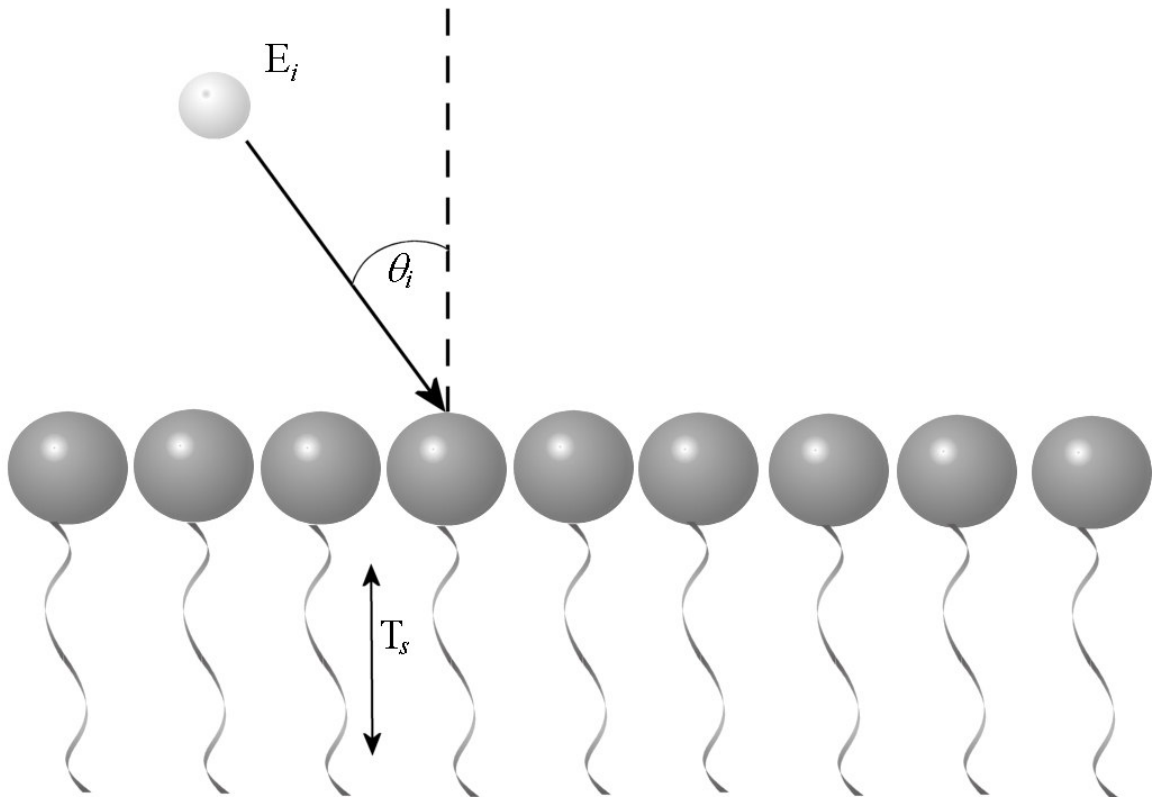


Figure 2-13. The improved Baule-model: dark spheres are atoms of the solid at the surface; the light sphere is the incoming projectile

This part of our research was motivated by the first quotient appearing in eq 6. (The angle factor also involves mass ratios, but it is far too complicated given the wide scattered angle distributions presented above in figures 2-7 and 2-8.) The dependence described by the first factor for very small μ ($\mu \ll 1$) is close to linear dependence of the energy transfer to the mass ratio. At the point where the two masses are the same, unit mass ratio, the quotient is also 1 (its maximum value), leading us to expect a particularly efficient energy transfer in this system. As the ratio further increases ($\mu > 1$), the value of the fraction decreases, suggesting that the energy transfer should decrease also. This analysis presumes that the equation remains valid for $\mu > 1$, but in fact the dynamical assumptions are not strictly valid under those circumstances. (In particular, when the surface atom is less massive than the incident atom, the surface atom is likely to rebound and collide again with the outgoing inelastically scattered atom.)

To test the validity of the kinematic assumptions mentioned above, we ran a series of simulations, where in order to isolate the effect of changing the mass ratio, we used the same potential parameters and only changed the mass of the impinging particle. If the simulated liquid - as it is described in the simulations discussion - was In, the colliding gas species corresponded to Ne, Ar, Kr, In and Pb. To further extend the range of mass ratios tested, we also considered a “light” particle, one having a mass of about half that of Ne (10 g/mol). In these simulations it was crucial to compensate for the effect of masses on the velocity of the projectile at constant initial kinetic energy, necessitating a variation of the time frame used in the determination of trapping probabilities.

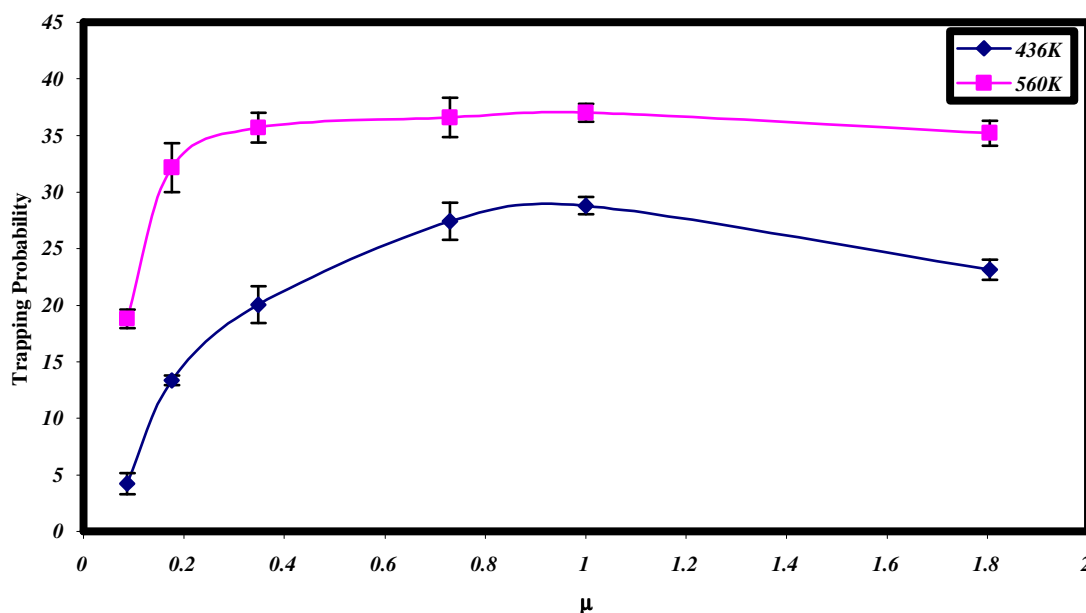


Figure 2-14. Calculated trapping probability as a function of the gas/liquid particle mass ratio at the highest and lowest temperatures considered in the present work.

Figure 2-14 summarizes the results of the aforementioned simulations, focusing on the trapping probabilities as a measure of the energy transfer. The behavior of the Lennard-Jones system clearly indicates a strong influence of simple kinematics on the collision process. At both investigated bulk temperatures, the trapping probability follows the expected trend by rapidly increasing at small values of μ , reaching a maximum when the colliding masses are the same, and slowly declining thereafter as the mass of the projectile is further increased. A significant difference can be seen between the energy-transfer behaviors at the two temperatures, one that cannot be predicted by using the Baule formula. (For the high initial kinetic energies used in this work, the energy factor accounting for nonzero surface temperatures is approximately unity and thus does not explain the difference noted, especially that seen for the small mass ratios.) The kinematic model actually predicts that the efficiency of energy transfer should decrease

with increasing liquid temperatures, because the probability of thermal energy feedback to the impinging particle increases as the temperature of the bulk rises and thus the net energy transfer decreases. The differences found between the predictions of the simple model and our results are mostly due to the variations in surface roughness at the different temperatures having a significant effect on the temperature sensitivity of the scattering dynamics. Another factor which cannot be ignored is the increase in the equilibrium vapor pressure as the liquid's temperature increases, a result shown in figure 2-2. The higher vapor pressure (i.e., a greater number of atoms of the liquid above the surface) increases the probability of collision between the vapor and incident gas particles before and after the incident particle interacts with the liquid surface.

The effect of the gas-liquid interaction potential well depth, the remaining variable governing kinematic energy, was also examined. In these simulations we varied the Lennard-Jones parameter ϵ_{gl} recognizing that ϵ_{gl} is not identical with the well depth parameter V appearing in the Baule formula, the latter describing the well depth of an assumed square-well interaction potential. Given the high initial kinetic energy of the impinging species it was expected that the variation of the well depth, which in our case was changed from (using reduced units $\epsilon_{gl}^* = \epsilon_{gl}/\epsilon_l$) 0.444 (applicable to the Ar-In interaction) to 1.39, will have only a small effect on the average energy transfer. (The change only gives a 5% change in the Baule formula's energy factor.) Figures 2-15 and 2-16 display the results of these calculations.

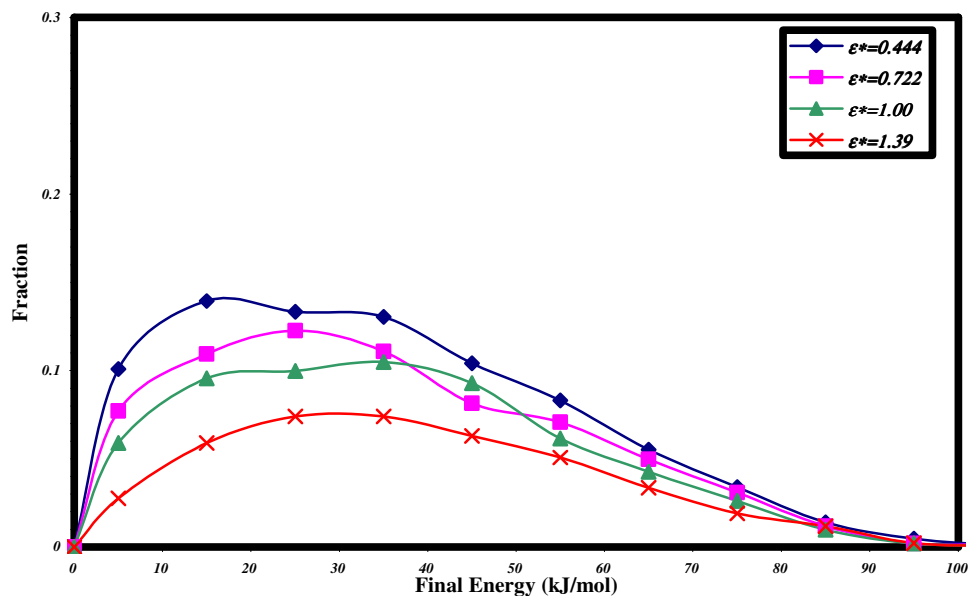


Figure 2-15. Final energy distributions of scattered particles for different gas-liquid well depths. $T_1 = 436$ K

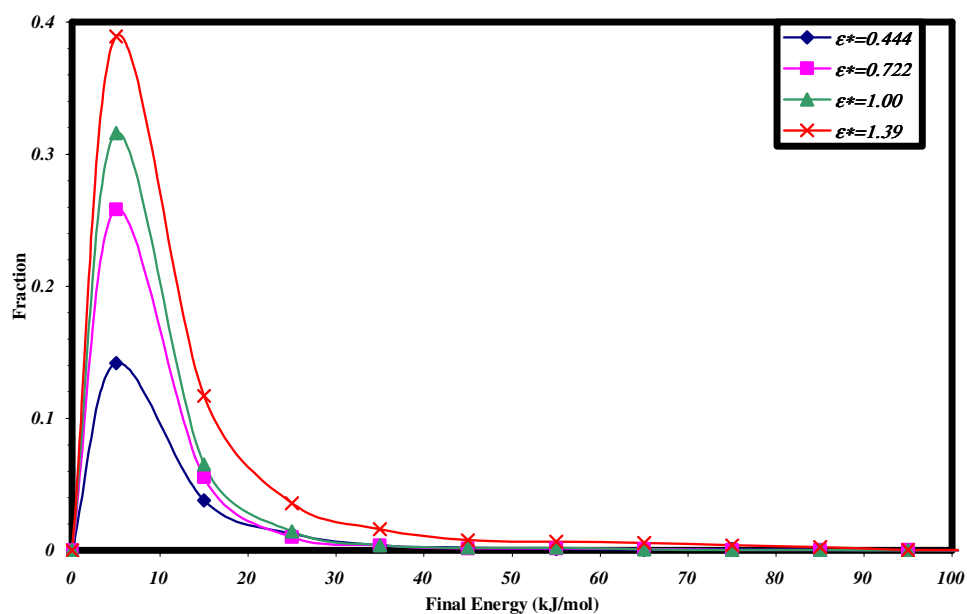


Figure 2-16. Final energy distributions of trapped particles for different gas-liquid well depths. $T_1 = 436$ K

Examining figure 2-15, we see that the general shape of the energy distribution of the scattered species is not affected by the change in the magnitude of the gas-liquid interaction used in those calculations. Only an approximately 11% variation was found in the average final energies of the scattered species over this ϵ_{gl} range. On the other hand the overall effect for all incident atoms was greater, as, with increasing potential energy well depth, the average kinetic energy of all incident species decreased by 31%. (The final kinetic energy distribution for all incident particles is the sum of the final energy distributions of the scattered and the trapped atoms, which implies a larger change in the trapped particle final energy distribution, shown in figure 2-16.) Naturally, all these distributions still peak at the lowest energy bin, but there is a significant change in the bin populations.

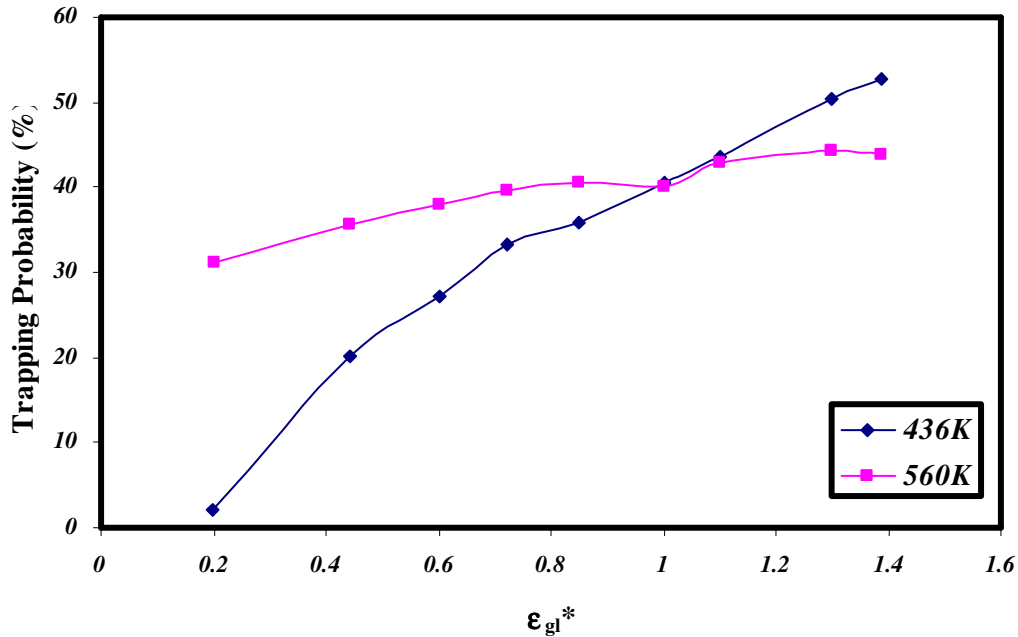


Figure 2-17. Dependence of the atom trapping probability on the scaled gas-liquid interaction well depth, ϵ_{gl}^* .

Figure 2-17, which shows the trapping probabilities at liquid temperatures of 436 K and 560 K, also suggests an increased efficiency of energy transfer with increasing interaction well depth. The graph also seems to show a roughly linear dependency between the interaction energies (even the largest of which is only about 8% of the impinging atom's initial kinetic energy) and the probability that a particle loses sufficient energy to become trapped at the surface. A linear fit to the results at $T_1 = 436$ K for $\epsilon_{gl}^* > 0.4$ gives $p_{\text{trap}} = 0.34\epsilon_{gl}^* + 0.07$ with $R^2 = 0.99$; at $T_1 = 560$ K, we get a slightly worse fit to the data $p_{\text{trap}} = 0.086\epsilon_{gl}^* + 0.33$ with $R^2 = 0.94$ only. These nearly linear dependencies point in the same direction as the predictions from the simple kinematics model; the magnitude of the slope on the other hand is significantly enhanced by the used prototypical system. (The nonlinearity of the trend at low ϵ_{gl}^* values is expected, given the dynamic differences between the behavior of the potentials at the limits $\epsilon_{gl}^* \rightarrow 0$ and $V \rightarrow 0$. The Lennard-Jones repulsive wall gets flatter and disappears as $\epsilon_{gl}^* \rightarrow 0$ while at the same time, the square well potential does not change the “hard wall” repulsive forces as $V \rightarrow 0$.)

The effect of increasing the interaction well depth at the higher temperature is much smaller. An explanation for this phenomenon is found in the energy factor of the Baule formula: the thermal energy is subtracted from the potential well depth, thus if both are increased, the change in the average energy transfer is modest. (The physical explanation is that the accelerating effect of the potential well on the projectile is counteracted by the more energetic thermal motion of the target surface atom.) We also have to consider, though, that an increase in temperature will cause a change in the surface topology (increasing its roughness), resulting in an increased probability of

multiple collisions. With an increased number of multiple collision events, relatively small changes (as a fraction of the incident energy) in the interaction potential well depth do not affect the trapping probabilities significantly.

Changing the value of ϵ_{gl}^* in the Lennard-Jones potential (eq 1) is not only affecting the well depth of the attractive interaction, but just as importantly it is affecting the steepness of the repulsive interaction. In contrast, the kinematic model assumes a single, “hard wall” repulsive interaction, which is independent of the depth of the square well attraction. To simulate systems in which the repulsive interaction is held constant, we used a more general expression for the 12-6 potential (eq. 7). That enables us to tackle the attractive and the repulsive parts of the interaction potential independently. (The standard Lennard-Jones potential is recovered by taking $A = 4\epsilon_{ij}\sigma^{12}$ and $B = 4\epsilon_{ij}\sigma^6$). In these calculations, A is held fixed at the value appropriate to the In-Ar interaction, while B is varied by changing $\epsilon_{ij} = \epsilon_{gl}$.

$$V_{ij} = \frac{A}{r_{ij}^{12}} - \frac{B}{r_{ij}^6} \quad (7)$$

We show the results obtained with the 12-6 potential with A held fixed in figure 2-18, and we also show in figure 2-19 a comparison with the standard Lennard-Jones potential results (the data obtained by holding the repulsive part constant is shown with dashed lines).

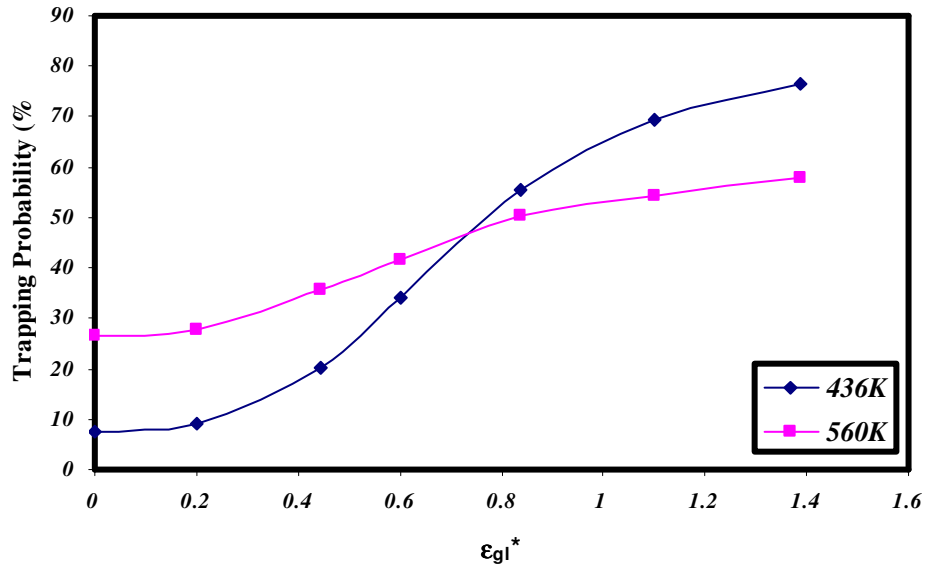


Figure 2-18. Dependence of the atom trapping probability on the gas-liquid interaction well depth, obtained varying only the attractive part of the 12-6 potential.

The curves in figure 2-19 have similar relative positions, though the curves obtained by keeping the repulsive part of the potential function constant have a distinct sigmoidal shape, in contrast to the nearly linear plots obtained from the previous set of simulations. The sigmoidal curves also include a nonzero trapping probability at zero well depth. Manipulating the 12-6 potential by holding A constant still does not replicate the properties of the square well potential used by the Baule formula. Increasing the magnitude of the attractive term B of the 12-6 potential, also changes the shape of the potential energy function, increasing the width of the potential well. (It moves the repulsive wall slightly closer to the center of the atoms.) This makes it possible for the incident atom to interact with multiple surface atoms simultaneously. Another noticeable feature of the independently manipulated attractive potential is that when $\epsilon_{gi}^* > 1$ the resulting trapping probabilities are higher, as the repulsive potential becomes “softer”.

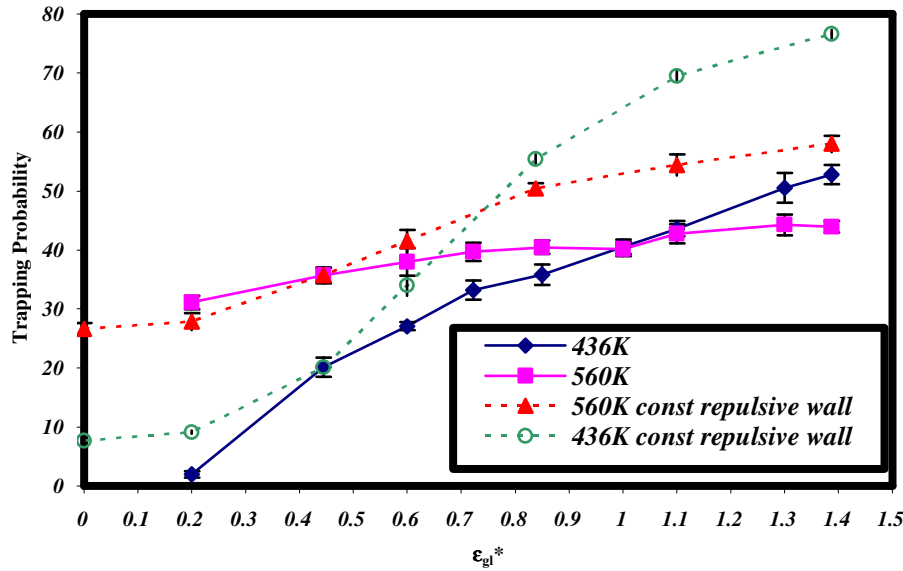


Figure 2-19. Dependence of the atom trapping probability on the gas-liquid interaction well depth, obtained through the two different methods described in the text. The solid lines connect data obtained by changing the ϵ_{gl}^* in the Lennard-Jones potential function, while the dashed lines connect data from the simulations in which the repulsive part was held constant in the 12-6 potential.

IV. Conclusions

The present work began with the modification and testing of the simulation code we intended to use to study the scattering of gas particles from a liquid surface described by a simple Lennard-Jones potential. During the process, though, it became clear that there was a need to investigate a prototypical gas-liquid surface scattering system in detail and to examine the effects of changing the parameters describing the collision process and the participating particles. Though the Lennard-Jones system is an imperfect model of the complex system that is a practical energetic material, it still nonetheless

provides a useful benchmark in analyzing more complex systems. It demonstrated that even in a simple system the energy transfer can be more intriguing than we might expect. The naïve expectation is that the large gap between the average thermal energy of the liquid and the initial kinetic energy of the impinging species leads to nearly elastic scattering dynamics, where the probability of the gas particle thermalizing and becoming trapped is low. We found, though, that the majority of the initial kinetic energy of the incident particles is lost (transferred) during the collision, thus making it possible for a significant fraction of particles to become trapped at the surface, or at least to be delayed sufficiently long to class them as trapped. Such efficient energy transfer was also found by the Nathanson group while investigating HCl scattering from glycerol,²¹ a comparison that validates the use of the Lennard-Jones system in reproducing the fundamental behavior of the energy transfer process at a gas-liquid interface.

Analyses of the angle distributions of the scattering suggest a complex collision process, since most particles scattered away from their specular direction. There is a small preference for forward scattering noted in the cases of the 55° and 30° angles of incidence, and the effect is relatively more pronounced at higher bulk liquid temperatures. The same trends are also observed by examining the azimuthal angle distributions of the scattered species. The strong preference for non-specular scattering suggests that there is a significant probability of multiple collisions, a dynamical picture that also explains the high efficiency of the energy transfer. This analysis is also suggested by the observed roughness of the liquid surface, as revealed by density profiles perpendicular to the surface plane. The change in surface roughness with temperature is also manifested in the azimuthal angle distributions of the 30° incident angle particles; as

the temperature increases, the forward scattering preference diminishes. At higher temperature we see a small fraction of collisions where the surface imparts some of its thermal energy to the incident atom, resulting in a higher final energy than the initial. We can see this behavior in the final energy distributions of the scattered atoms. The probability of this process increases as the temperature of the bulk liquid increases. An explanation for the slight increase in the preference for forward scattering in the case of $\theta_i = 55^\circ$ is that because only the scattered particles contribute to the angular and azimuth distributions, as the roughness increases at higher temperatures, most of the non-trapped particles are deflected in collisions with the outermost surface atoms, thereby decreasing the number of collisions experienced and resulting in a greater propensity for specular scattering.

The observation that our results generally agree well with the predictions of a simple kinematic theory, even though the assumptions of that theory are not strictly applicable, nonetheless suggest that kinematics plays a significant role in many of these processes. These kinematic models were developed to explain the results of energy transfer at gas-solid interfaces, and they do so reasonably well.⁵⁶ Applying the understanding gained by the investigation of gas-solid energy transfer in previous decades to more complex gas-liquid interface processes thus might prove fruitful. Utilizing the previously gained insight to the common features of the gas-liquid and gas-solid systems, allows focusing on the features of the liquid which make up the differences.

A definite difference between liquid and solid surfaces is the temperature dependence of the surface properties, specifically the surface roughness. The simple

models used for gas-solid interface processes cannot account for the magnitude of the effect of the bulk liquid temperature on the energy transfer and on the trapping probability of the incident species at the liquid surface. This dependence requires that the topology of the liquid surface changes with temperature and that the surfaces become rougher and rougher as the thermal energy of the bulk increases. This same property of the liquid was used to explain the increase in energy transfer with temperature by Nathanson and co-workers in the analysis of their experimental work,^{20,25,26} in which they allude to the significance of the kinematic contribution to the collision dynamics. The results shown in this part of our work were published last year in the Journal of Physical Chemistry.⁵⁷

Chapter 3

Energy Transfer in a Liquid Nitromethane System

I. Introduction

For our next step in characterizing the gas-liquid energy transfer, there are two reasonable strategies that retain some control over the number of new variables introduced. The first of these involves changing the liquid from an atomic to a molecular melt while keeping the projectile unchanged. Such a study would allow us to assess the validity and applicability of the analysis of a simple Lennard-Jones system to more complex systems. By changing to a molecular melt, we introduce a multitude of energy disposition channels arising from the molecular rotational and vibrational degrees of freedom that obviously are not present in an atomic liquid. A second strategy would involve retaining the Lennard-Jones liquid but making the impinging particle a molecule. An intermediate case might include a rigid linear projectile, thus minimizing the number of changing variables by reducing the number of internal degrees of freedom. We chose the first strategy in this part of the research.

A suitable system needed to be selected, preferably a relatively small molecular system for which a tested force field is available, but also one that has some connection with the main aim of the overall project, which is the investigation of energetic materials. Nitromethane (CH_3NO_2 or NM) was our molecule of choice, since there is a good force field developed by Sorescu, Agrawal, Rice, and Thompson for it.⁵⁸⁻⁶⁰ This all atom force

field includes all of the molecule's internal degrees of freedom and has been used by Thompson and co-workers to model various properties of nitromethane including its melting characteristics.⁶⁰⁻⁶³ (In developing the force field description, they used a variety of measured properties of the solid CH_3NO_2 , among them the X-ray crystal structure,⁶⁴⁻⁷¹ to validate the potential function. They have found that the potential gives good solid- and melt/liquid-state properties.) Two articles by Thompson and Siavosh-Haghighi^{62,63} are worth mentioning in this regard, as they used a similar method of creating a surface in determining melting temperatures with great success.

Another rationale for choosing nitromethane as the liquid component is that it is an energetic compound and it also incorporates characteristic moieties (see figure 3-1) found in nitramine-type energetic materials like RDX or in TNT.

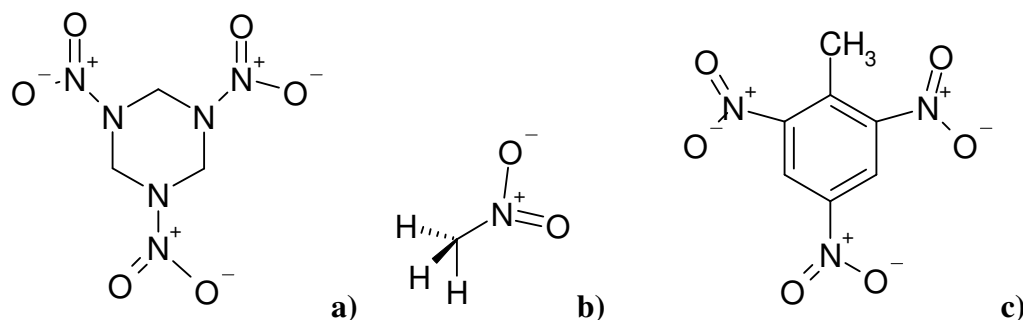
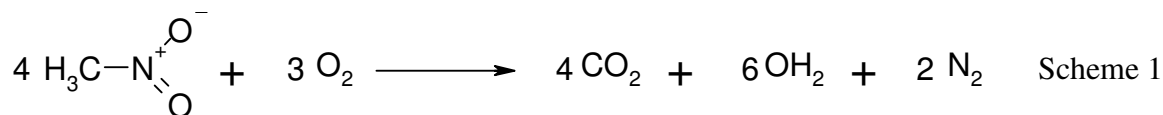


Figure 3-1 Chemical structure of a) RDX (Cyclonite, Hexogen), b) nitromethane and c) TNT

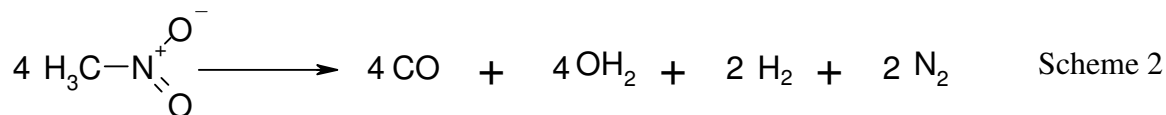
While being an important solvent for analytical chemistry and a reactant in organic synthesis, nitromethane can be also used as a propellant in liquid fuel rockets, where it can replace the hydrazine monopropellant thanks to its high performance and reduced toxicity. Although it is a high-energy monopropellant, it is stable enough for long term storage, and thanks to its low toxicity during packaging and handling, it is an attractive replacement for hydrazine in space thrusters. CH_3NO_2 can be combined with

other oxidizer-rich components to form mixtures for bi-propellant propulsion applications.⁷² Its performance is reported to be significantly better than hydrazine and hydroxylammonium nitrate monopropellants.⁷³ Nitromethane can also be used as a component in liquid explosives, for example, PLX (Picatinny Liquid eXplosive).⁷⁴ In everyday life nitromethane can be used as fuel for internal combustion engines, though it is relatively expensive compared to oil distillates. Thus it is only used in high-performance applications such as fuel for drag racing Top Fuel Cars, where the engine is running rich and using the internal oxygen of NM to complete combustion.⁷³ In small scale model cars, airplanes and boats that use internal combustion engines, the fuel is usually methanol mixed with nitromethane in order to supply relatively high energy for the engine size. Its use is easily noticeable in the exhaust's distinctive tangy, suffocating smell. It is the simplest CHON molecule containing nitro groups, making it useful as a prototype for more complex energetic materials in reaction, and combustion, studies.^{75,76} CH₃NO₂ has the following properties: a molecular weight of 61.04 g/mol, density of 1.137 g/cm³ at 20°C, critical point of 588.15 K and 6.3126 MPa, freezing and boiling points (atmospheric pressure) of 244.6 and 374.35 K, respectively.⁴⁹

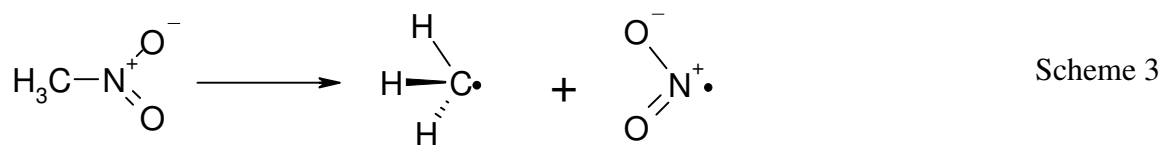
The commonly accepted path for CH₃NO₂ combustion is that producing N₂, CO₂, and water,



while decomposition in the absence of oxygen is believed to proceed via



The products of this second reaction are also the major equilibrium products, since experimental and theoretical studies of the combustion of nitromethane^{75,76} indicate that the most probable step in its decomposition is the breaking of the bond between C and N.



Other, “minor” products, like CH₂O, HNO, HONO, N₂O and some NO_x, also are expected, resulting from subsequent reactions of the radicals formed in the process (especially under non-ideal conditions). We also have examined an even simpler model of nitromethane, taking the methyl and nitro groups to be spherical units (diatomic like behavior). The potential parameters describing the interaction of these spherical units with the gaseous projectile was taken from the JZCS database.⁷⁷

The second part of this chapter describes the simulations done on rigid-body and fully flexible models of nitromethane liquid (in order to establish the importance of the internal degrees of freedom in dissipating energy from the collisions) as well as on the simplified “diatomic” system. The third part discusses our findings.

II. Simulations

Nitromethane, our model energetic material, is a molecular liquid with a molecular mass of 61.04 g/mol. (For incident Ar the mass ratio μ , discussed in the previous chapter therefore is equal to 0.65) Unlike other energetic materials that are structurally more complex, a NM molecule has only 15 internal degrees of freedom, few enough that an optimized potential energy surface is available.⁵⁸⁻⁶⁰ The intramolecular

interaction potential is described as the sum of bond stretch, angle bend and dihedral (or torsion) potentials:

$$V_{in} = V_{bond} + V_{angle} + V_{dihedral} \quad (8)$$

The bond stretches are described by Morse potentials:

$$V_{bond} = E_0 \left[\left\{ 1 - \exp(-k(r_{ij} - r_0)) \right\}^2 - 1 \right] \quad (9)$$

where r_{ij} is the bond length, r_0 is the equilibrium bond distance, E_0 is the bond dissociation energy, and k is a measure of the potential curvature. There are six bonds in the molecule described this way. In modeling the angle bends (there are 9 of them describing changes in the HCH, HCN, CNO and ONO angles), harmonic potential functions were used as shown below:

$$V_{angle} = \frac{k}{2} (\theta_{jik} - \theta_0)^2 \quad (10)$$

where k is the force constant, θ_{jik} is the angle of interest, and θ_0 is the equilibrium bond angle. Finally the dihedral angles, indicating the orientations of the methyl and nitro groups with respect to rotation about the C-N bond, are approximated by a cosine-type torsional potential function:

$$V_{dihedral} = A [1 + \cos(m\phi_{ijkn} - \delta)] \quad (11)$$

where A is equal to half of the intramolecular torsional barrier, ϕ is the dihedral angle, δ is a fitting parameter, and $m = 2$ or 3 . Altogether there are seven dihedral potential terms, six describing the H-C-N-O angles and one describing the N-O-O-C angle.

The other important part of the full potential is the intermolecular potential for the liquid, which is described using Buckingham potentials and Coulombic interactions with fixed partial charges on the atoms.

$$V(r_{ij}) = A \exp\left(-\frac{r_{ij}}{\rho}\right) - \frac{C}{r_{ij}^6} \quad (12)$$

where A and C are parameters related to the well depth and ρ is a shape parameter. The complete list of parameters can be found in Refs. 58 and 59.

To describe the interaction between the atoms of the liquid and the impinging gas particle, we used a Lennard-Jones interaction potential (eq 1), using the conventional Lorentz-Berthelot combining rules mentioned in the previous chapter. The specific parameters applicable to this work are the following:

Table 3-1. Lennard-Jones parameters used to describe gas-liquid interaction in the scattering simulations

Interaction	ϵ (kJ/mol)	σ (pm)
Ar-Ar	0.99572	341
Ar-C	0.31869	352.5
Ar-H	0.13010	315
Ar-N	0.27145	332.5
Ar-O	0.34854	317.5

To validate our simulation code as modified and to ensure that our modifications have not introduced inadvertent errors in the original simulation process, we carried out a simulation in which we melted the nitromethane. We obtained good agreement between our results and the result found in the literature.⁵⁸ In this simulation the nitromethane's starting structure consisted of 240 molecules (1680 atoms) in an orthorhombic arrangement from which we began a constant temperature equilibration at 360 K. The simulation cell was expanded in the z-direction to 80Å right before the first simulation in order to avoid complications that would be caused by the application of periodic boundary conditions if instead we were to first “melt” the nitromethane and then later to

create and thermally equilibrate a surface. Since this is a periodic molecular system and a molecule may extend across a simulation cell boundary (i.e. parts of the molecule appear at the opposite sides of the cell), an arbitrary expansion of the box could cause unwanted and unrealistic fragmentation of the molecules. The constant temperature simulations were run for 500000 steps (with a time step of 0.0005 ps, this simulation was carried out for a clock time of 250 ps), and density profile data was accumulated. We also saved 100 well-separated configurations for use as initial conditions for the scattering trajectories. After further expanding the box along the z-axis to 100 Å, an argon atom was introduced in the same way as in the case of the liquid indium system. Separate simulations were carried out with initial Ar incident kinetic energies of 92 kJ/mol and 12.5 kJ/mol; in both cases, the impact angle was 55°. We collected 800-1000 trajectories for the scattering studies at each initial Ar energy.

As mentioned above, the first step in the fragmentation of nitromethane is thought to be the breaking of the C-N bond. In order to see if the collisions in our system can lead directly to bond breaking (in the absence of switching functions that “turn off” the angle terms in the potential as the C-N bond breaks, the potential is non-reactive), we created a simplified molecule, for which we only kept the C-N bond stretch potential (the Morse potential itself is reactive) and in which the H₃C- and O₂N- groups are represented by spheres. To describe the intermolecular interaction between the H₃C- and O₂N- groups and the Ar gas atom, we adopted parameters from the JZCS database⁷⁷ applicable to a potential of the following form:

$$V(r) = \varepsilon \left[\left(\frac{6}{\eta - 6} \right) \exp[\eta(1 - r/r^*)] - \left(\frac{\eta}{\eta - 6} \right) \left(\frac{r^*}{r} \right) \right] \quad (13)$$

where $\eta = 13$, ε is the well depth (ε_{ij}) and $r^* = \sigma$ from eq 1 (the inner radius where the

Lennard-Jones potential goes to zero). In DL_POLY the most similar potential functional form is the Born-Huggins-Meyer potential, which we adapted to reproduce the form of equation 13 as follows:

$$V(r_{ij}) = A \exp[B(\sigma - r_{ij})] - \frac{C}{r_{ij}} - \frac{D}{r_{ij}^6} \quad (14)$$

where the parameters are as follows $A = \epsilon \left(\frac{6}{\eta - 6} \right)$, $B = \eta/\sigma$, $C = \sigma \left(\frac{\eta}{\eta - 6} \right)$, and $D = 0$.

This “diatomic” simplified nitromethane system was initially equilibrated the same way as the one described by the full potential function, but at a temperature of 300 K, with 100 configurations again being saved. Three simulations were then carried out in which an Ar atom was introduced to the system with an initial kinetic energy of 92, 250, or 350 kJ/mol and at an incident angle of 0°. Later, we heated the “diatomic” system to the same temperature used in the full nitromethane simulations and set up two simulations at 12.5 and 92 kJ/mol initial projectile kinetic energies, one set that included an attraction between the gas atom and the liquid species, and one that did not, with 1000 trajectories being included in each simulation.

Finally, we included a further system in our investigations, one in which the nitromethane molecules were taken to be rigid bodies, thus providing a model of a liquid with no internal vibrational degrees of freedom. Our goal here was to determine what fraction of the collisional energy transfer is channeled into the vibrational modes of the liquid molecules. The preparation of the system followed the same procedure that was used in initializing the flexible nitromethane simulations. In these final scattering simulations, an initial incident atom kinetic energy of 12.5 kJ/mol was used.

III. Results

For the fully flexible nitromethane system, our first step was to calculate a density profile along the z -axis for the melt. Such a profile is useful because it gives an indication of the extent of the bulk melting, and also roughly describes the features of the surface. Since NM is a three-dimensional molecular system and contains different numbers of the four atomic species within the molecule, in order to get a molecular number density profile, we have calculated a weighted (weighted by the number of the given atomic species per nitromethane molecule, 3 for H, 2 for O and 1 for both N and C) average of atomic number densities, the result being shown in figure 3-2.

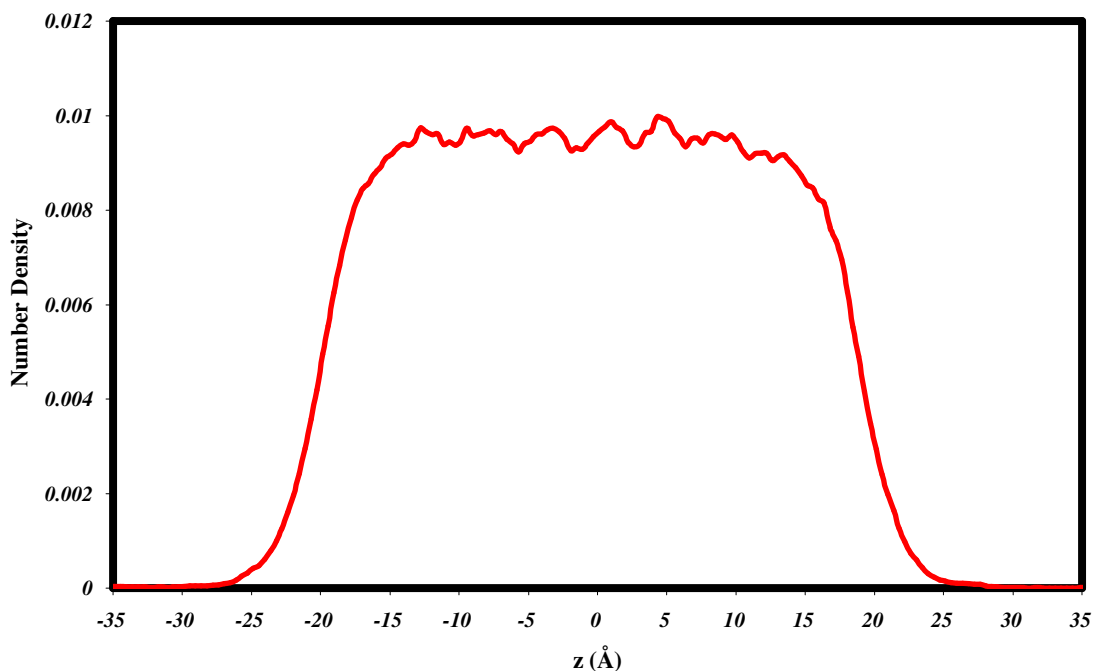


Figure 3-2. Density profile of liquid nitromethane after 500,000 steps at 360 K

The density profile of nitromethane is found to be much rougher than the ones obtained for indium. If we compare it to previous results, it most resembles the one for the Lennard-Jones system at the second-highest temperature (511 K) in that they have a

similar surface width (approximately 8 Å). But unlike the atomic liquid, the bulk of the molecular liquid appears to be somewhat structured.

This structure observed in the bulk is interesting, since 360 K is much higher than the melting temperature of the neat nitromethane (244.6 K). Furthermore, although we started from a structure that describes the perfectly crystalline solid and investigations⁵⁸⁻⁶⁰ have shown that these crystals melt at a higher temperature (superheating) than the usually obtained polycrystalline material the equilibration temperature used here is still higher than the melting temperature obtained by Thompson and co-workers (~338 K) using the present potential energy function. A probable reason for fluctuations in the density of the bulk liquid, which seems periodic, is that unlike the atomic liquid, nitromethane has a three dimensional structure and might form small associations in the liquid phase which give an internal structure to the bulk. Since the density fluctuations in the bulk are not sharply pronounced we can still assume that it is not a solid, but a liquid, structure. Since the nitromethane consists of two different groups (-CH₃ and -NO₂) at each end, the density profiles might provide information about the molecule's orientation at the surface. If there is a preferred orientation, which group is oriented towards the bulk?

To look at the surface structure, we plotted the parts of the C and N number density contour and also the analogous H and O weighted number density contour over the transition regime from bulk liquid to vapor (figures 3-3 and 3-4, respectively). To determine which part of the molecule prefers to face the vapor-phase we focus on the part of the plot which is farthest from the bulk but not clearly pertaining to the vapor phase, operationally where the contour becomes concave upward. The graphs show that both C

and H have somewhat higher (~8%) number density on both outermost surfaces than do N and O (which would suggest a preference for methyl groups to be oriented away from the bulk at the surface, but these are really small differences and we cannot justify this conclusion).

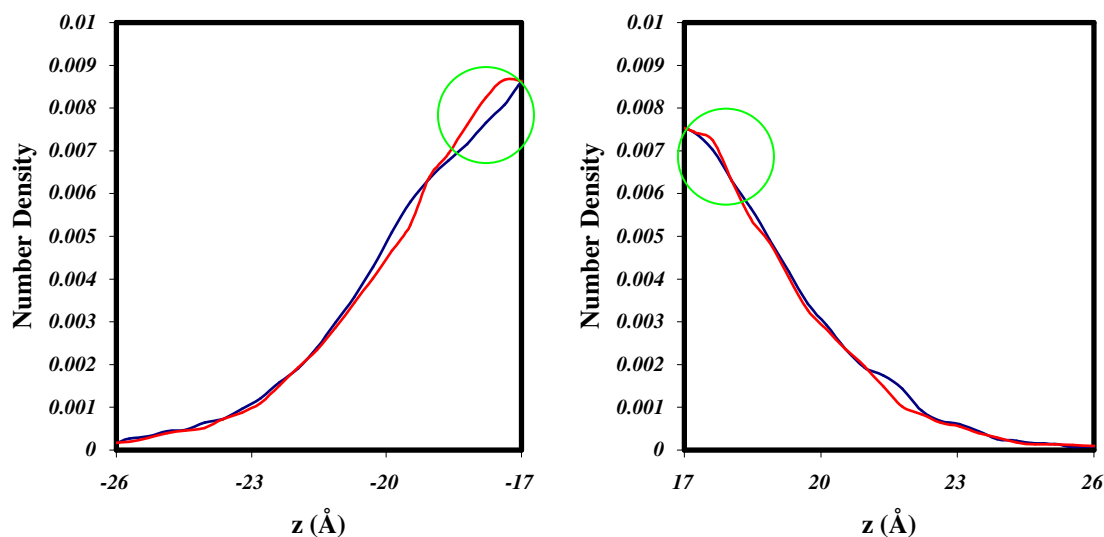


Figure 3-3. Density profiles of C (blue) and N (red) at the $-z$ and $+z$ surfaces

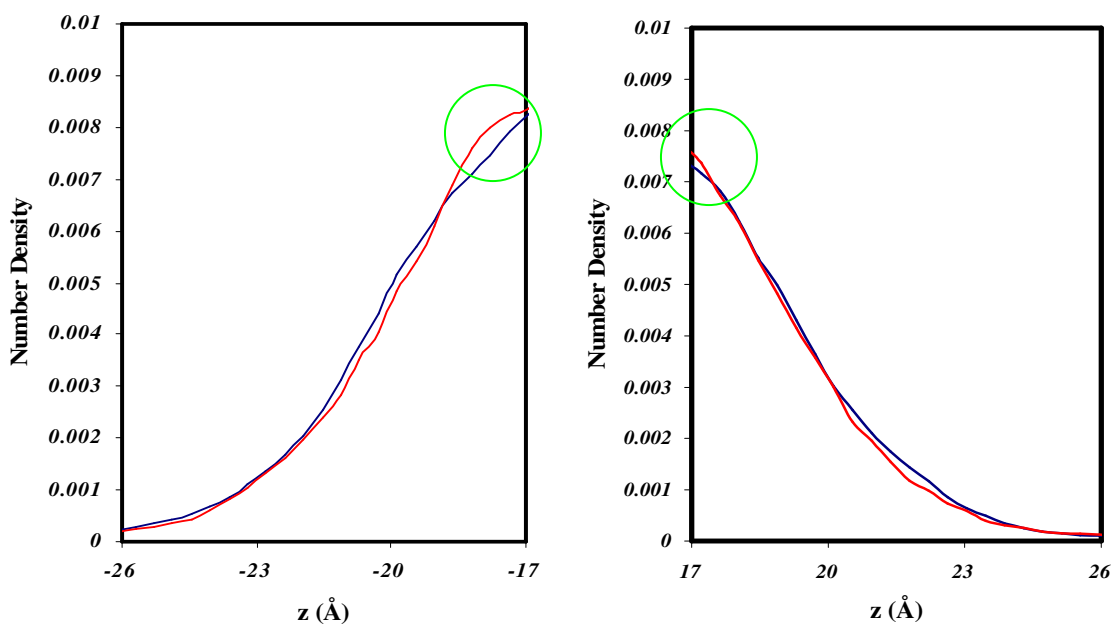


Figure 3-4. Weighted density profiles for H (blue) and O (red) at the $-z$ and $+z$ surfaces

In the outermost bulk layer though, we see a much more pronounced preference for the opposite orientation (green circles), suggesting a preference for the nitro groups (of the nitromethane molecules in the outermost bulk layer) to be oriented toward the surface layer. Because of the small differences, the orientation at the surface is nearly random, but suggests that the topic might be worthy of further investigation in other systems.

The z-direction density profile also contains the information required for calculating the equilibrium vapor pressure of nitromethane. Using the ideal gas equation and the density profile magnitude well away from the bulk liquid, at 360 K, we obtained a vapor pressure p_{vap} of 0.606 atm. This is a reasonable value; using the literature value of the vapor pressure at 298 K value and the enthalpy of vaporization ($\Delta_{\text{vap}}H^\circ = 38.36$ kJ/mol),⁴⁹ we obtained a “literature” vapor pressure of 0.65 atm by substitution into the Clausius-Clapeyron equation. We also wondered if we could determine a reasonable value for the enthalpy of vaporization of nitromethane based on calculated vapor pressures. Thus we carried out a series of equilibration calculations at temperatures in the range 300-350 K. Unfortunately, even the vapor pressures calculated after different equilibration times at the same temperature fluctuated considerably, and we were not able to obtain a reliable $\Delta_{\text{vap}}H^\circ$ value.

The smaller time step and more complex force description radically increase the computational time necessary for these simulations. In the time needed to obtain 4000 trajectories of the indium system, only 10-20 trajectories can be computed for the nitromethane system. To aid in the statistical analysis we ran multiple sets of 100 trajectories each, the results of which were later united. The following figures indicate the

fluctuations obtained in these simulations, and suggest the minimum and optimum number of trajectories necessary.

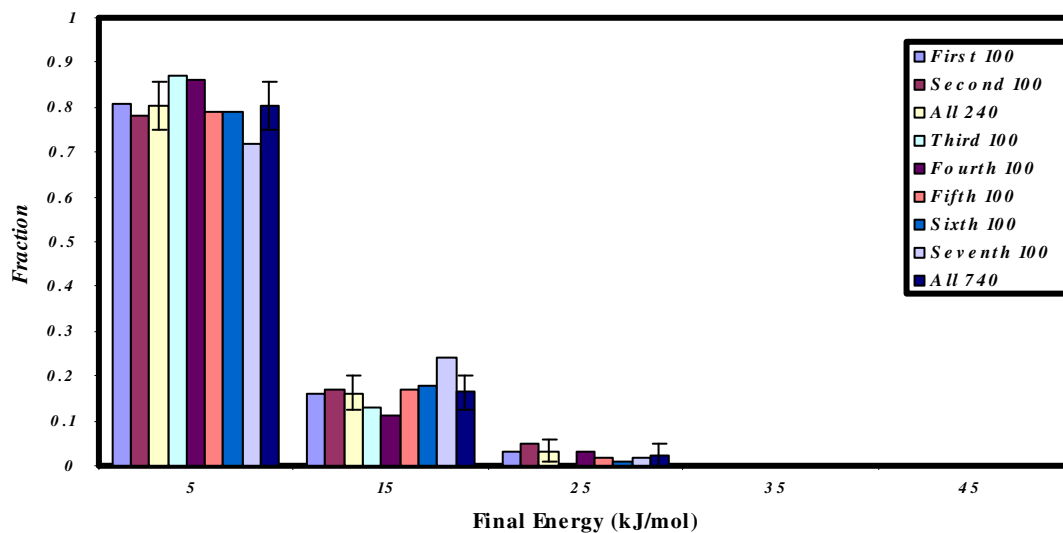


Figure 3-5. Convergence of the final energy distribution of all projectiles with increasing numbers of trajectories. ($T_1 = 360$ K, $\theta_i = 55^\circ$, $E_i = 12.5$ kJ/mol)

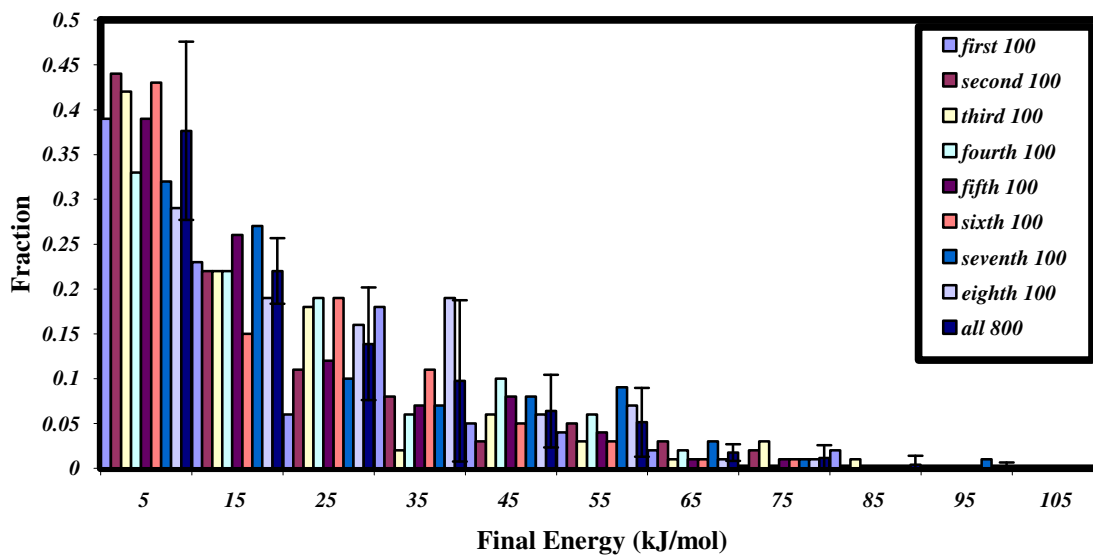


Figure 3-6. Convergence of the final energy distribution of all projectiles with increasing numbers of trajectories. ($T_1 = 360$ K, $\theta_i = 55^\circ$, $E_i = 92$ kJ/mol)

Although the number of trajectories is smaller than that routinely calculated in the studies of the previous chapter, the convergence of the final energies is nonetheless remarkably good. The distribution changes little, the variations being within the order of the error bar applicable to each individual set. The graphs clearly show a significant energy loss by the incident Ar atoms. This result encouraged us in believing that gathering 800-1000 trajectories is the optimal way of balancing computational time and statistical accuracy.

As mentioned in the introduction above, the primary fragmentation step of the decomposition of CH_3NO_2 is the breaking of the C-N bond, resulting in $\cdot\text{CH}_3$ and $\cdot\text{NO}_2$ fragments, which later through complicated multi step reactions recombine to form the main deflagration products: water, CO, H_2 and N_2 . We naturally wondered, therefore, whether collisional energy transfer might lead to direct fragmentation of this bond in the condensed phase. Although the potential function for the flexible nitromethane system is non-reactive, the bond stretch part of it, a Morse-potential, would allow separation of two previously connected atoms. To further simplify the system, we devised a “diatomic” model, in which only the bond between the C and N was kept from the original potential function, while the methyl and nitro groups were each modeled in a “united atom” fashion. In order to maximize the likelihood of collisional dissociation, we chose an incident angle of 0° and omitted any attractive interaction between Ar and the liquid species. In this study, we considered three initial kinetic energy settings for the projectile. The first energy chosen was 92 kJ/mol, which provide a base line with which to compare the results of the higher initial energy collisions (250 kJ/mol and 350 kJ/mol). The simulations were run at a liquid temperature of 300 K. We plotted the final energy

distributions of all particles as well as those that were scattered (figs. 3-7 and 3-8) looking for a characteristic energy uptake by the system that might indicate cleavage of the bond.

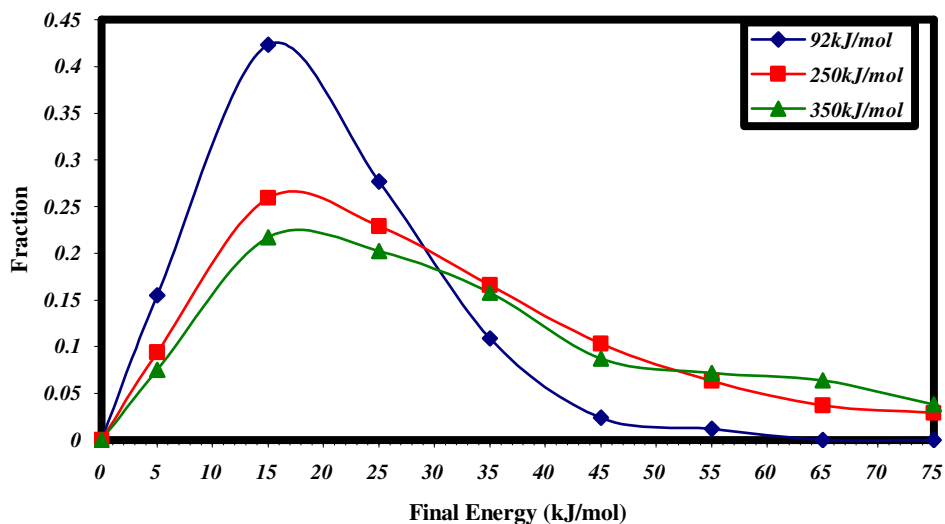


Figure 3-7. Final energy distributions of all particles collided with the simplified “diatomic” liquid. ($T_l = 300$ K, $\theta_i = 0^\circ$)

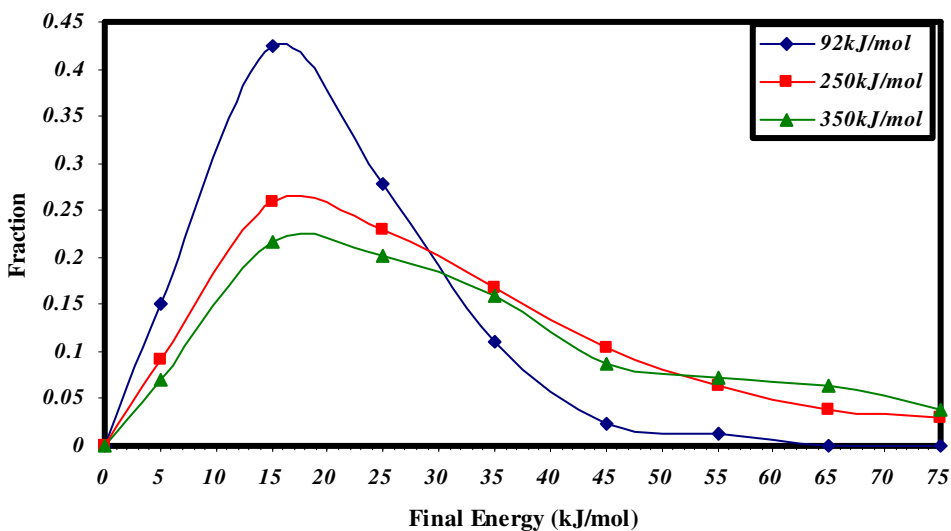


Figure 3-8. Final energy distributions of the particles scattered from the simplified “diatomic” liquid. ($T_l = 300$ K, $\theta_i = 0^\circ$)

Clearly a large fraction of the incident energy is transferred in all the cases. Note in particular that the energy distributions of the scattered particles are very similar to those applicable to all the projectiles, a result indicating that very low trapping is expected in the absence of attractive interactions. As one expects, the higher the initial energy the larger the number of scattered particles detected with higher final energy. There was no signature of a characteristic energy being transferred, suggesting that dissociation cannot be stimulated by collision. This result was affirmed by visual inspection of the collisions where, instead of dissociation, the excitation of the rotational states of the liquid molecules was particularly noticeable. The parts of the diatomic molecules in the bulk liquid are difficult to separate because even if energy does flow into the vibration, it is quickly dispersed among the neighbor molecules inside the bulk through collisions.

A further use of this model system involved an evaluation of the effect of the attractive potential. These simulations were run at 360 K to ensure compatibility with the rest of the nitromethane simulations. Two sets of calculations were run, each with two initial kinetic energies of the projectile (12.5 and 92 kJ/mol).

The model system behaves much like the previously studied Lennard-Jones system does. As the attractive interaction energy between the molecule and the gas particle increases, the number of scattered species diminishes. While at zero attractive interaction the scattered species obviously dominate the final energy distributions, the opposite is true when we switch the attractive potential on.

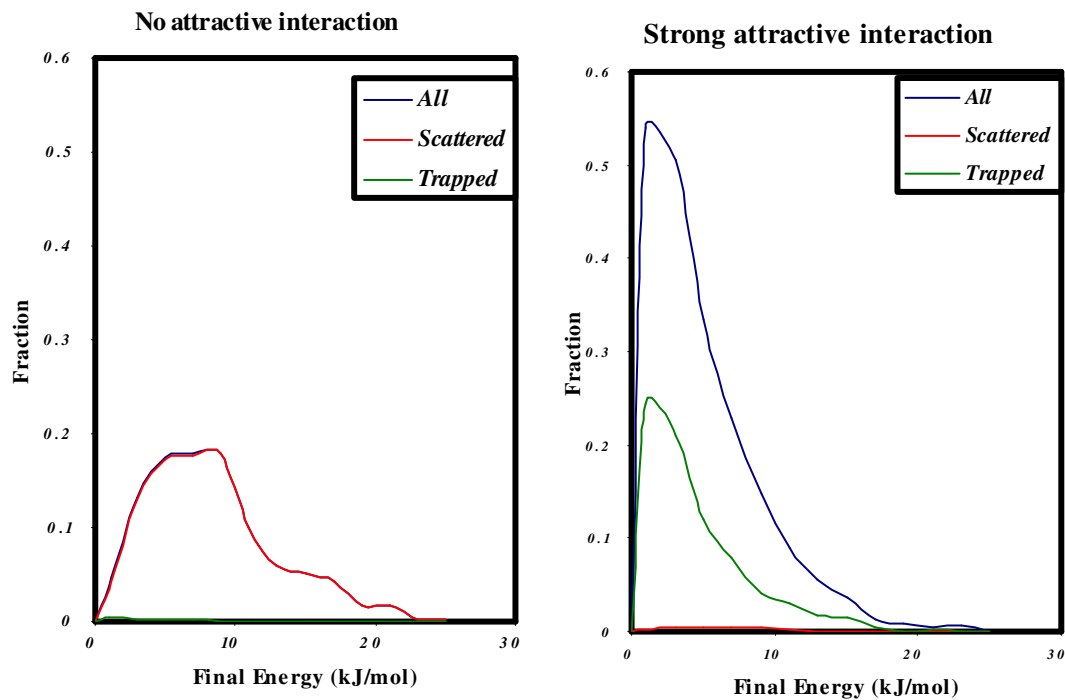


Figure 3-9. Energy transfer in the model system at gas-liquid interaction strength limits.
($T_1 = 360$ K, $\theta_1 = 0^\circ$, $E_i = 12.5$ kJ/mol)

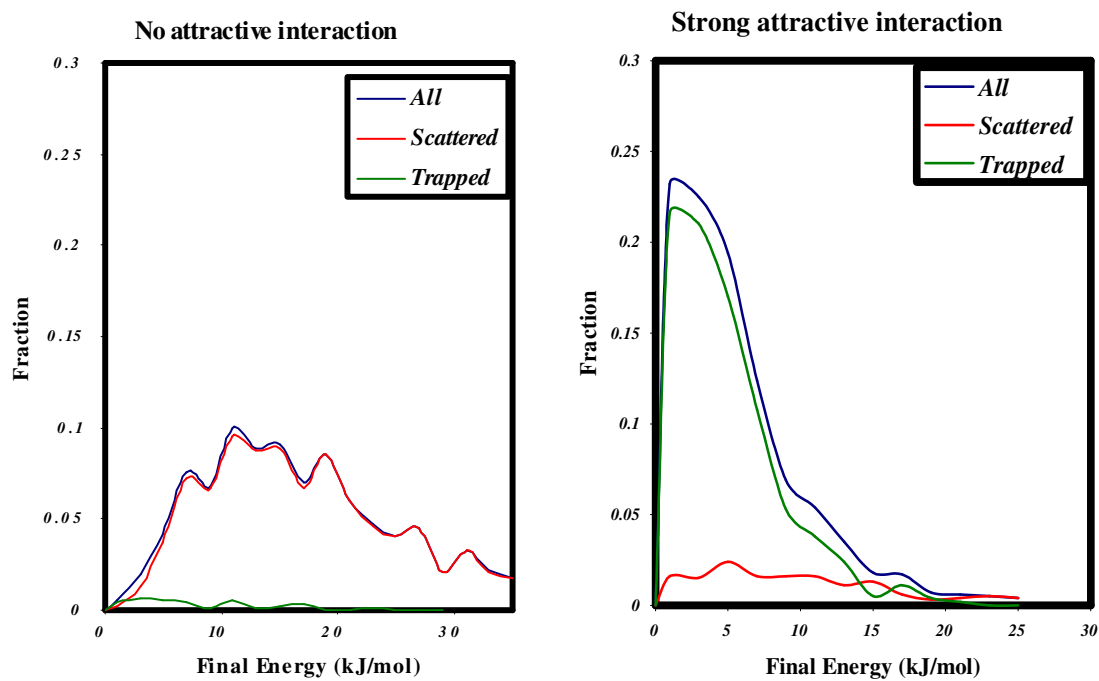


Figure 3-10. Energy transfer of the model system at gas-liquid interaction strength limits.
($T_1 = 360$ K, $\theta_1 = 0^\circ$, $E_i = 92$ kJ/mol)

Fitting Maxwell-Boltzmann distributions to the energies of the scattered particles and calculating the trapping probabilities and the energy accommodation coefficients, we can describe this behavior numerically. Table 3-2 summarizes the findings.

Table 3-2. Effect of the gas-liquid attractive interaction strength on the scattering behavior.

E_i (kJ/mol)	No attractive interaction	Strong attractive interaction*
12.5=4.18 RT_1	$T_f = 1.7T_1$; $\alpha = 0.62$; trapping: 1%	$T_f=1.2 T_1$; $\alpha=0.89$; trapping: 76.7%
92=30.74 RT_1	$T_f=4.2 T_1$; $\alpha=0.84$; trapping: 3.5%	$T_f=1.7 T_1$; $\alpha=0.96$; trapping: 84.1%

*The interaction between the Ar atom and the liquid surface is described by the potential of the form in eq. 14 with parameters used from ref. 77.

As we can see, we have very efficient energy transfer in all these systems, especially when we consider that at zero well depth we have a very low trapping probability. Another similarity with the Lennard-Jones prototypical system is that here also the trapping probability is not zero in the absence of an attractive gas-liquid potential. An interesting but not unexpected feature of these results is that the efficiency of energy transfer increases as we increase the initial kinetic energy of the projectile. Turning the attractive interaction off and on is resulting in significant changes for both incident energy cases; we see larger changes in the trapping probabilities and the final argon temperature for the higher incident energy simulations. The change in the thermal accommodation coefficient follows a similar trend, but it is for the lower energy projectile that the larger increase is observed.

To study the energy transfer in the fully flexible liquid nitromethane system, we used an initial incident kinetic energy of 92 kJ/mol, and we also ran simulations at a 12.5 kJ/mol initial incident energy, which is an energy that is more relevant to a combustion application. The 12.5 kJ/mol initial kinetic energy in case of Ar is

approximately equivalent to a collision with a 1000 K combustion product. The final energy distributions derived from this system are shown in figure 3-11. Figure 3-12 shows the final energy distributions obtained for the system with 92 kJ/mol initial incident energy.

Compared to the Lennard-Jones system results, the energy distribution of the trapped atoms peaks early and then decreases rapidly, indicating that the trapped species have lost most their initial energy. The position of the peak is even lower than what was found in the atomic liquid case; it appears below 5 kJ/mol. This result is a good indication of very efficient energy transfer. It is also supported by the plot of the scattered species, which also peaks at relatively lower energies. While previously the scattered particles had their distribution peak at about 20 kJ/mol, for the molecular system with $E_i = 92$ kJ/mol, the peak appears between 5 and 10 kJ/mol.

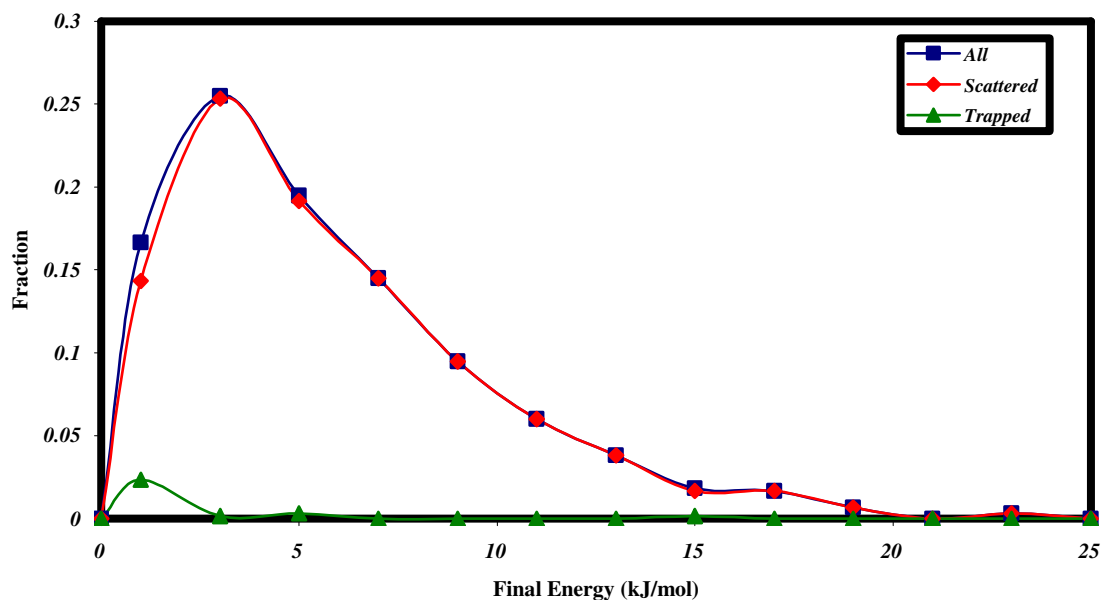


Figure 3-11. Distribution of final energies of atoms incident with 12.5 kJ/mol initial kinetic energy. ($T_1 = 360$ K, $\theta_1 = 55^\circ$)

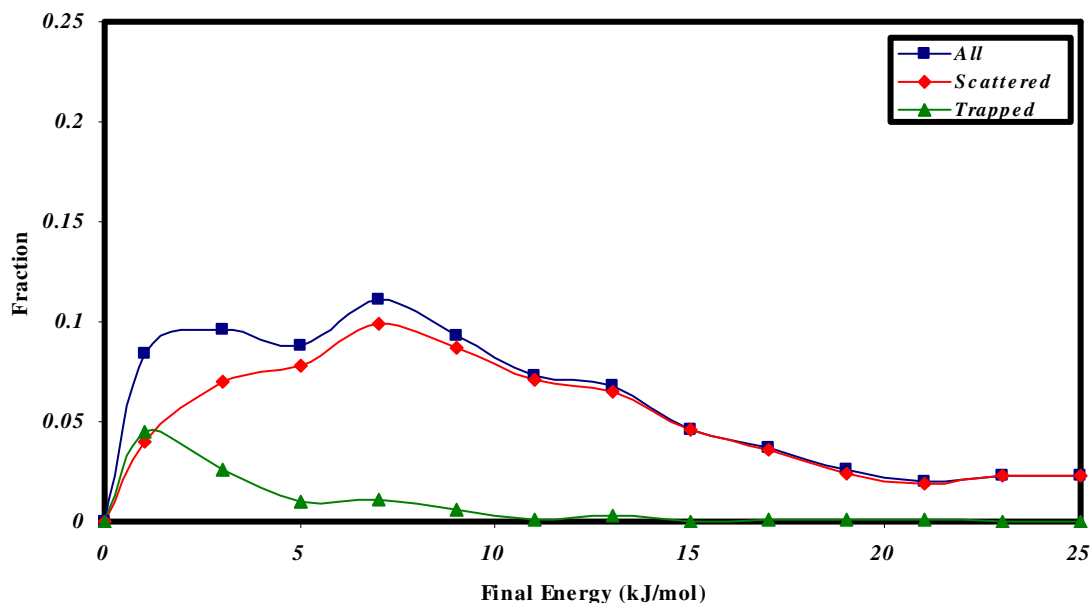


Figure 3-12. Distribution of final energies of atoms incident with 92 kJ/mol initial kinetic energy. ($T_1 = 360$ K, $\theta_i = 55^\circ$)

This result might also indicate that the attraction between the gas and the liquid is weaker for the molecular system than for the atomic system. It is also noteworthy, though, that in the nitromethane there are fewer vaporized particles in the space above and below the liquid, and thus there is a clearer flight path for the projectile approaching and leaving the surface. The fully flexible nitromethane system exhibits behavior (shown in figures 3-11 and 3-12) similar to that of the simplified model diatomic system, namely that increased E_i results in increased trapping probability. Another common behavior is that at higher E_i the height of the energy distribution peaks is substantially decreased. We have to admit that the odd shape of the scattered particle energy distribution curves, makes fitting the data to a Maxwell-Boltzmann distribution problematic. If we ignore this complication, though, we find that $\alpha > 0.95$ for both initial incident energies. The final energy distribution curves for the scattered atoms peak at a higher energy for the higher

initial kinetic energy trajectories, which is understandable given that the fraction of the energy transferred is similar (about 95%). The remaining ~5% of the initial incident energy is, of course, higher if the initial value itself is higher. The calculated trapping probabilities, 3% trapping for the 12.5 kJ/mol initial kinetic energy trajectories and ~11% for the higher initial energy trajectories, are in good agreement with the results obtained for the simple diatomic model system.

To gather further insight into the behavior of the system upon changing the E_i of the impinging particles, we have plotted the angular scattering distributions. Figure 3-13 shows the one-dimensional representation of the final angle distribution of the particles scattered from the liquid nitromethane surface. The values at the positive angle values belong to atoms scattering forward (in the +x direction); the negative angle values imply backscattering (in the -x direction).

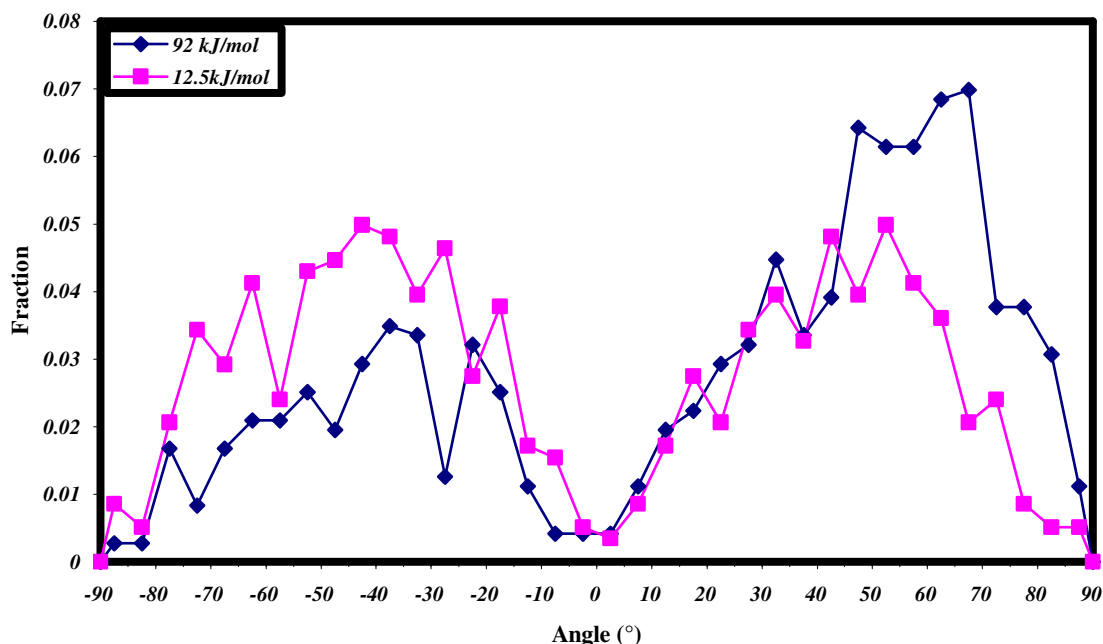


Figure 3-13. Final scattering angle distributions for Ar impinging on nitromethane, (fully flexible potential) $T_1 = 360$ K, $\theta_i = 55^\circ$

We see broad distributions of scattered angles here, but with pronounced double peaks describing backward and forward scattering. There is a probability of scattering off in all angles, but the scattering probability close to the normal is small. Most particles are scattered within $\pm 20^\circ$ of the specular and incident directions. The most significant difference between the scattering processes at the two incident kinetic energies is that the higher E_i process shows a clear preference for forward scattering, while the lower E_i process yields approximately symmetric forward and backwards scattering. This behavior is also clearly seen in the azimuthal angle distributions for the two processes, the results being shown in figure 3-14.

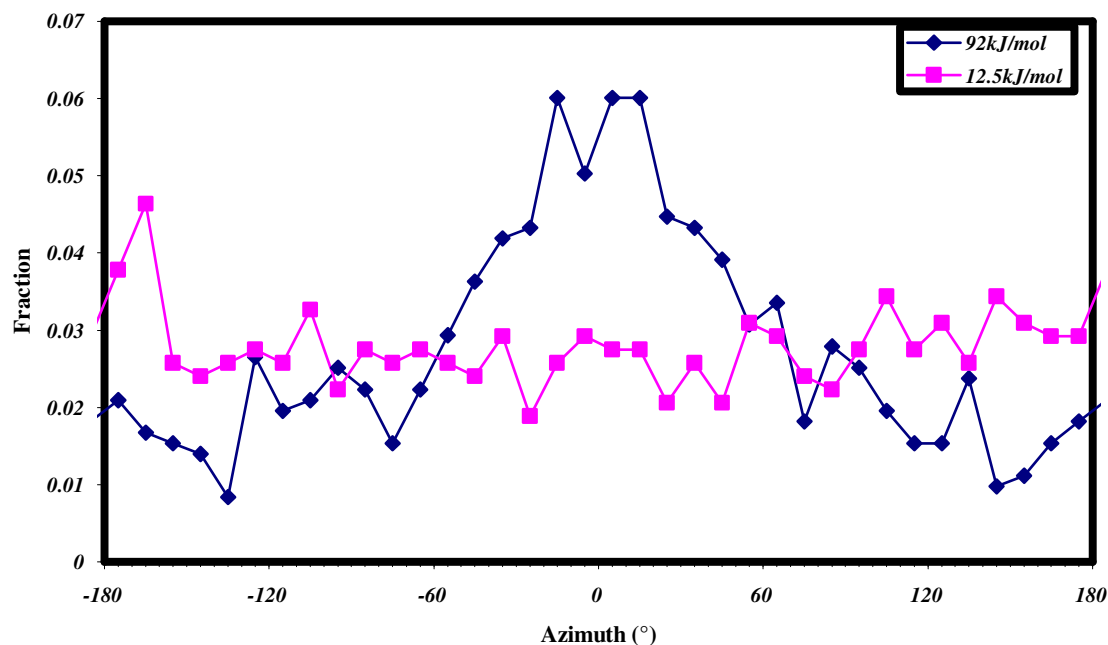


Figure 3-14. Final azimuthal scattering angle (ϕ) distributions for Ar scattering from nitromethane, (fully flexible potential) $T_1 = 360$ K, $\theta_i = 55^\circ$

The azimuthal angle distributions reinforce the conclusions drawn from the scattering angle distributions, the higher initial energy particles show a distinct preference

for in-plane forward scattering. The probability distributions suggest that the lower initial incident energy particles have a higher probability of losing their directionality. This may be the result of these particles experiencing the same surface being rougher than the higher E_i particles. Lower E_i results in lower initial velocity causing the Ar atoms to spend more time in the proximity of the surface interacting with the liquid. This is further enhanced by the relatively flat impact trajectory.

Do not let the angular distribution graphs mislead you. Though at a first look they may seem to indicate specular scattering as normally associated with elastic scattering (no energy transfer), the deflection angles and azimuths cannot be correlated through the probability distributions. In fact there are no trajectories where the projectile left the surface both in the plane ($\phi=0$) and at $\theta_f = \theta_i$; in some cases no trajectories were found with those exact scattered angles and azimuths. The non-zero probability in graphs 3-13 and 3-14 (also in graphs 2-7, 2-8, 2-10, 2-11, 3-17 and 3-18) at those angle values is only an artifact of the binning method used to calculate the probabilities.

Finally, we have investigated a rigid version of the nitromethane molecule to explore the effect of removing the vibrational degrees of freedom of nitromethane on the energy transfer dynamics. As always, we calculated the density profile along the axis perpendicular to the free liquid surfaces. The density profile of the rigid-body liquid closely resembles that of the fully flexible system, including a similar bulk structure. The graphs of the two systems do not overlap perfectly; the relationship of the plots to one another is similar to the relationship between Lennard-Jones liquids of different temperatures, with the rigid-body system here behaving as if it has a slightly lower temperature. The differences in the method, how the program calculates temperatures for

a rigid-body and a fully flexible system, might be responsible for the differences in figure 3-15.

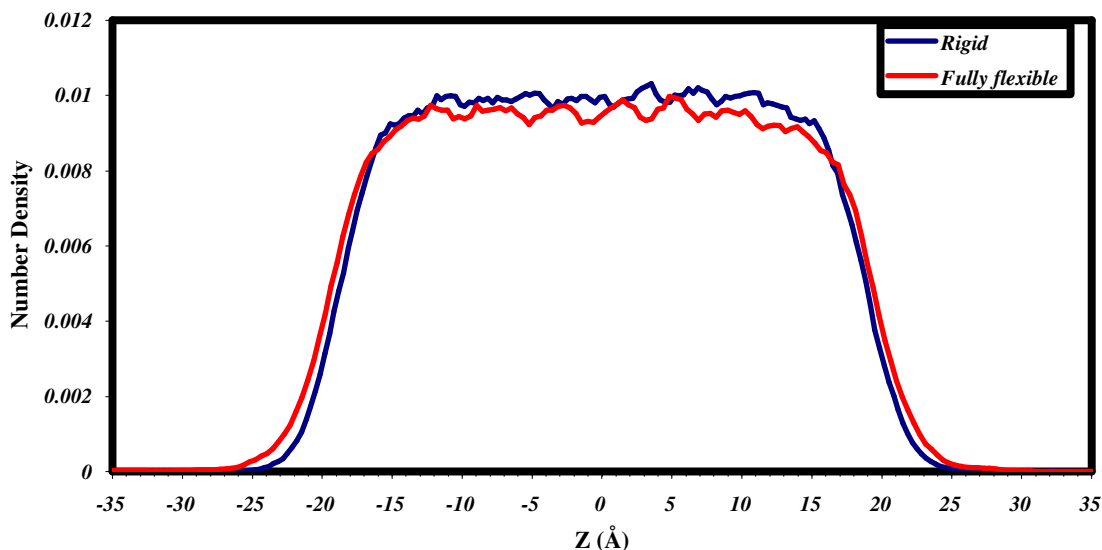


Figure 3-15. Density profiles of rigid-body and fully flexible liquid nitromethane averaged over 500,000 time steps at 360 K

After collecting the data from the scattering simulations from the rigid-body liquid surface, we generated energy distribution diagrams for the final energy of the argon atoms after interacting with this surface. In figure 3-16 we show the final energy distributions of all the projectiles as well as those for the trapped and scattered species subsets. The general shape of the plot is similar to the one pertaining to the 12.5 kJ/mol initial energy collisions with the fully flexible nitromethane surface at the same temperature. The energy distribution of the trapped species, in contrast, is broadened and increased in magnitude, indicating a higher probability of trapping. Indeed 9.1% of the incident Ar-atoms are trapped at the surface of the rigid-body liquid, whereas the fully flexible nitromethane surface only retains about 3% of the incident particles.

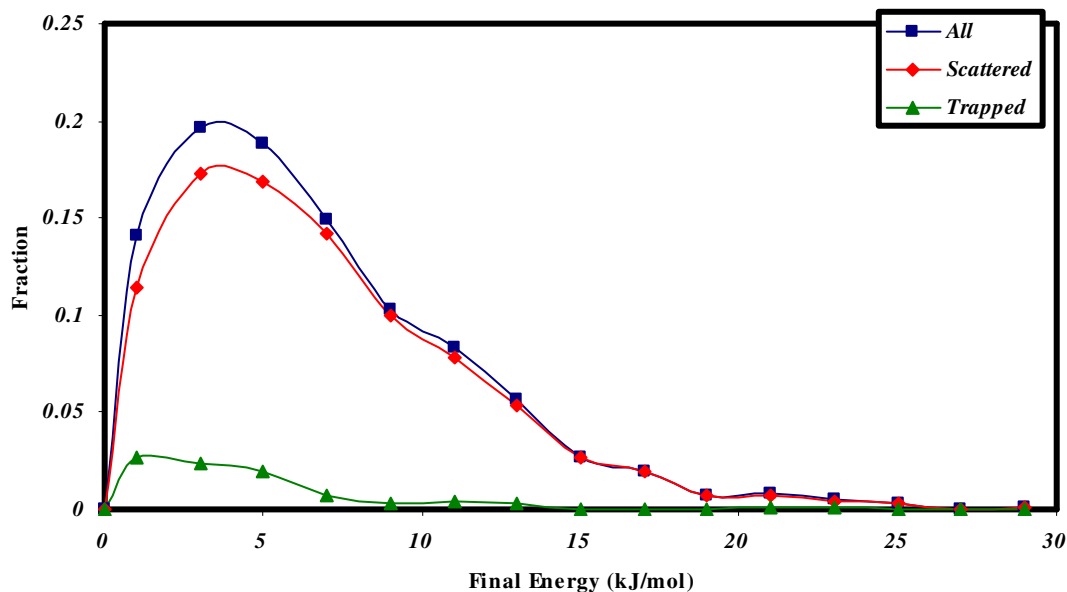


Figure 3-16. Distribution of final energies for atoms incident with 12.5 kJ/mol initial kinetic energy interacting with a rigid-body nitromethane liquid surface. ($T_i = 360$ K, $\theta_i = 55^\circ$)

The distributions attest to considerable energy transfer in good accordance with previous simulations performed using different versions of the molecular liquid. Fitting a Maxwell-Boltzmann distribution to the scattered particles' final energy distribution gives a final average temperature of 433.3 K ($1.2 T_i$), which is associated with a thermal accommodation coefficient (an approximate measure of the efficiency of the energy transfer) of 0.89. Comparing this result to the one obtained using the analogous fully flexible nitromethane system $\alpha = 0.97$, we might infer that the rigid body system is characterized by a less efficient energy transfer, just what might be expected as a result of removing the vibrational degrees of freedom that otherwise could accept the collision energy. On the other hand we also noted that trapping is more probable in the rigid body system.

The angular distribution of the scattered Ar atoms in the case of the rigid-body nitromethane liquid (again with an incident Ar kinetic energy of 12.5 kJ/mol) has a shape that is intermediate between the two plots obtained from the simulations of the fully flexible nitromethane system (corresponding to the two examined Ar incident kinetic energies). This low-energy scattering process shows some preference for forward scattering, but not to the degree seen in the high E_i case with fully flexible nitromethane. The graph of the azimuthal angle distribution of the scattered particles in the rigid-body system plotted in figure 3-18 shows a propensity for in-plane scattering that is intermediate between the results obtained for high- and low-energy scattering from the fully flexible surface.

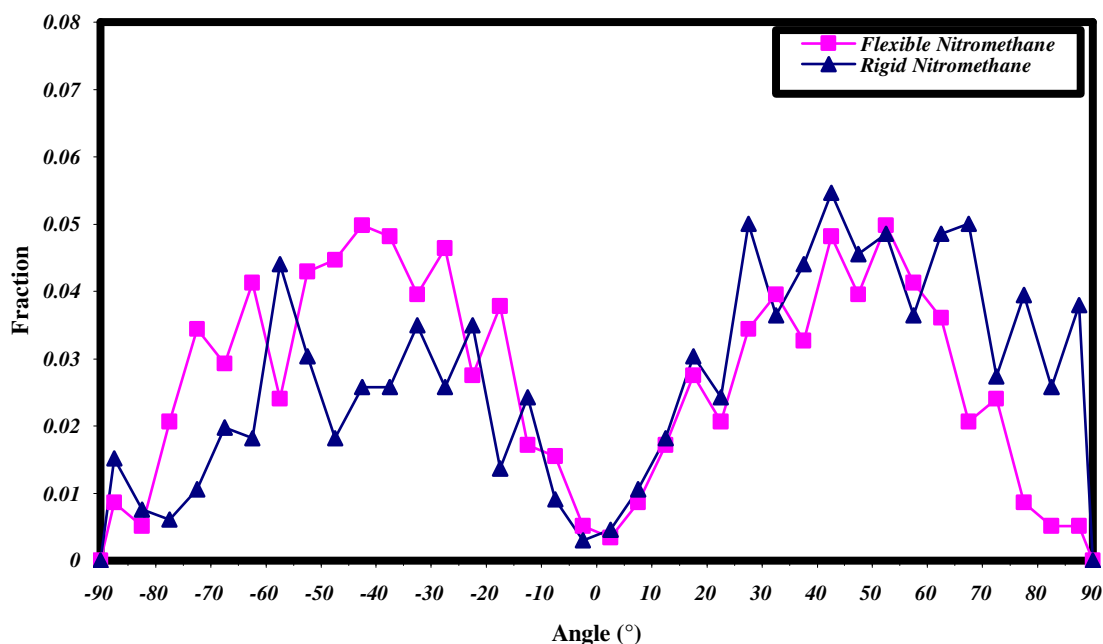


Figure 3-17. Final scattering angle distributions for Ar scattered from model nitromethane surfaces. $T_1 = 360$ K, $\theta_i = 55^\circ$, $E_i = 12.5$ kJ/mol

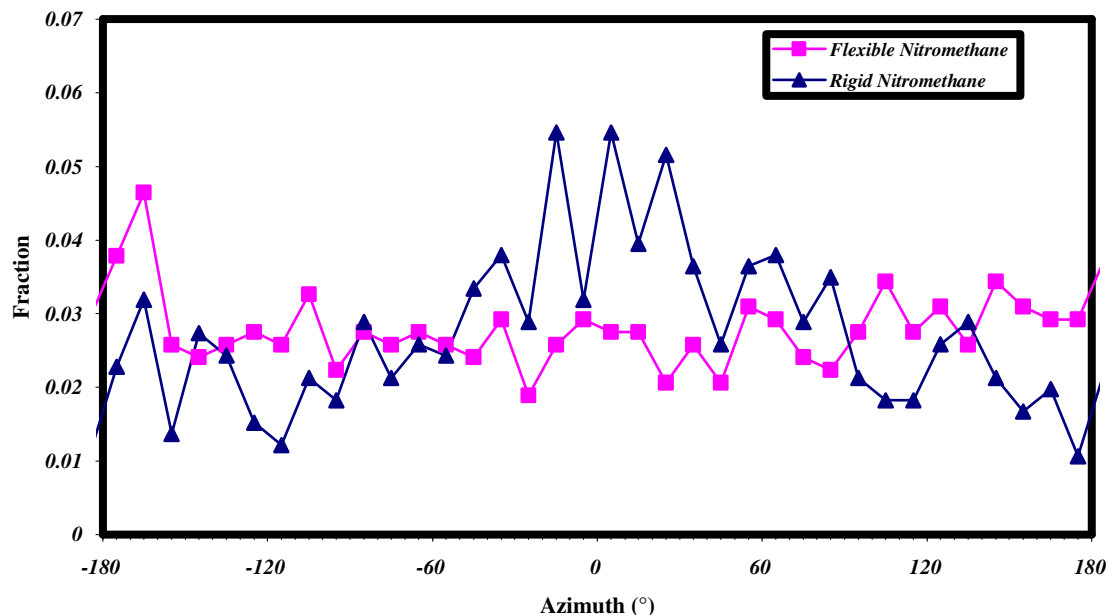


Figure 3-18. Final scattering azimuthal angle distributions for Ar scattered from model nitromethane surfaces. $T_i = 360$, K $\theta_i = 55^\circ$, $E_i = 12.5$ kJ/mol

The evaluation of the energy distribution diagrams for 12.5 kJ/mol Ar incident on fully flexible and rigid-body nitromethane liquid surfaces suggests the rigid-body liquid appears to be associated with less efficient energy transfer, but nonetheless it is characterized by higher trapping probability. The somewhat reduced energy transfer can be explained by the removal of the internal vibrational degrees of freedom. It must be noted, however, that even though the number of trajectories collected are sufficiently large for evaluation of the final energy distributions (as shown in figures 3-5 and 3-6), where the narrow range of final energies obtained ensure quick convergence, the lower number decreases the reliability of the angular distributions where a wide range of angles is observed. Thus only a qualitative comparison of the distributions of the scattered angle and azimuthal angle distributions obtained in the different simulations is justified.

The previous chapter showed us that in the case of a Lennard-Jones prototypical system, kinematic effects play an important role in collisional energy transfer. Although the molecular liquid in this case is more complex and considerably different from the original gas-solid scattering model for which the Baule formula was derived, we were intrigued by the prospect that the kinematic model yet has some relevance to collisional energy transfer to a nitromethane liquid.

The kinematic model predicts that the closer the masses of the colliding particles are to one other (i.e. the closer the mass ratio is to 1) the more efficient is the transfer of energy between them. We investigated this behavior in the previous chapter (see figure 2-14), where we found good agreement between the predictions of this simple model and the results of our simulations. The mass ratio of the collision partners in the Lennard-Jones system (corresponding to In and Ar) was 0.348, while in the case of liquid nitromethane the mass ratio is 0.65. This change in the mass ratio results in an increase in the first factor of the Baule formula ($4\mu/(1+\mu)^2$) from 0.77 to 0.96. In fact, we do find an increase in the efficiency of energy transfer in our simulations as we go from the atomic system to nitromethane.

Our simulations also indicate that the surface trapping (a factor we also use to describe the energy transfer) and the efficiency of energy transfer increase with increasing incident atom energy. This behavior was observed both in the diatomic model nitromethane and the fully flexible nitromethane systems. The Baule formula also predicts that increasing the projectile's initial kinetic energy should increase the fractional energy transfer (see the last fraction appearing in eq 6). Applying the kinematic approximation to an Ar-nitromethane system, we find that the first factor in the formula

gives the above mentioned value of 0.96 (corresponding to $\mu = 0.65$); the second factor, which describes the angle dependence, is approximated by unity (assuming a 0° impact angle); and the last factor, which accounts for the interaction well depth relative to the initial kinetic energy (in this case assume $V = 0$, $T_1 = 360$ K, and $E_i = 12.5$ kJ/mol) gives a value of 0.52, the net result is a fractional energy transfer, $\Delta E/E_i$, of 0.50. From the energy analysis of the scattered particles of the fully flexible nitromethane simulations with $E_i = 12.5$ kJ/mol, we get $\Delta E/E_i = 0.53$. For higher incident energy projectiles ($E_i = 92$ kJ/mol), the kinematic approximation yields a fractional energy transfer of 0.89. The simulation for this system gave the result $\Delta E/E_i = 0.89$. This good agreement tells us that, while the system is more complex and includes internal degrees of freedom that increased the ability of the liquid to dissipate a greater portion of the collision energy, kinematic effects still play a crucial role in the collision dynamics.

IV. Summary

As an extension of the simulations performed in the previous chapter, we considered atom scattering from a molecular liquid surface. The system of choice was nitromethane, because it is an energetic material in its own right and contains structural moieties of the most common nitramine-type explosives and propellants. It also has been extensively studied (an X-ray structure of the crystal and thermodynamical parameters are available, as well as results of combustion/deflagration experiments^{75,76}), and a high-quality force field has been developed for it, recently validated on the basis of melting simulations.⁵⁸⁻⁶³ To gain further insight, we also created simplified molecular systems

based on the original nitromethane model that isolated particular features of the dynamics.

The simplest model system considered was a “diatomic” representation of CH_3NO_2 generated by replacing the functional groups at the ends of the molecule with spherical representations of those groups, while retaining the important C-N bond, the bond that is most likely broken during degradation. This system was initially designed to probe the probability of bond cleavage being induced directly by collisions. The results, however, do not show evidence of a characteristic energy absorption related to dissociating the bond, suggesting that the nitromethane is not prone to dissociate even when the gas-surface collision energy is in excess of the C-N bond energy. Reaction initiation thus is likely to result from overall heating of the liquid rather than from dissociative collision events. Visual inspection of the individual trajectories suggested that gas collisions with the surface generally lead to energy being imparted initially into translation or rotation of the diatomics. This work was done in cooperation with a summer research fellow, Rachel Castleberry, who spent great time and effort setting up and analyzing the simulations, and who showed great interest and high motivation for working in the theoretical field.

Using the density data gathered during the thermal equilibration of the CH_3NO_2 liquid, we have attempted to deduce the orientation of the nitromethane molecules in the outermost bulk liquid layer. The density profiles obtained using the full nitromethane potential function and the rigid-body nitromethane model both show a slight preference for having the methyl groups oriented towards the vacuum, with any changing of this outermost bulk layer being neutralized by molecules in the surface layers.

A calculation of the vapor pressure above the surface of liquid nitromethane (full-potential) at a temperature of 360 K yielded good agreement with the value calculated using the Clausius-Clapeyron equation and readily available literature data. This favorable result prompted us to investigate further our ability to simulate vapor pressures by setting up a series of simulations that spanned the temperature regime 300 - 350 K. However, the vapor pressures we obtained from this fairly narrow temperature range were characterized by large fluctuations, and thus we were not able to deduce an enthalpy of vaporization using this approach. The difficulties here should not necessarily be attributed to deficiencies in the assumed force field, but rather to insufficient configuration averaging. Extended equilibrations starting from different original structures and extended sampling might yet make this approach viable.

The evaluation of the Ar scattering trajectories shows highly efficient collisional energy transfer, with the fraction of the incident energy transferred being much higher than in the case of the atomic Lennard-Jones system. This efficiency was maintained consistently throughout all the simulations performed with different variants of the full nitromethane system. The thermal accommodation coefficient α varied between 0.62 (for the diatomic system with no attractive interaction) to more than 0.95 in the case of the fully flexible nitromethane model. For the diatomic model system it is important to note that energy transfer is efficient both when the attractive potential between the impinging particle and the liquid molecule is large and when that potential is zero, although the trapping probability is quite different in these two limits. The rigid-body nitromethane system also exhibits efficient energy exchange. The systems with fewer internal degrees of freedom (both the diatomic model and the rigid-body system) are less efficient in

accommodating the Ar collision energy, than is the full nitromethane system, but not greatly so. We also suggest that the low trapping probabilities obtained for both the rigid-body and the full-potential systems (which share the same gas-liquid interaction description) is attributed to the weak gas-liquid interaction inherent to this system. This observation is supported by the results obtained using the diatomic model, which demonstrate a strong dependence of the trapping probability on the interaction well depth.

Finally, we have evaluated the applicability of the kinematic model of collisional energy transfer in this molecular system. As mentioned in the previous chapter an atomic Lennard-Jones system yields a value of the net average energy transfer far gas-liquid scattering that agrees well with predictions of the Baule model. Somewhat to our surprise, though, the kinematic approximation that describes the general structure of the energy transfer to an atomic liquid also yields a good description of energy transfer to a simple molecular liquid. A good agreement with the Baule formula was found in the simulations with the fully flexible nitromethane model, and also in the rest of the molecular systems, the energy transfer generally follows the predictions of the kinematic model. The fraction of energy transferred in general increases with an increase in E_i , a result also predicted by the Baule formula; the energy transfer also increases as the mass ratio μ approaches 1. Thus more efficient energy transfer is expected in Ar scattering from nitromethane ($\mu = 0.65$) than from In (Lennard-Jones model $\mu = 0.348$).

Chapter 4

Future possibilities

Steps have been taken towards scattering a rigid rotor projectile from a Lennard-Jones atomic liquid to illustrate other aspects of collisional energy transfer at a gas-liquid interface. In particular collisions of carbon dioxide molecules with a simple atomic liquid surface are to be investigated. The particular focus of these simulations is not in transfer of energy to the liquid surface, but rather on the transfer of an impinging molecules' initial kinetic energy into its rotational degrees of freedom. The CO₂ molecules are to be treated as rigid rotors, thus permitting isolation of the fraction of the initial (purely translational) kinetic energy flowing into rotations. The first phase of this work involves modifying the molecular dynamics code to incorporate molecular species rather than atoms as impinging particles and an evaluation of the rotational state of the molecules after leaving the surface. This work has been started with the help of Michael Valliere, an undergraduate research fellow. The selection of the initial parameters is based on the work of Perkins and Nesbitt.⁷⁸

The vapor pressure calculations using the calculated density profiles also needs further exploration. A follow-up study should focus on improving the reliability of the estimation of vapor pressures by the use of extended equilibrations of different original structures and extended sampling. These steps should yield improved statistics and thus more reliable values.

Also related to the evaluation of the density profiles is the determination of the orientation of molecules at liquid surfaces. The results so far have not shown an overwhelming preference in orientation for the nitromethane system, but liquids with more prominent dipolar or amphiphilic properties may show a stronger preference.

The modifications underway for incorporating CO₂ as a projectile can be extended to a more complex system. In the future, this could provide an opportunity to conduct studies of a reactive system.

Appendix A

Simulating scattering processes with DL_POLY_2.14

Modified and added subroutines for DL_Poly_2.14

The original code was modified to incorporate the parameters associated with an impinging species describing the initial state of the scattering process (initial kinetic energy E_i , angle of incidence θ_i). Without compromising the original capabilities of the program package, we adapted it to calculate the initial x-, y- and z-directional velocities of the projectile from the supplied angle and energy values and to evaluate the final (post-collision) energetics of the particle. Each trajectory begins with the projectile positioned randomly in the x-y plane above the surface, with the liquid species configuration being chosen from a file of 100 “snapshots” stored in a preliminary NVT simulation. To distinguish between the trapped and scattered particles, we imposed multiple criteria. First a distance from the surface was selected (large enough that there were no residual interactions between the surface atoms and the particle) as a counting-surface, simulating the presence of a detector at a distance from the surface. We also set a maximum trajectory time, but did so realizing that particles scattered to grazing angles may not quite reach the counting-surface by the time the trajectory was stopped. Thus, if at that time the initially incident atom was moving with a velocity that would take it away from the surface and there were no forces acting on the atom, the atom was included as scattered rather than trapped.

Modified Files: dl_params.inc; dlpoly.f; error.f; makefile; quatqnch.f; quench.f; simdef.f; sysdef.f; systemp.f; traject.u.f; vscaleg.f

Added Subroutines:

posread.f (reads in saved surface configurations)

recenter.f (re-centers the bulk in the simulation cell)

reset.f (resets the system at the end of a trajectory; calls for a new surface configuration, sets a new random starting position for the impinging species, and calculates the final kinetic properties of the projectile)

scatter.f (calculates the initial kinetic parameters of the impinging species)

The modifications for the program are available at the Adams Research Group; please contact Dr. John E. Adams, 125 Chemistry, University of Missouri-Columbia, Columbia, MO 65211; email: AdamsJE@missouri.edu

Example input files of scattering simulations with the modified DL_Poly_2.14

```

Lattice file generated by FILE_MAKER utility
2 3 10000 0.6700000000E-02
28.3800000000 0.0000000000 0.0000000000
0.0000000000 28.3800000000 0.0000000000
0.0000000000 0.0000000000 100.0000000000

In 1
6.870605483 12.44053657 0.2855249818
-1.154613622 0.8594792310 0.8872173385
1229.817071 199.3177395 -426.5489047

In 2
1.189468469 -1.575574448 7.129228752
-0.3094614861 0.7885624488 1.683013346
-209.9235555 3456.379451 2908.476731

In 3
-9.025655106 -13.96244888 2.414629203
0.5162052900 2.012533845 0.2660316106
1688.449000 -4878.496239 -2834.426827

In 4
-4.312874177 -11.91480649 4.688999633
-0.8916189498 0.6339304688 0.4639006117E-01
-1509.489856 787.1667132 -1526.453356

In 5
12.98042307 3.050710720 8.615255999
-3.116169774 -1.362340991 0.6984951346
250.7028726 381.0348773 -2715.923720

In 6
10.58573756 -11.91217740 16.66592433
-0.8336733171 -0.3061387454 -2.758203259
558.4633127 -301.0051079 -2650.704105

In 7
9.785548499 5.639688265 -3.133538566
0.3622890608 -2.628258033 0.2672247180
694.0797986 1890.793114 870.0481074

In 861
-9.761518904 11.68378030 3.585013603
-1.228820944 1.200114653 -1.240629894
683.3674368 1400.339909 1850.634306

In 862
-10.13948064 -6.318459059 -9.232952489
-2.932925486 -1.623277351 1.780985517
723.0088509 -441.4164045 1031.617515

In 863
-2.217822895 10.04125209 4.499010301
-1.645950143 -0.6431327478 -2.333998222
569.6398683 653.1057610 -852.9581085

In 864
3.845405405 5.382952392 -5.639147316
-2.657757677 -0.2140870220 1.222732537
-1199.869212 -4361.590833 -311.9565849

Ar 865
0.0000000000 0.0000000000 50.00000000
0.0000000000 0.0000000000 0.00000000
0.0000000000 0.0000000000 0.00000000

```

Figure A-1. Excerpt of an example CONFIG file used for scattering simulations

The CONFIG file contains the coordinates, velocities and forces of each atom in the system. It was constructed by using an equilibrated configuration of the liquid lamella, (the length of the cell in the z-direction during equilibration was 80 Å), increasing the cell length in the z-direction to 100 Å, and then adding the impinging species (in this case Ar). The impinging atom(s) information goes at the end of the file; this placement tells the program how to differentiate the bulk from the mobile species

(shown in the red frame). A POSITIONS file is needed to be made, using the HISTORY file of a previous equilibration. For this purpose a slightly modified, version of the unformatted **traject.f** subroutine is used.

```

CONTROL file generated by DL_POLY/java utility

temperature      459.00
pressure         0.0000
ensemble nve

steps            12000
equilibration    0
multiple step    1
print           1000
stack           1000
stats           100000

timestep         0.0012
cutoff           7.0250
delr width       1.0000
rvdw cutoff      7.0250
no electrostatics
shake tolerance  1.0E-5
quaternion tolerance  1.0E-5

detector         49.0000
cycle            4000
scatter          92.0000
scatangle        55.0000

job time         10000000.0
close time       500.000

finish

```

Figure A-2. Example CONTROL file used for scattering simulations

The steps keyword (blue frame) in a scattering calculation defines how many time steps each trajectory will last, and is involved in differentiating the scattered from the trapped species. The following variables also need to be defined:

detector: this is the cutoff value in the positive z-direction for detecting the end of a scattering trajectory,

cycle: the number of trajectories calculated during the simulation,

scatter: the initial kinetic energy for the impinging species (in this case in kJ/mol),

also the keyword to turn on the scattering simulation mode in DL_Poly, and

scatangle: defines the impact angle of the scattering species (relative to the normal to the surface)

```
Simulation of Liquid indium,
UNITS kJ
Scatter 1
MOLECULES 2
Indium
nummols 864
atoms 1
  In      114.82      0.0      1
finish
Argon (incoming particle)
nummols 1
atoms 1
  Ar      39.948      0.0      1
finish
vdw 3
In      In      1j      5.04525      2.81
Ar      Ar      1j      0.99572      3.41
In      Ar      12-6 7338137.029      0.00
close
```

Figure A-3. Example CONTROL file used for scattering simulations

The FIELD file, which describes the interaction potentials between atoms (both intra- and intermolecular) only contains the extra parameter scatter (red frame), telling the program the number of atoms making up the impinging species (essentially telling the program how many atoms it has to count back from the end of the CONFIG file in getting information about the incident species).

Appendix B

Electronic Structure Investigation of Host-Guest Interactions Within Hexameric Pyrogallol[4]arene Nano-Capsules

Hexameric nano-capsules based on pyrogallol[4]arenes (PgCn, figure A-4)⁷⁹⁻⁸² are one of the cornerstone research interests of the Atwood group, as forming non-covalent capsules with large internal volume is a main goal of supramolecular chemistry. The capsule formed by assembling six of the PgCn molecules is held together by 72 hydrogen bonds, giving it high structural stability, and has an internal volume of $\sim 1250 \text{ \AA}^3$.

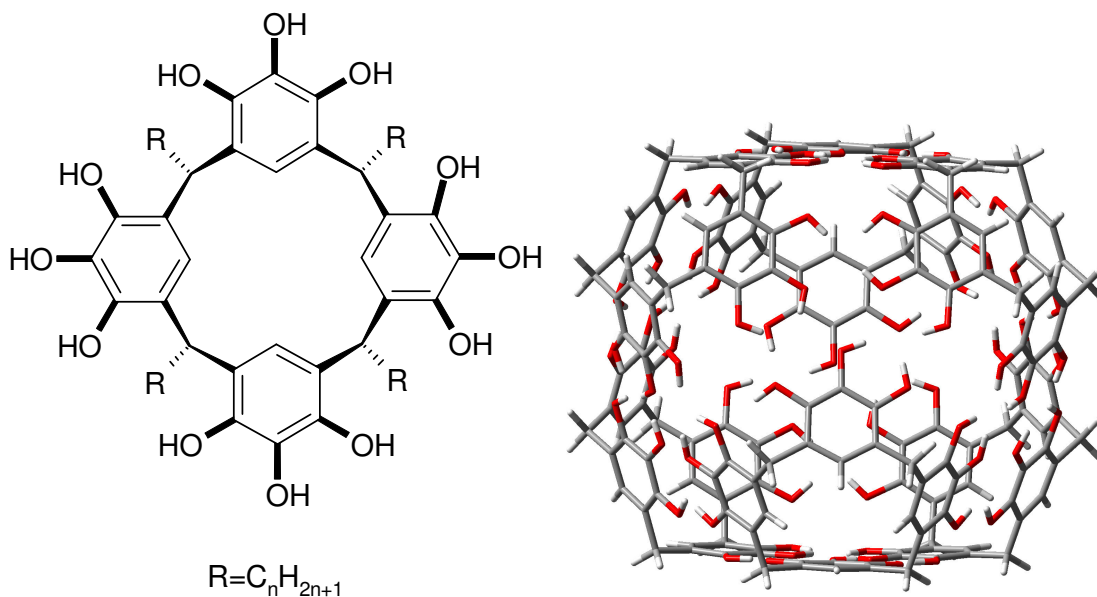


Figure A-4. Chemical structure of pyrogallol[4]arene on the left and the hexameric capsule on the right.

The latest investigations, led by Scott J. Dalgarno, were aimed at examining the inner environment of these structures by encapsulating molecular probes.^{81,82} They have found that when they used pyrene butyric acid as a probe, they have two probe molecules in one capsule aligned with the capsule inner walls, interacting with the walls, and kept apart by ~ 8 Å. On the other hand, when they tried to encapsulate benzo[α]pyrene (B[α]P) and pentacene, they have found only one of these molecules in each capsule. They have found that pentacene clearly can not align itself with the wall, maximizing the π -stacking interactions, because of its length. The orientation for the B[α]P was less clear, due to disorder in the crystal structure, though the space filling diagrams they created indicated an orientation towards the center of the capsule.

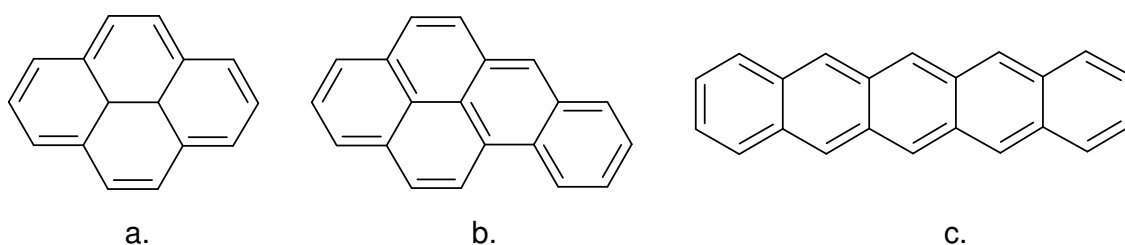


Figure A-5. Chemical structure of a) pyrene, b) benzo[α]pyrene (B[α]P) and c) pentacene

To resolve the B[α]P orientation issue they turned to the theoretical chemistry group of Prof. Carol A. Deakyne, and accordingly we started performing electronic structure calculations to address the problem. We used pyrene in our calculations instead of the pyrene butyric acid, since the important moiety of the molecule participating in the interaction with the capsule wall is the pyrene.

Using the Gaussian 03 software suite,⁸³ we sought to answer two questions: first, is there a difference between the positioning of the pyrene and the benzo[α]pyrene, and if they show different orientations, is the difference caused mainly by steric effects or by

differences in the nonbonding interactions; second, how well do the low-to-medium levels of theory we were required to use (due to the size of the system) for most of the calculations reproduce the equilibrium structures given by higher levels of theory.

To answer the first question, we set up two sets of model structures for both pyrene and benzo[α]pyrene. The guest molecules were paired up with a single pyrogallol molecule ($\text{C}_6\text{H}_6\text{O}_3 \cdots \text{C}_{16}\text{H}_{10}$ and $\text{C}_6\text{H}_6\text{O}_3 \cdots \text{C}_{20}\text{H}_{12}$) in the first set, and with a “wall segment” comprised of three pyrogallol molecules, held together by intra- and intermolecular hydrogen bonds ($(\text{C}_6\text{H}_6\text{O}_3)_3 \cdots \text{C}_{16}\text{H}_{10}$ and $(\text{C}_6\text{H}_6\text{O}_3)_3 \cdots \text{C}_{20}\text{H}_{12}$), in the second. The calculations were performed at the B3LYP/cc-pVDZ level on these complexes. We also have placed each guest molecule in a rigid half nano-capsule and optimized the structures at the B3LYP/3-21G level. The rigid half capsule was generated from the X-ray diffraction structure by holding the heavy atoms in place, aligning the OH hydrogens to maximize the hydrogen bonding, and replacing the R-groups and capping the alkyl groups with hydrogen atoms.

For answering the second question, structures of pyrogallol with benzene ($\text{C}_6\text{H}_6\text{O}_3 \cdots \text{C}_6\text{H}_6$) were studied at the B3LYP/cc-pVDZ, MP2/cc-pVDZ and MP2/aug-cc-pVDZ levels of theory. Complexes of benzene with the “wall segment” were only studied at the B3LYP/cc-pVDZ level. All complexes, except the ones containing the pyrogallol[4]arene half nano-capsule, were fully optimized using the tight convergence criterion of the Gaussian 03 suite of programs.⁸³ To ensure that all structures correspond to minima on their own potential energy surfaces, we calculated the harmonic vibrational frequencies for all optimized complexes.

For the benzene and pyrogallol complexes, two “edge-on” and one “face-to-face” orientations were observed at all calculational levels. The one “edge-on” orientation where an O-H $\cdots\pi$ interaction was observed is less relevant, because in the capsule the guest has little chance of slipping between the structural hydrogen bonds and giving such an orientation. The second “edge-on” complex has C-H \cdots O (and possibly C-H $\cdots\pi$) interactions. The face-to-face arrangement is a slipped parallel structure with an O-H $\cdots\pi$ interaction between the benzene and the pyrogallol. The latter two experimentally significant arrangements are shown in figure A-6.

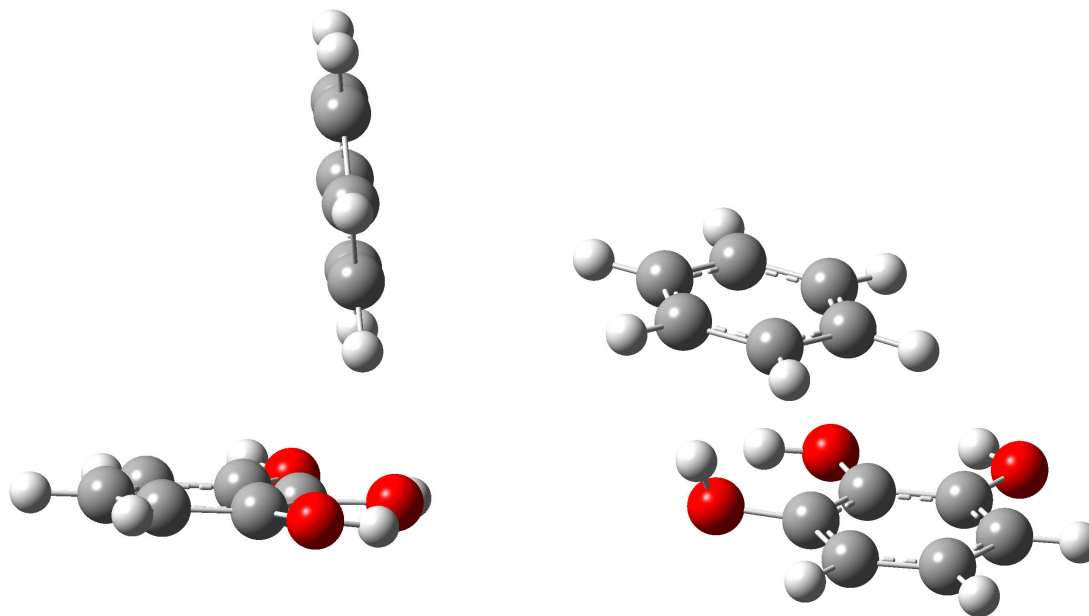


Figure A-6. Optimized structures for benzene/pyrogallol complexes at the MP2/cc-pVDZ level of theory.

For the complexes pyrogallol/pyrene and pyrogallol/benzo[α]pyrene, we have found similar structures, the difference being that in the face-to-face arrangements, the pyrene and the benzo[α]pyrene are slightly tilted to accommodate the O-H $\cdots\pi$ and C-H \cdots O

interactions (see figure A-7). The B3LYP/cc-pVDZ level of theory likely overemphasizes the importance of the C-H \cdots O hydrogen bonding interactions, since the $\pi\cdots\pi$ interactions are not properly represented at this level of theory.

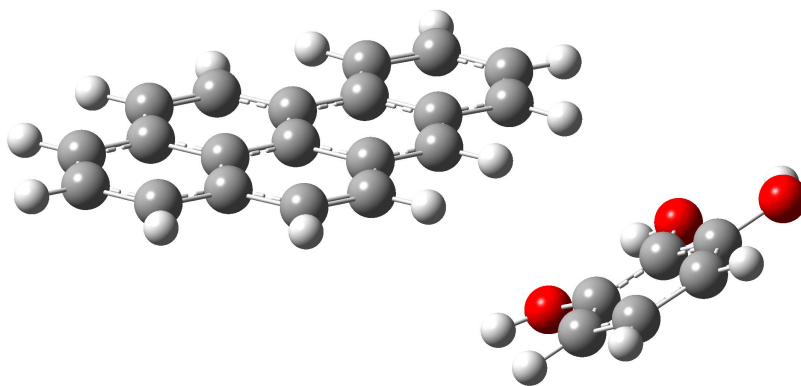


Figure A-7. Optimized structure of the pyrogallol/benzo[α]pyrene complex

The optimized structure for the “wall segment” is a twisted geometry where both the intra- and intermolecular hydrogen bonding is maximized (figure A-8).

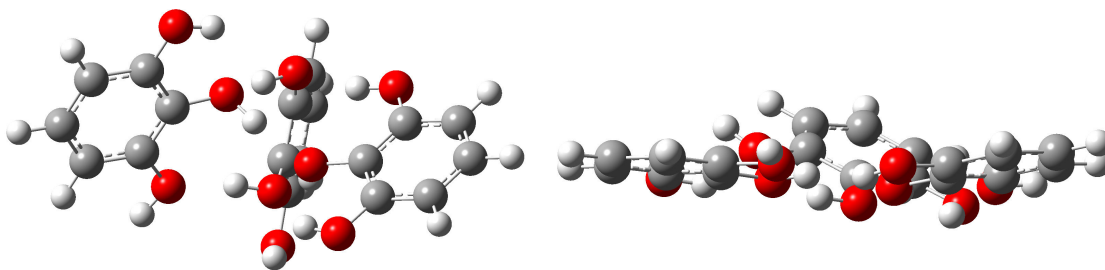


Figure A-8. Optimized structures for the “wall segment” at the B3LYP/cc-pVDZ level on the left, and at the MP2/cc-pVDZ level on the right

In the complexes formed by either of the guest molecules with the wall segment, the segment flattens somewhat but not to the extent found in the nano-capsule (figure A-9). Both guests (pyrene and benzo[α]pyrene) form both face-to-face and edge-on

complexes with the wall segment, while the model compound benzene could be only found in the edge-on orientation.

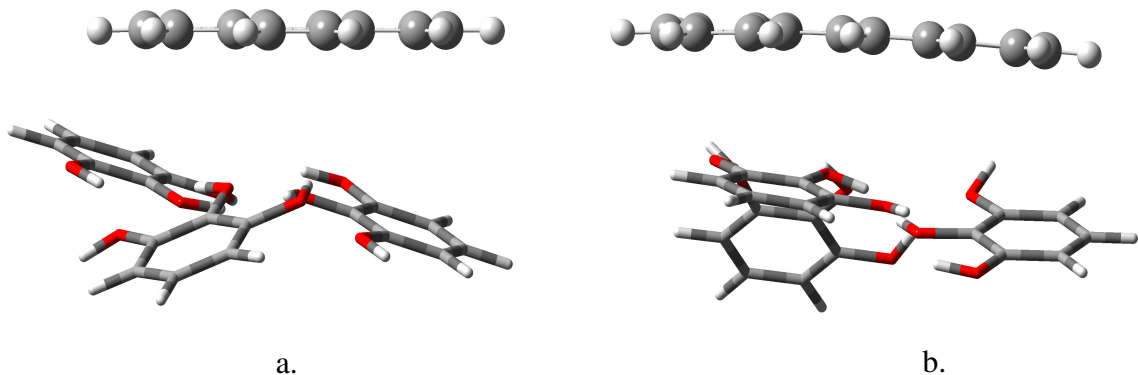


Figure A-9. Optimized structures of the a) pyrene/wall segment and b) benzo[α]pyrene/wall segment complexes.

In the B3LYP/3-21G calculations, where the pyrene was placed along an entire wall (at the bottom of the rigid half nano-capsule) we have found that the guest stays relatively close to the wall and is nearly parallel with the wall as it was observed in solution and the solid structures of the pyrene butyric acid guest (encapsulated in the experiments). At the same time, when we repeated the optimization at the same level and with a similar starting geometry but with the benzo[α]pyrene as guest, the molecule immediately bent out of the molecular plane, a good indication that the starting geometry is greatly different from the equilibrium structure. More precisely in this case, the guest does not fit the space available. The optimized structure, where the benzo[α]pyrene is planar again, has the guest tilted, halfway hanging out of the half nano-capsule (as shown in figure A-10), supporting the finding that the B[α]P is located in the center of the hexameric nano-capsule. Part of the guest is still inside the rigid half sphere, possibly forming C-H \cdots π and C-H \cdots O interactions with the pyrogallol[4]arenes.

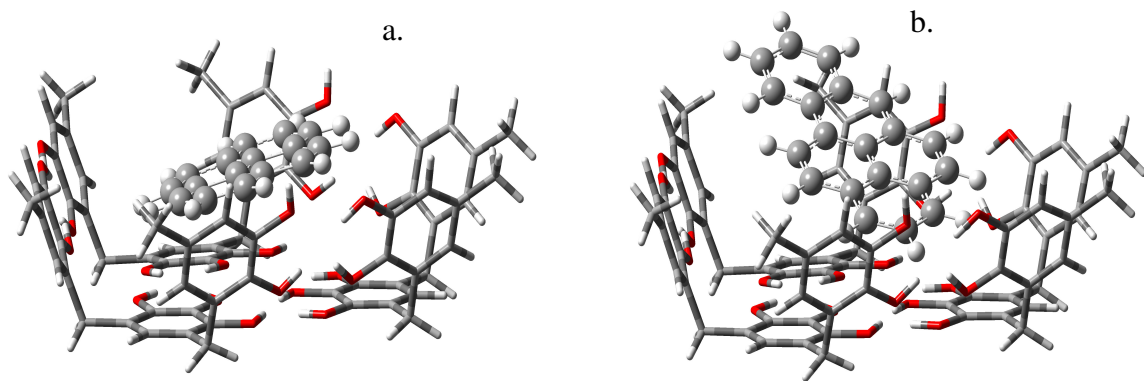


Figure A-10. Optimized structures of the a) pyrene/rigid half nano-capsule and b) benzo[α]pyrene/rigid half nano-capsule complexes

In conclusion, it was found that there was no significant difference, based on the series of model complexes evaluated, between the non-bonding host-guest interactions existing between the hexameric pyrogallol[4]arene nano-capsule and pyrene butyric acid (modeled by pyrene), and those between the capsule and benzo[α]pyrene. The interactions resulted in similar equilibrium geometries for similar systems. The observation that the B[α]P occupies the center of the capsule is a consequence of steric effects related to its larger size.⁸⁴

References Cited:

1. *Air Conditioning Thermodynamics*; California Air Resources Board: Sacramento, CA, 2004.
2. Cengel, Y.; Boles, M., *Thermodynamics: An Engineering Approach, 3rd Edition*. WCB/McGraw-Hill: London, UK, 1997.
3. Johnson, V. H. *Heat-Generated Cooling Opportunities in Vehicles*; SAE 2002-01-1969; Society of Automotive Engineers: 2002.
4. Akhavan, J., *The Chemistry of Explosives, Second Edition*. 2004.
5. Akhavan, J., Explosives and propellants. *Kirk-Othmer Encyclopedia of Chemical Technology (5th Edition)* **2005**, 10, 719-744.
6. Ransom, S.; Cammann, H.-H., *ME 163*. Classic Publications, Ian Allan Publishing: Hersham, UK, 2005.
7. Miller, M. S., Three-phase combustion modeling: frozen ozone, a prototype system. *Materials Research Society Symposium Proceedings* **1996**, 418, (Decomposition, Combustion, and Detonation Chemistry of Energetic Materials), 169-80.
8. Miller, M. S.; Anderson, W. R., Energetic-material combustion modeling with elementary gas-phase reactions: A practical approach. *Progress in Astronautics and Aeronautics* **2000**, 185, (Solid Propellant Chemistry, Combustion, and Motor Interior Ballistics), 501-531.
9. Miller, M. S. In *Burning-Rate Models and Their Successors: A Personal Perspective*, ARL-TL-2996, U.S. Army Research Laboratory; Aberdeen Proving Ground, MD, 2003
10. Saecker, M. E.; Govoni, S. T.; Kowalski, D. V.; King, M. E.; Nathanson, G. M., Molecular beam scattering from liquid surfaces. *Science (Washington, DC, United States)* **1991**, 252, (5011), 1421-4.

11. Rettner, C. T.; Mullins, C. B.; Bethune, D. S.; Auerbach, D. J.; Schweizer, E. K.; Weinberg, W. H., Molecular beam studies of trapping dynamics. *Journal of Vacuum Science & Technology, A: Vacuum, Surfaces, and Films* **1990**, 8, (3, Pt. 2), 2699-704.
12. Waseda, Y.; Saito, M.; Suzuki, S., Structural characterization of surface and morphology of materials using X-ray scattering. *Springer Series in Materials Science* **2004**, 64, (Morphology Control of Materials and Nanoparticles), 223-255.
13. Asadchikov, V. E.; Kozhevnikov, I. V.; Krivonosov, Y. S., X-ray investigations of surface roughnesses. *Crystallography Reports (Translation of Kristallografiya)* **2003**, 48, (5), 836-850.
14. Fiehrer, K. M.; Nathanson, G. M., Energy and angle-resolved uptake of organic molecules in concentrated sulfuric acid. *Journal of the American Chemical Society* **1997**, 119, (1), 251-252.
15. Morris, J. R.; Behr, P.; Antman, M. D.; Ringeisen, B. R.; Splan, J.; Nathanson, G. M., Molecular beam scattering from supercooled sulfuric acid: collisions of HCl, HBr, and HNO₃ with 70 wt. % D₂SO₄. *Journal of Physical Chemistry A* **2000**, 104, (29), 6738-6751.
16. Behr, P.; Morris, J. R.; Antman, M. D.; Ringeisen, B. R.; Splan, J. R.; Nathanson, G. M., Reaction and desorption of HCl and HBr following collisions with supercooled sulfuric acid. *Geophysical Research Letters* **2001**, 28, (10), 1961-1964.
17. Chorny, I.; Benjamin, I.; Nathanson, G. M., Scattering, trapping, and ionization of HCl at the surface of liquid glycerol. *Journal of Physical Chemistry B* **2004**, 108, (3), 995-1002.
18. Klassen, J. K.; Fiehrer, K. M.; Nathanson, G. M., Collisions of organic molecules with concentrated sulfuric acid: scattering, trapping, and desorption. *Journal of Physical Chemistry B* **1997**, 101, (44), 9098-9106.
19. Tribe, L.; Manning, M.; Morgan, J. A.; Stephens, M. D.; Ronk, W. R.; Treptow, E.; Nathanson, G. M.; Skinner, J. L., Argon scattering off the surface of liquid indium: exit angle and energy dependence. *Journal of Physical Chemistry B* **1998**, 102, (1), 206-211.

20. Ronk, W. R.; Kowalski, D. V.; Manning, M.; Nathanson, G. M., Inert gas scattering from molten metals: probing the stiffness and roughness of the surfaces of atomic liquids. *Journal of Chemical Physics* **1996**, 104, (12), 4842-9.
21. Ringeisen, B. R.; Muentert, A. H.; Nathanson, G. M., Collisions of HCl, DCl, and HBr with Liquid Glycerol: Gas Uptake, D \rightarrow H Exchange, and Solution Thermodynamics. *Journal of Physical Chemistry B* **2002**, 106, (19), 4988-4998.
22. Nathanson, G. M., Bouncing gases off liquids: molecular beam studies of transient and not-so-transient solvation. *Proceedings of the Robert A. Welch Foundation Conferences on Chemical Research* **1994**, 38th, 187-95.
23. Benjamin, I.; Wilson, M. A.; Pohorille, A.; Nathanson, G. M., Scattering of water from the glycerol liquid-vacuum interface. *Chemical Physics Letters* **1995**, 243, (3,4), 222-8.
24. Nathanson, G. M., Molecular beam studies of gas-liquid interfaces. *Annual Review of Physical Chemistry* **2004**, 55, 231-255.
25. King, M. E.; Fiehrer, K. M.; Nathanson, G. M.; Minton, T. K., Effects of thermal roughening on the angular distributions of trapping and scattering in gas-liquid Collisions. *Journal of Physical Chemistry A* **1997**, 101, (36), 6556-6561.
26. King, M. E.; Saecker, M. E.; Nathanson, G. M., The thermal roughening of liquid surfaces and its effect on gas-liquid collisions. *Journal of Chemical Physics* **1994**, 101, (3), 2539-47.
27. Chase, D.; Manning, M.; Morgan, J. A.; Nathanson, G. M.; Gerber, R. B., Argon scattering from liquid indium: Simulations with embedded atom potentials and experiment. *Journal of Chemical Physics* **2000**, 113, (20), 9279-9287.
28. Barker, J. A.; Auerbach, D. J., Gas-surface dynamics, velocity distributions, trapping, and residence times. *Faraday Discussions of the Chemical Society* **1985**, (80), 277-89.
29. Rettner, C. T.; Auerbach, D. J.; Tully, J. C.; Kleyn, A. W., Chemical Dynamics at the Gas-Surface Interface. *Journal of Physical Chemistry* **1996**, 100, (31), 13021-13033.

30. Feldman, L. C.; Mayer, J. W., *Fundamentals of Surface and Thin Film Analysis*. North-Holland: New York, 1986.
31. Hurlbut, F. C.; Beck, D. E. *D.E.U.C. Eng. Proj. Report He-150-166*; University of California: 1959.
32. Sinha, M. P.; Fenn, J. B., Scattering of an argon beam by a liquid glycerin surface. *C. R. - Symp. Int. Jets Mol., 5th* **1975**, Paper No B6, 8 pp.
33. Olander, D. R.; Balooch, M.; Siekhaus, W. J., Reactions of chlorine with liquid metals. 4. Tin. *Journal of Physical Chemistry* **1986**, 90, (18), 4397-402.
34. Balooch, M.; Siekhaus, W. J.; Olander, D. R., Reactions of chlorine with liquid metals. 1. Indium. *Journal of Physical Chemistry* **1984**, 88, (16), 3521-8.
35. Balooch, M.; Siekhaus, W. J.; Olander, D. R., Reactions of chlorine with liquid metals. 2. Lead. *Journal of Physical Chemistry* **1984**, 88, (16), 3529-31.
36. Balooch, M.; Siekhaus, W. J.; Olander, D. R., Reactions of chlorine with liquid metals. 3. Bismuth. *Journal of Physical Chemistry* **1986**, 90, (8), 1671-6.
37. Balooch, M.; Olander, D. R.; Siekhaus, W. J., Reaction of water vapor and oxygen with liquid uranium. *Oxidation of Metals* **1987**, 28, (3-4), 195-211.
38. Olander, D. R.; Balooch, M.; Siekhaus, W. J., Reaction and thermal accommodation of gases with liquid uranium and two uranium alloys. *High Temperature Science* **1987**, 24, (1), 21-35.
39. King, M. E.; Nathanson, G. M.; Hanning-Lee, M. A.; Minton, T. K., Probing the microscopic corrugation of liquid surfaces with gas-liquid collisions. *Physical Review Letters* **1993**, 70, (7), 1026-9.
40. Lipkin, N.; Gerber, R. B.; Moiseyev, N.; Nathanson, G. M., Atom scattering studies of liquid structure and dynamics: collisions of Xe with a model of squalane. *Journal of Chemical Physics* **1994**, 100, (11), 8408-17.

41. Nathanson, G. M.; Davidovits, P.; Worsnop, D. R.; Kolb, C. E., Dynamics and Kinetics at the Gas-Liquid Interface. *Journal of Physical Chemistry* **1996**, 100, (31), 13007-13020.
42. Morgan, J. A.; Nathanson, G. M., Atom scattering from atomic surfactants. Collisions of argon with a dilute Bi:Ga solution. *Journal of Chemical Physics* **2001**, 114, (5), 1958-1961.
43. Manning, M.; Morgan, J. A.; Castro, D. J.; Nathanson, G. M., Examination of liquid metal surfaces through angular and energy measurements of inert gas collisions with liquid Ga, In, and Bi. *Journal of Chemical Physics* **2003**, 119, (23), 12593-12604.
44. Muis, A.; Manson, J. R., Rare gas scattering from molten metals examined with classical scattering theory. *Journal of Chemical Physics* **1997**, 107, (5), 1655-1663.
45. Muis, A.; Manson, J. R., Angular distributions of Ar reflected from molten metal surfaces. *Journal of Chemical Physics* **1999**, 111, (2), 730-736.
46. Smith, W.; Forester, T. R., *DL_POLY_2*, version 2.14; CCLRC: Daresbury, Warrington, U.K, 2003.
47. Smith, W.; Forester, T. R.; Todorov, I. T.; Leslie, M., *The DL_POLY_2 User Manual*. CCLRC Daresbury Laboratory: Daresbury, Warrington, UK, 2006.
48. Siavosh-Haghighi, A. Topics in molecular dynamics
 - I. Local structure in a supercritical fluid: solute rotational dynamics
 - II. Energy transfer at a gas-liquid interface in a Lennard-Jones system. University of Missouri-Columbia, Columbia MO, 2004.
49. WebBook, N. C. NIST Standard Reference Database 69.
<http://webbook.nist.gov/chemistry/> (August, 6. 2007),
50. Harris, J., Mechanical energy transfer in particle-surface collisions. In *Dynamics of Gas-Surface Interactions*, ed. Rettner, C. T.; Ashfold, M. N., Royal Society of Chemistry: Cambridge, U.K., 1991; p 1-46.

51. Logan, R. M.; Stickney, R. E., Simple classical model for the scattering of gas atoms from a solid surface. *Journal of Chemical Physics* **1966**, 44, (1), 195-201.
52. Logan, R. M.; Keck, J. C.; Stickney, R. E., Simple classical model for the scattering of gas atoms from a solid surface: additional analyses and comparisons. *Rarefied Gas Dynamics* **1967**, 1, 49-66.
53. Tully, J. C., Washboard model of gas-surface scattering. *Journal of Chemical Physics* **1990**, 92, (1), 680-6.
54. Baule, B., Theoretical treatment of phenomena in rarefied gases. *Annalen der Physik (Berlin, Germany)* **1914**, 44, 145-76.
55. Weinberg, W. H.; Merrill, R. P., Simple classical model for trapping in gas-surface interactions. *Journal of Vacuum Science and Technology* **1971**, 8, (6), 718-24.
56. Zangwill, A., *Physics at Surfaces*. Cambridge University Press: Cambridge, UK, 1988.
57. Szabo, T. J.; Siavosh-Haghighi, A.; Adams, J. E., Energy Transfer at a Gas-Liquid Interface: Kinematics in a Prototypical System. *Journal of Physical Chemistry B* **2006**, 110, (3), 1319-1325.
58. Sorescu, D. C.; Rice, B. M.; Thompson, D. L., Theoretical studies of solid nitromethane. *Journal of Physical Chemistry B* **2000**, 104, (35), 8406-8419.
59. Sorescu, D. C.; Rice, B. M.; Thompson, D. L., Molecular Dynamics Simulations of Liquid Nitromethane. *Journal of Physical Chemistry A* **2001**, 105, (41), 9336-9346.
60. Agrawal, P. M.; Rice, B. M.; Thompson, D. L., Molecular dynamics study of the melting of nitromethane. *Journal of Chemical Physics* **2003**, 119, (18), 9617-9627.
61. Agrawal, P. M.; Rice, B. M.; Thompson, D. L., Molecular dynamics study of the effects of voids and pressure in defect-nucleated melting simulations. *Journal of Chemical Physics* **2003**, 118, (21), 9680-9688.
62. Siavosh-Haghighi, A.; Thompson, D. L., Molecular dynamics simulations of surface-initiated melting of nitromethane. *Journal of Chemical Physics* **2006**, 125, (18),

63. Siavosh-Haghighi, A.; Thompson, D. L., Melting Point Determination from Solid-Liquid Coexistence Initiated by Surface Melting. *Journal of Physical Chemistry C* **2007**, 111, (22), 7980-7985.
64. Trevino, S. F.; Prince, E.; Hubbard, C. R., Refinement of the structure of solid nitromethane. *Journal of Chemical Physics* **1980**, 73, (6), 2996-3000.
65. Trevino, S. F.; Rymes, W. H., A study of methyl reorientation in solid nitromethane by neutron scattering. *Journal of Chemical Physics* **1980**, 73, (6), 3001-6.
66. Cromer, D. T.; Ryan, R. R.; Schiferl, D., The structure of nitromethane at pressures of 0.3 to 6.0 GPa. *Journal of Physical Chemistry* **1985**, 89, (11), 2315-18.
67. Grosev, V. M.; Stelzer, F.; Jocham, D., Internal rotation dynamics of nitromethane at low temperatures. *Journal of Molecular Structure* **1999**, 476, (1-3), 181-189.
68. Jones, W. M.; Giaque, W. F., The entropy of nitromethane. Heat capacity of solid and liquid. Vapor pressure, heats of fusion and vaporization. *Journal of the American Chemical Society* **1947**, 69, 983-7.
69. Yarger, F. L.; Olinger, B., Compression of solid nitromethane to 15 GPa at 298 K. *Journal of Chemical Physics* **1986**, 85, (3), 1534-8.
70. Piermarini, G. J.; Block, S.; Miller, P. J., Effects of pressure on the thermal decomposition kinetics and chemical reactivity of nitromethane. *Journal of Physical Chemistry* **1989**, 93, (1), 457-62.
71. Cavagnat, D.; Magerl, A.; Vettier, C.; Anderson, I. S.; Trevino, S. F., Anomalous pressure dependence of the torsional levels in solid nitromethane. *Physical Review Letters* **1985**, 54, (3), 193-6.
72. Wucherer, E. J.; Christofferson, S. S.; Reed, B. In *AIAA Paper 2000-3872*, 36th AIAA/ASME/SAE/ASEE Joint Propulsion Conference, Huntsville, AL, 2000
73. Hannum, J. A. E., In *Liquid Propellants.*, ed. Chemical Propulsion Information Agency: Laurel, MD, 1984.

74. Meyer, R.; Köhler, J.; Homburg, A., *Explosives*. Wiley-VCH: Weinheim, Cambridge, 2002.
75. Kelzenberg, S.; Eisenreich, N.; Eckl, W.; Weiser, V., Modelling nitromethane combustion. *Propellants, Explosives, Pyrotechnics* **1999**, 24, (3), 189-194.
76. Boyer, E.; Kuo, K. K., Modeling of nitromethane flame structure and burning behavior. *Proceedings of the Combustion Institute* **2007**, 31, (Pt. 2), 2045-2053.
77. Hobbs, M. L.; Baer, M. R.; McGee, B. C., JCZS: an intermolecular potential database for performing accurate detonation and expansion calculations. *Propellants, Explosives, Pyrotechnics* **1999**, 24, (5), 269-279.
78. Perkins, B. G., Jr.; Nesbitt, D. J., Quantum-State-Resolved CO₂ Scattering Dynamics at the Gas-Liquid Interface: Incident Collision Energy and Liquid Dependence. *Journal of Physical Chemistry B* **2006**, 110, (34), 17126-17137.
79. Atwood, J. L.; Barbour, L. J.; Jerga, A., Organization of the interior of molecular capsules by hydrogen bonding. *Proceedings of the National Academy of Sciences of the United States of America* **2002**, 99, (8), 4837-4841.
80. Cave, G. W. V.; Antesberger, J.; Barbour, L. J.; McKinlay, R. M.; Atwood J. L., *Angewandte Chemie International Edition* **2004**, (43), 5263-5266.
81. Dalgarno, S. J.; Tucker, S. A.; Bassil, D. B.; Atwood, J. L., Fluorescent Guest Molecules Report Ordered Inner Phase of Host Capsules in Solution. *Science (Washington, DC, United States)* **2005**, 309, (5743), 2037-2039.
82. Dalgarno, S. J.; Bassil, D. B.; Tucker, S. A.; Atwood, J. L., Cococrystallization and encapsulation of a fluorophore with hexameric pyrogallol[4]arene nanocapsules: structural and fluorescence studies. *Angew Chem Int Ed* **2006**, 45, (42), 7019-22.
83. Frisch, M. J.; Trucks, G. W.; Schlegel, H. B.; Scuseria, G. E.; Robb, M. A.; Cheeseman, J. R.; Montgomery, J., J. A.; Vreven, T.; Kudin, K. N.; Burant, J. C.; Millam, J. M.; Iyengar, S. S.; Tomasi, J.; Barone, V.; Mennucci, B.; Cossi, M.; Scalmani, G.; Rega, N.; Petersson, G. A.; Nakatsuji, H.; Hada, M.; Ehara, M.; Toyota, K.; Fukuda, R.; Hasegawa, J.; Ishida, M.; Nakajima, T.; Honda, Y.; Kitao, O.; Nakai, H.; Klene, M.; Li, X.; Knox, J. E.; Hratchian, H. P.; Cross, J. B.; Bakken, V.; Adamo, C.; Jaramillo, J.; Gomperts, R.; Stratmann, R. E.; Yazyev, O.; Austin, A. J.; Cammi, R.; Pomelli, C.; Ochterski, J. W.; Ayala, P. Y.; Morokuma, K.; Voth, G. A.; Salvador, P.; Dannenberg, J.

J.; Zakrzewski, V. G.; Dapprich, S.; Daniels, A. D.; Strain, M. C.; Farkas, O.; Malick, D. K.; Rabuck, A. D.; Raghavachari, K.; Foresman, J. B.; Ortiz, J. V.; Cui, Q.; Baboul, A. G.; Clifford, S.; Cioslowski, J.; Stefanov, B. B.; Liu, G.; Liashenko, A.; Piskorz, P.; Komaromi, I.; Martin, R. L.; Fox, D. J.; Keith, T.; Al-Laham, M. A.; Peng, C. Y.; Nanayakkara, A.; Challacombe, M.; Gill, P. M. W.; Johnson, B.; Chen, W.; Wong, M. W.; Gonzalez, C.; Pople, J. A., *Gaussian 03*, Revision C.02; Gaussian, Inc.: Wallingford, CT, 2004.

84. Dalgarno, S. J.; Szabo, T.; Siavosh-Haghighi, A.; Deakyne, C.; Adams, J. E.; Atwood, J. L., Exploring the limits of encapsulation within hexameric pyrogallol[4]arene nano-capsules. *Journal of the American Chemical Society* **2007**, (submitted).

VITA

Tamas Szabo was born on May 25, 1976 in Miskolc, Hungary. He graduated from his high school the Janos Irinyi Chemical Technical College (Technicum) in Kazincbarcika at 1994. He received his M.Sc. in Chemistry from the Lajos Kossuth University of Sciences (now University of Debrecen) in 1999. Between 1999 and 2002 he was working at the University of Miskolc as an assistant lecturer and researcher in the Institute of Materials Science and Engineering. In 2002 He was accepted as a Chemistry Ph.D. candidate by the Chemistry Department of the University of Missouri-Columbia and achieved his degree in August 2007.